Fakultät für Physik
der Technischen Universität München

Dissertation

Single-Molecule Junction Spectroscopy and Computational Modeling for Molecular Electronics

Yuxiang Gong

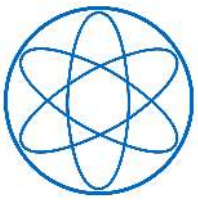

June 2019

Fakultät für Physik
Lehrstuhl für Experimentalphysik

Single-Molecule Junction Spectroscopy and Computational Modeling for Molecular Electronics

Yuxiang Gong

Vollständiger Abdruck der von der Fakultät für Physik
der Technischen Universität München
zur Erlangung des akademischen Grades
eines Doktors der Naturwissenschaften (Dr. rer. nat.)
genehmigten Dissertation.

Vorsitzender:	apl. Prof. Dr. Norbert Kaiser
Prüfende der Dissertation:	1. Prof. Dr. Johannes Barth
	2. Prof. Dr. Pavel Jelínek

Die Dissertation wurde am 14.02.2019 bei der Technischen Universität München eingereicht und durch die Fakultät für Physik am 29.05.2019 angenommen.

Abstract

The investigation of electronic properties of organic molecules is a fundamental aspect in the field of molecular electronics with significant promises for future applications. Conventional approaches are frequently limited to electrical measurements of single-molecule junctions. In this work, a pioneering set-up combined technique which integrates optical spectroscopy with current-voltage characterization on a single-molecule level was employed. Experimental results are complemented and explained by comprehensive DFT simulations, whereby good agreement is obtained. Earlier projects highly relied on manual operations for data acquisition and analysis, which were trapped in low efficiency and limited data volume. Significant improvements have been made by developing a hardware control routine to realize automatic experiments and a multi-functional software to process data, which generates statistical results from current-voltage characteristics as well as sequential Raman spectra. This thesis focuses on the changes of molecular vibrational frequencies depending on applied bias and mechanical stress. One project demonstrates the conformation change of a two-state molecular switch with vibrational spectroscopy at different bias voltages. The other studies the relationship between vibrational frequencies and tension applied to the molecular junction, which indicates a systematic frequency shift of a distinct vibrational mode corresponding to the applied strain.

Contents

Chapter 1

Introduction

Throughout the 20th century, with the development of the nanotechnology, our views of the world have focused into microcosmic structures. The investigation of the nano-scale world can be traced back to 1857, when Faraday reported the Tyndall effect of metallic nanoparticles [1]. Using chemical approaches, Langmuir theorized the possibility of forming single-molecular thin films on the surface of water in 1917 [2] which was further developed by Blodgett to realize the formation of monomolecular films in 1934 (i.e. Langmuir-Blodgett film) [3, 4]. Later in 1946, molecular self-assembly techniques were first introduced by Zisman [5]. Meanwhile, the near-field scanning optical microscope (SNOM) was theoretically proposed by Synge in 1928 [6] and the first electron microscope was developed by Ruska and Knoll in 1931 [7]. These advances prepared the ground for molecular engineering and sustained its advancement.

In recent decades, techniques like the discovery of surface enhanced Raman spectroscopy (SERS) (1974) [8], the proposition of the first unimolecular rectifier (1974) [9], the inventions of scanning tunneling microscope (STM) (1981) [10] and atomic force microscopy (AFM) (1986) [11] have given rise to a boom in nanotechnolgy. Benefiting from advanced nanotechnology, the miniaturization of electronic circuits together with the enormous variations of electrical, optical and mechanical properties of molecules might afford new applications and research methods in the fields of nano-electronics, material science, organic chemistry, biology, quantum chemistry, etc.. Molecular electronics offers the possibility to study the electronic properties at the smallest achievable scale, where the nature is completely dominated by quantum mechanical effects. A common way to build nano-scale devices is to employ individual molecules as the functional component, i.e.

to construct a metal-molecule-metal single-molecule junction. Researches have demonstrated the possibilities to realize single-molecule switches [12–16], transistors [17–21], amplifiers [22, 23], rectifiers [24–27] and logics [28–32].

Prospective engineering methods for molecular studies are often centered on the electronic characterization of single molecules [33–43]. Other approaches focus on chemical [44–47] or mechanical [48–50] properties. Investigations involving light-driven switches often employ photochromic molecules, such as azobenzenes [48, 51–56] or diarylethenes [57–61] to mention a few. Exposure of single-molecule junctions to light also allows for complementary characterization and read-out of molecular states, exceeding present technology in terms of speed [62, 63] and power efficiency (by exploiting minimal electron-induced structural reorganization [64]). While light stands as a versatile read-out method, its implementation in metal-molecule-metal junctions remains challenging. Early attempts employed large-area illumination of break junctions [65–67] and scanning probe tips [37].

Certain molecules have been studied by mechanical manipulation which is commonly achieved by magnetic tweezers [68–70], optical tweezers [71–74] and AFM [75–77]. Most of them focus on stretching induced electrochemical properties such as orbital realignment in benzenedithiol molecular junctions [39], conductance switching of bipyridine-gold junctions [15] and conductance increase in a spin-crossover molecule [78]. Other applications address mechanochemical reactions like force-induced activation of covalent bonds [79] and bond rearrangement in a single molecule [80]. However, studies on tension induced variation of vibrational modes, for instance stretching dependence of vibrational modes in Pt-H_2-Pt junctions [81], are scarce.

From the theoretical point of view, the electronic structure of individual atoms and molecules play an essential role in the electronic transport properties [82, 83]. Therefore, a detailed description of the electronic structure of the individual molecules is necessary, which can be achieved by using the simulation methods in quantum chemistry such as density functional theory (DFT).

In this thesis, the electrical and optical properties of single-molecule junctions are investigated simultaneously using a self-built molecular junction spectroscopy. DFT simulations are performed to complement the experiments. Previous projects including the detection of the photocurrent of a single photosynthetic protein [84] and molecular junctions exhibiting negative differential conductance [85] have been performed with the same set-up. The investigation of electron-phonon interactions in single-molecule junctions [86], which was already addressed in my master thesis [87], is included with the latest progresses containing the negative bias Stokes Raman results, the theoretical rate model of charge-vibrational coupling based on the anti-Stokes Raman spectrum and the internal vibrational-vibrational relaxation time measured by infrared time-resolved spectroscopy. The corresponding article entitled ***Vibrational Excitations in Current-Driven Single Molecule Junctions*** has been submitted. Results of two independent

studies which focus on voltage-driven conformational switching and tension induced vibrational shifts are mainly elaborated here. The former is contained in the publication of ***Voltage-Driven Conformational Switching with Distinct Raman Signature in a Single-Molecule Junction (2018)*** [88], the latter entitled ***Tension Induced Vibrational Frequency Shifts in Helicene Molecules*** is under preparation for submission.

The thesis is arranged as following:

Chapter 1 lists the milestones and breakthroughs in nanotechnology and outlines the synopsis of this thesis.

Chapter 2 introduces the theories and techniques related to the experiments, i.e. single-molecule junction, charge transport and Raman spectroscopy, as well as the foundations of density functional theory (DFT).

Chapter 3 elaborates the details of the self-built set-up, the procedures and conditions of the experiments and simulations, and the algorithms for data processing.

Chapter 4 discusses the results of the investigations of single-molecule charge-vibrational coupling, a single-molecule switch and a nano-vibromechanical system in terms of experimental and computational aspects.

Chapter 5 gives a brief summarization of the work.

The automated LabVIEW control procedures as well as the data analysis software are introduced in the **Appendixes**.

Chapter 2

Experimental and Theoretical Background

Employing single-molecules as active functional units in electronic devices is a promising technological concept of strong current interest [60, 89–97]. Many recent advances in nanofabrication techniques have realized single-molecule devices [98–100]. The conductivity behavior of organic molecules which are immobilized by self-assembly techniques between two metallic electrodes have been investigated and single molecules have already proven to act as functional parts in nano-scale devices [101–104]. For the development of such components, it is crucial to understand electron transport mechanisms through nano-scale devices and multiparameter studies are required to improve this understanding of electron transport through single-molecule junctions.

In this chapter, the fundamental theories regarding the experimental and computational methods in our research are introduced. Firstly, the techniques to investigate single-molecule junctions as well as the principle of electron transport through molecular junctions are elaborated. Secondly, the concept of Raman spectroscopy and signal enhancement mechanisms are described. Finally, the essential theorems in density functional theory (DFT) are elucidated.

2.1 Single-Molecule Junctions

As demonstrated in Fig. 2.1, a single-molecule electronic device can be established by contacting a molecule to metal electrodes in a circuit. Due to the manifold electronic

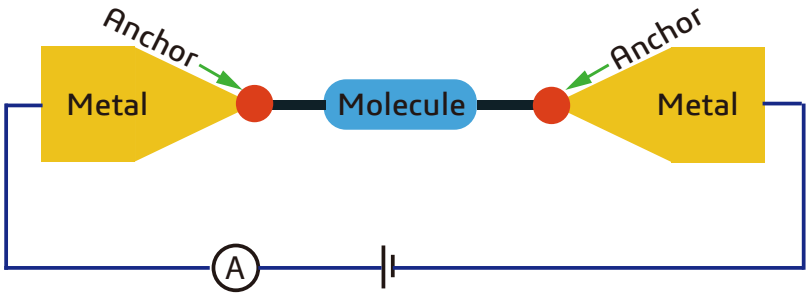

FIGURE 2.1: Concept of a single-molecule junction. A molecule is bonded to two metal electrodes with anchor groups in a circuit.

properties of the carbon-based molecules, they can be used as promising functional molecular unit. According to the functionalities [105], the carbon-based molecules can act as: conducting wires, insulators, switches, storage elements, diodes and amplifiers. In order to form a mechanically stable contact and electronically transparent chemical bond between the molecule and the metal electrodes, anchor groups are indispensable. The facile reactions between thiols and gold make them the ideal choice as anchor groups and electrodes for single-molecule devices. The sulfur-gold bond is mechanically stable with a force up to 1.5 nN [106].

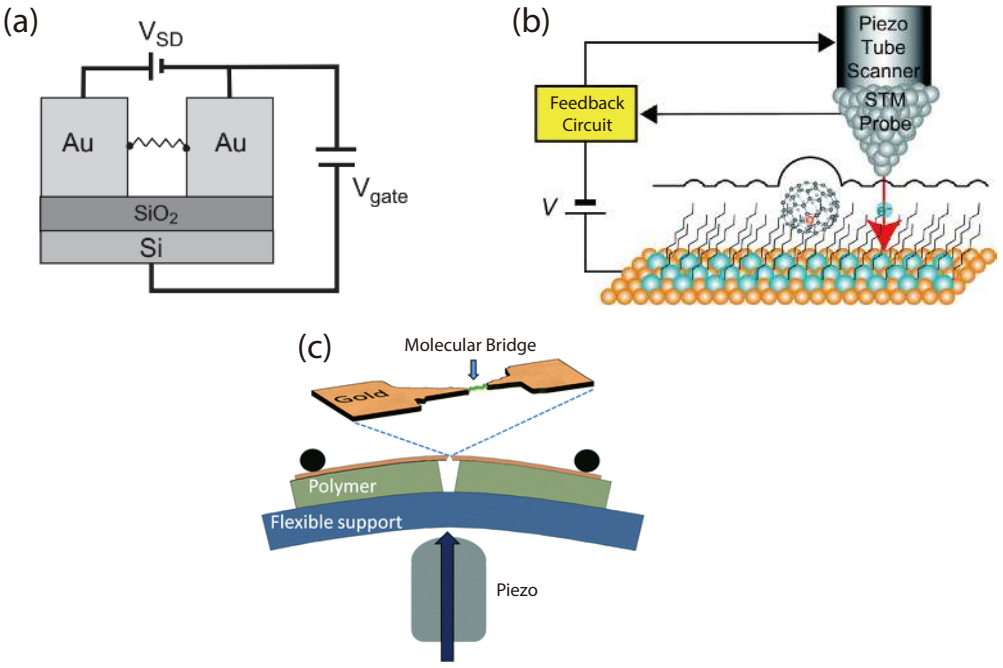

FIGURE 2.2: Techniques commonly employed to form single-molecule juncions. (a) "On-chip" techniques, adopted from [105], (b) scanning probe junctions adopted from [107] and (c) mechanically controlled break-junctions (MCBJ) adopted from [108].

The methods to form single-molecule junctions can be divided into three main classes. As the first one has to mention the so calles "on-chip" techniques which can produces

stable junctions which are suitable for systematic studies of their transport behavior. However, the geometry of the electrodes is fixed and contamination cannot be eliminated. As one example, electodes fabricated by the electromigration technique [109–111] is illustrated in Fig. 2.2a. It allows to build three-terminal devices where a gain electrode can be realized to apply an external electric potential. The other two approaches enables clean contacts and adjustable junction geometry. The scanning probe microscopy (SPM) [76, 112–116] (Fig. 2.2b) is the most straightforward method to contact a single molecule by approaching the molecule on the substrate with the tip until a chemical connection is established. However, the junction formation is sometimes with limited stability. As to the mechanically controlled break-junctions (MCBJ) [65, 90, 101, 117, 118] (Fig. 2.2c), similar to electromigrated junctions, the molecules are deposited after the electrode gap is mechanically broken. The junction is then gradually closed until a measurable current flows. At room temperature, the electrode atoms are rather mobile, thus the molecular junctions have limited lifetime. MCBJ has the main disadvantage that it does not allow for multiparameter studies. In this thesis, a technique which is a crossover between SPM and MCBJ is applied, meaning that a molecular junction is formed by driving a substrate towards a fixed metallic probe in one-dimension.

2.2 Charge Transport Through Molecular Junctions

A single-molecule junction is a one-dimensional nano-device with two metal-molecule interfaces. Electron transport in an one-dimensional conductor can be described as a scattering problem according to the *Landauer-Büttiker Formalism* [119–122]. Fig. 2.3a shows a schematic of a ballistic conductor. For a given particle, a mean free path is the average length that the electron can travel freely, which can be increased by reducing the number of impurities in a crystal or by decreasing its temperature. Ballistic transport is observed when the mean free path of the electron is significant longer than the dimension of the medium through which the electron travels. For example, ballistic transport can be observed in a metal nano-wire whose length is at the nanometer scale and the mean free path can be longer than that in a metal [123]. If the diameter of the wire is in the range of the wavelength of the electrons, additional quantization effects are expected.

Fig. 2.3b shows a one-dimensional conductor with a quadratic dispersion, where $k_N = \frac{2\pi}{L}N$. The current carried by this transport model can be expressed as

$$I = \frac{e}{L}\sum_k v(k)[f_1(k) - f_2(k)], \tag{2.1}$$

where $\frac{e}{L}$ is the electron density, v is the velocity of the conducting electrons and $f(k)$ is the Fermi distribution. Considering an infinite length L of the conduction channel, the

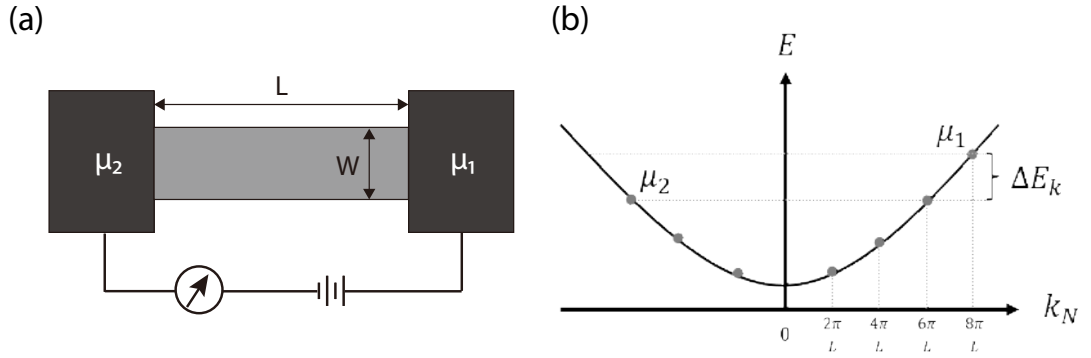

FIGURE 2.3: Ballistic conductor and single eigenchannel model. (a) A ballistic conductor connected to two electrodes. A voltage is applied which forms a chemical potential difference of $\mu_1 - \mu_2$ between the electrodes. L and W denote the length and width of the conducting channel; (b) A one-dimensional conductor with a quadratic dispersion which is described by discrete k-states at corresponding energies, ΔE_k is the difference of the electrochemical potential.

group velocity v can be expressed as $v(k) = \frac{1}{\hbar} dE/dk$, it turns into

$$I = \frac{2e}{h} \int_{\mu_2}^{\mu_1} [f_1(k) - f_2(k)] dE. \tag{2.2}$$

At temperatures of absolute zero ($0\ K$), the integral of the difference of Fermi distributions is equal to the electrochemical potential difference $\Delta E_k = \mu_1 - \mu_2$, therefore the current can be expressed as

$$I = \frac{2e}{\hbar} (\mu_1 - \mu_2). \tag{2.3}$$

The electrochemical potential difference $\mu_1 - \mu_2$ is equal to one unit of electronvolt (eV), thus

$$I = \frac{2e^2}{h} V. \tag{2.4}$$

This leads to an expression, where the conductance is not depending on the length of the conductor and given by:

$$G_0 = \frac{2e^2}{h} \approx \frac{1}{12.9}\ k\Omega^{-1}. \tag{2.5}$$

More generalized one has to sum up all contributing conductance channels,

$$G_{tot} = G_0 \sum_{i=1}^{n} T_i, \tag{2.6}$$

which is the expression of *Laudauer formula* [119]. This formula indicates that the number of modes contributing to the conductance can be altered by changing the size

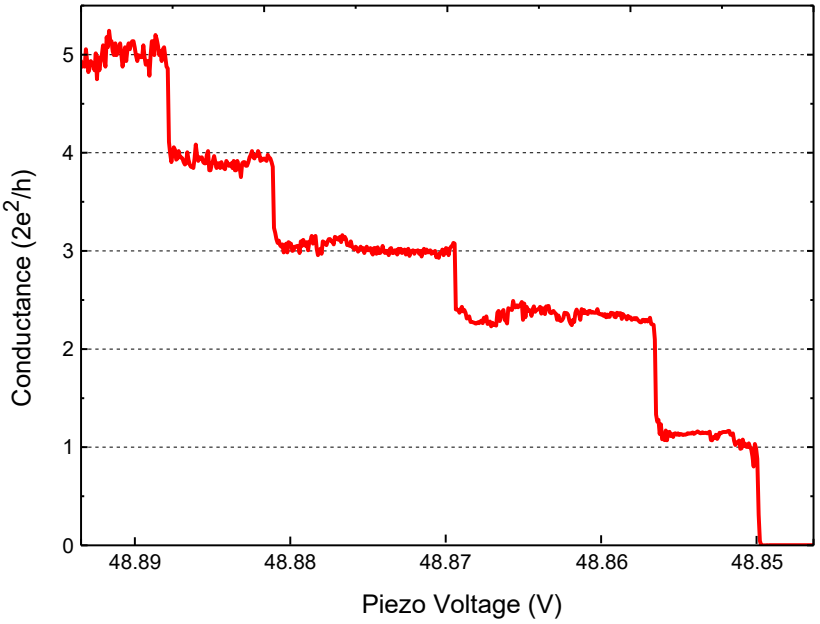

FIGURE 2.4: Conductance quantization in units of $2e^2/h$, observed by stepwise modifications during the stretching of a metallic contact (gold-gold). The figure is adopted from [86].

of the contact and thus the conductance of the ballistic conductor could be a step-like manner, as shown in Fig. 2.4. The steps are approximately integer multiples of $2e^2/h$ (G_0), which is referred to as conductance quantization.

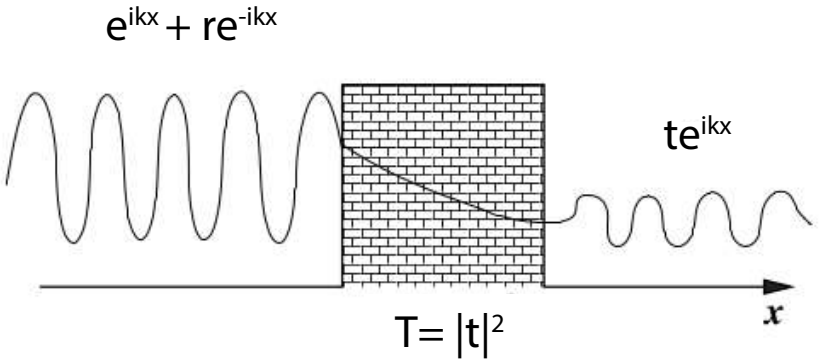

FIGURE 2.5: Wave function crossing a potenital barrier. The wave is partially transmitted with a probability $T = |t|^2$ while partially being reflected with a probability r. Figure is adopted from [105].

Let's consider a plane wave $(1/\sqrt{L})e^{ikx}$ (Fig. 2.5) which crosses the barrier in Fig. 2.3 from right to left. This wave is partially transmitted with a probability $T = |t|^2$ while

partially being reflected with a probability r. Eq. (2.1) can be expressed in quantum-mechanical form

$$I = \frac{e}{L} \sum_k v(k) T(k). \tag{2.7}$$

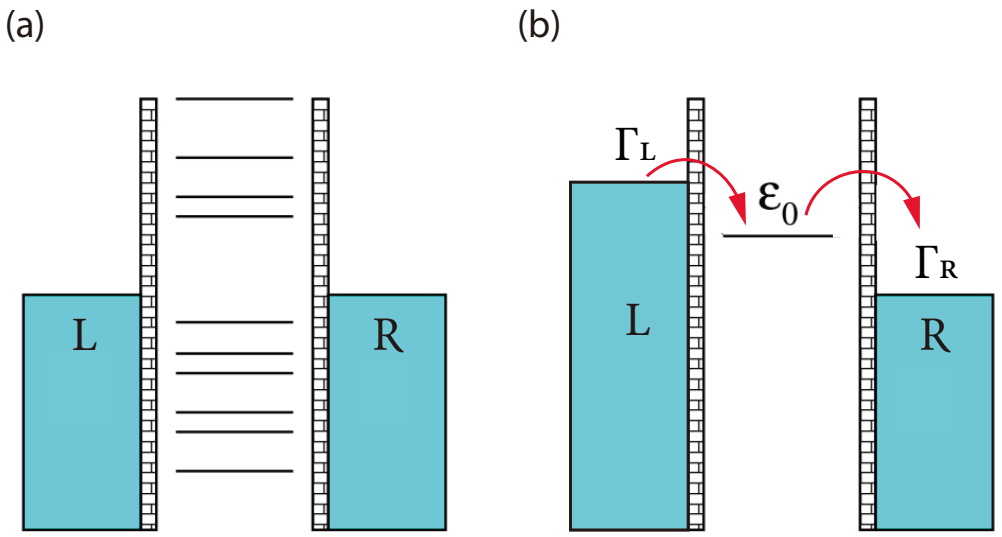

FIGURE 2.6: (a) Orbital scheme of a molecular junction. (b) The charge transport proceeds through a single orbital ε_o. Figures are reproduced from [105].

To investigate electron transport through a metal-molecule-metal contact, it is common to start considering the molecular orbitals within a junction. The orbital level scheme of a molecular junction is depicted in Fig. 2.6a, where the Fermi energy of the electrodes lies in between the highest occupied molecular orbital (HOMO) and the lowest unoccupied molecular orbital (LUMO) of the molecule. The chemical potential of the electrodes can be shifted by applying a bias voltage V (Fig. 2.6b). Therefore, a factor $f_1(k)[1 - f_2(k)]$ is taken into account to ensure that the initially occupied states on the left and empty on the right contribute to the current flow. Accordingly, the current can be written as

$$I_{L \to R} = \frac{e}{L} \sum_k v(k) T(k) f_1(k)[1 - f_2(k)]. \tag{2.8}$$

By introducing the density of state $dk/dE = m/(\hbar^2 k)$, where the energy $E = \hbar^2 k^2/(2m)^2$, and convert the sum into integral, the current can be expressed as

$$I_{L \to R} = \frac{e}{h} \int T(E) f_1(E)[1 - f_2(E)] dE. \tag{2.9}$$

Correspondingly, the current from right to left can be written as

$$I_{R \to L} = \frac{e}{h} \int T(E) f_2(E)[1 - f_1(E)] dE, \tag{2.10}$$

where we assume that the transmission probability is identical regardless of the direction. Therefore, the total current $I = I_{L\to R} - I_{R\to L}$ can be expressed as

$$I = \frac{2e}{h}\int_{-\infty}^{\infty}[f_1(E) - f_2(E)]T(E)dE, \tag{2.11}$$

which is simplest version of the *Landauer formula* and it builds up the relationship between current and transmission.

In principle, several molecular orbitals can participate in the electron transport simultaneously. However, the general situation is that the Fermi level of the metal lies close to either the HOMO or the LUMO of the molecule. Thus, one of them dominates the charge transport in a certain voltage range as Fig. 2.6b depicted. Due to the hybirdization of the metallic states and the molecular orbitals, the molecular states have a finite brodening that depends on the strength of the metal-molecule coupling, which can be described by the scattering rates Γ_L and Γ_R. According to the Landauer Formula Eq. (2.11), the current-voltage (I-V) characteristics in this model can be express as

$$I(V) = \frac{2e}{h}\int_{-\infty}^{\infty}[f(E - eV/2) - f(E + eV/2)]T(E, V)dE, \tag{2.12}$$

where due to the spin symmetry of the model, the factor 2 is included, $f(E)$ is the Fermi function and $T(E, V)$ is the transmission function depending on energy and voltage. The transmission function is given by the *Breit-Wigner formula* [124]

$$T(E, V) = \frac{4\Gamma_L\Gamma_R}{[E - \epsilon_0(V)]^2 + [\Gamma_L + \Gamma_R]^2}. \tag{2.13}$$

Fig. 2.7c shows a typical I-V characteristics with the corresponding first derivative, namely the conductance, in which three different regions can be distinguished. In the low bias region, the voltage is smaller than $|\varepsilon_o|$ (Fig. 2.7a), there is no charge transfer through the barrier since there is no molecular orbital within the energy window between $[-V_0,\ V_0]$ of the I-V curves in Fig. 2.7c. When the resonance condition $eV/2 = \varepsilon_0(V)$, i.e. $eV = 2\varepsilon_0$ (Fig. 2.7b), the level of the first molecular orbital is aligned to the chemical potential of one electrode. At $|V_0|$ the current suddenly increases and a peak appears in the conductance curve as illustrated in Fig. 2.7c.

On the other hand, the interaction between a tunneling electron and its environment can lead to the loss of coherence. According to *Landauer* & *Buttiker* [125], the traversal time τ that an electron staying in a junction can be calculated by

$$\tau = L\sqrt{m/2\Delta E}, \tag{2.14}$$

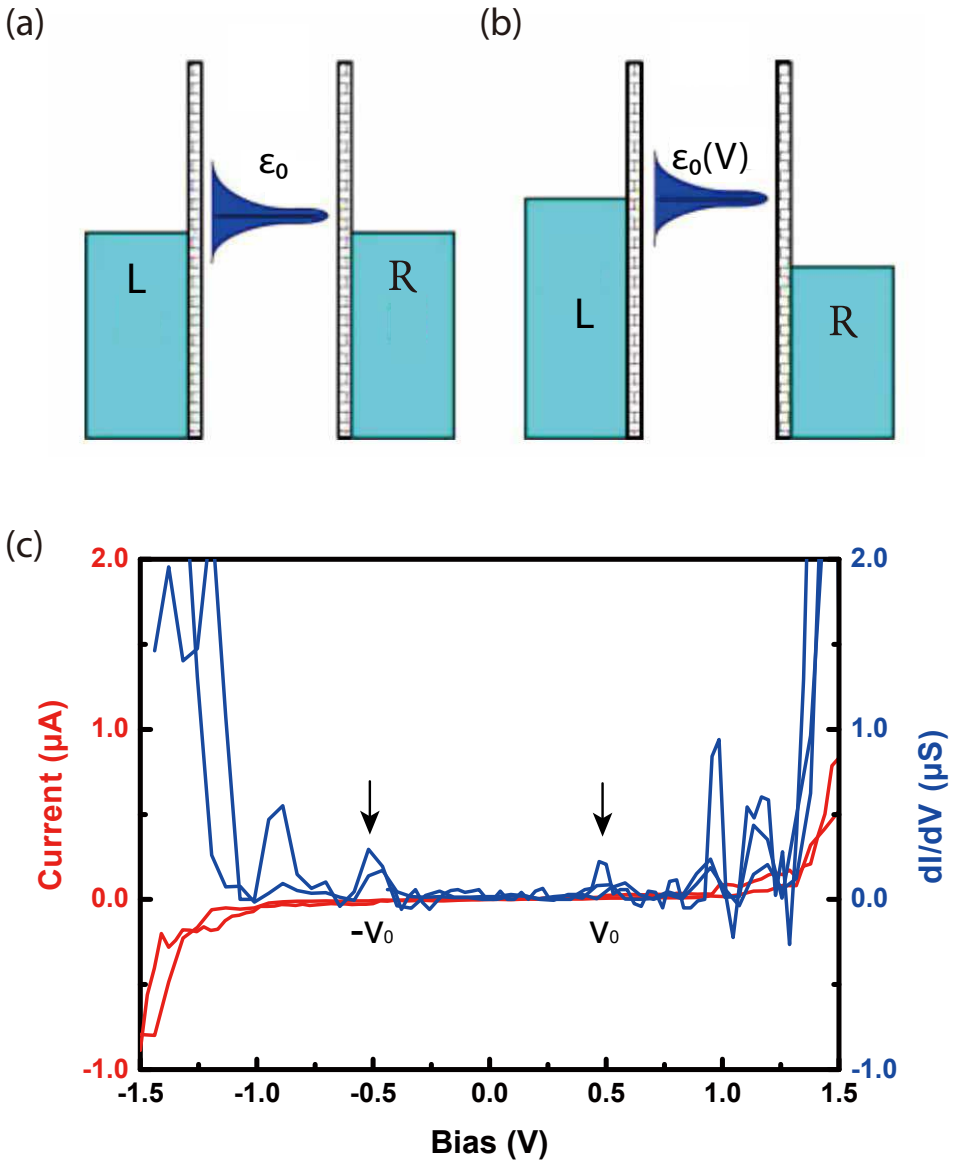

FIGURE 2.7: Electron transport in a single molecule junction. (a) Zero bias region and (b) resonant state region, figures are adopted from [105]; (c) Current-voltage characteristic of a single-molecule junction, adopted from [88].

where ΔE is the energy difference of the barrier, L is the width and m is the electron mass. The traversal time is normally expressed as

$$\tau = \hbar/\sqrt{\Delta E^2 + \Gamma^2}. \tag{2.15}$$

The dominant interactions between the electrons and the environment are relaxation (energy transfer) and dephasing (energy fluctuation). If the timescales, an electron is localized on the molecules, as well as interactions with its environment become important, one speaks of hopping transport rather than the coherent tunneling [126]. When

a molecule is weakly coupled to the electrodes and the energy spacing between states is small, the transport is dominated additionally by the Coulomb interaction. This is called *Coulomb blockade* regime, which can be often observed in metallic quantum dots [127].

When the tunneling time is considerable larger than the inelastic scattering time and the elextron has to traverse the junction by a sequence of spatially separated states, one speaks of sequential hopping. In long molecules, for instance the DNAs [128–130], additional conditions of the environment also play an essential role in the transport procedure (thermally assisted sequential hopping).

In recent decades, charge transport through alkanethiols has been widely studied both theoretically and experimentally in the scope of single molecules [76, 88, 131–136] and self-assembled monolayers (SAM) [103, 137], due to the chemical stability and the large HOMO-LUMO gap. Moreover, gold as electrodes are commonly used to connect the molecule through the relatively strong chemical Au-S bond.

2.3 Raman Spectroscopy

Raman spectroscopy is a popular technique to study the vibrations in molecular systems and provides information on the chemical structure of the material. This technique uses a laser light source to irradiate a sample, and generates a small amount of Raman scattered light, which is detected as a Raman spectrum. The phenomenon of *Raman scattering* was first observed experimentally by C. V. Raman and K. S. Krishnan in 1928 [138], and hence won the Nobel Price for physics in 1930.

2.3.1 Raman Scattering

When light is scattered by matter, majority of the scattering is an elastic process and there is no change in energy. However, a very small percentage of scattering is an inelastic process, thus a scattered light has different energy from incident light. As illustrated in Fig. 2.8, let us consider an incident phonon is absorbed by a molecule and excites the molecule to a virtual energy level, which has a short lifetime and decays with an emitted photon. If the energy of the incident photon is identical to the emitted one, i.e. the photon is elastically scattered, such phenomenon is referred to as *Rayleigh scattering* [140–143]. If the virtual state of the molecule has a higher energy than the initial state, the emitted light is shifted to a lower frequency to balance the total energy of the system. This redshift in the frequency is called Stokes shift. However, the vibrational modes of a molecular system might be already occupied without the interaction with incident light. This occurs especially at nonzero temperatures or due to electron phonon interactions. The incident light can then absorb energy from the system and emitted a photon with

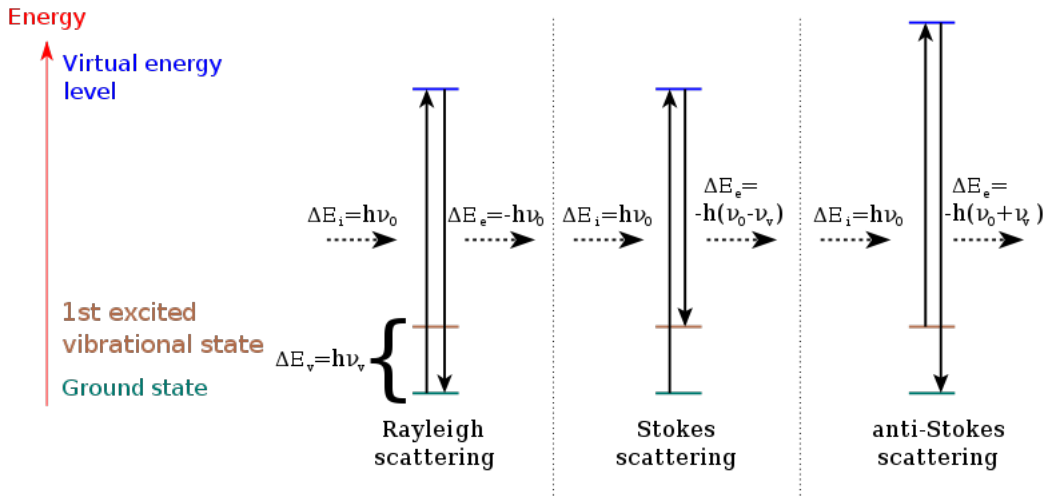

FIGURE 2.8: Energy level diagram of Rayleigh scattering, Stokes and anti-Stokes Raman scattering. Figure is adopted from [139].

more energy, which result in blueshift called anti-Stokes shift. At room temperature, the molecules in the ground state tend to interact with photons mainly by Stokes scattering [144]. The ratio γ of the intensities of anti-Stokes and Stokes scattering is dependent on the amount of molecules on in the ground and the first excited vibrational states:

$$\gamma = \frac{N_m}{N_n} = \frac{d_m}{d_n} exp\left[\frac{-(E_m - E_n)}{kT}\right], \tag{2.16}$$

where N_m and N_n are the numbers of molecules in the excited vibrational state and the ground vibrational state respectively, d is the degeneracy of the levels m and n, $E_m - E_n$ is the energy difference between the two vibrational states, k is the Boltzmann constant and T is the absolute temperature[1].

The spectrum of the scattered photons is termed Raman spectrum which presents the correlation between Raman shift and intensity of the signal. Raman shift is generally expressed in terms of wavenumbers with an unit of inverse length (normally cm^{-1}):

$$\Delta\omega = (\frac{1}{\lambda_0} - \frac{1}{\lambda}), \tag{2.17}$$

where $\Delta\omega$ is the Raman shift, λ_0 the wavelength of the incident light source and λ the wavelength of the Raman spectrum. The intensity I of Raman scattering of a vibrational mode can be calculated by

$$I = K\alpha^2 P\omega^4, \tag{2.18}$$

where K presents a collection of constants such as the speed of light, α is the polarizability of the electrons from which the information of the molecule can be derived, P

[1] In the quantum-mechanical description, matter at absolute zero is in its ground state, i.e. the state of lowest energy.

and ω are the power and the frequency of incident light [145–147]. Thus, two of four parameters are related to the device, namely using the highest possible power of light source would maximize the Raman intensity. However, there is a high risk of molecule degradation with high power illumination. To avoid this problem, less straightforward techniques with the moderate power of the light source with improved Raman sensitivity have been developed, for instance, surface- and tip-enhanced Raman spectroscopy.

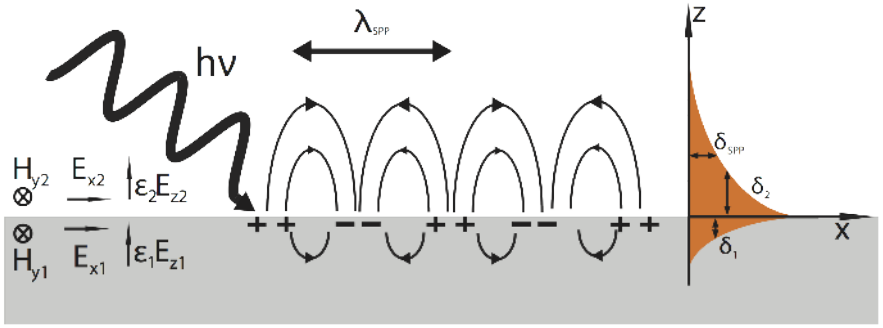

FIGURE 2.9: Sketch of a surface plasmon. An electromagnetic wave propagating along a metal-dielectric interface and the dependence of the electromagnetic field intensity on the distance to the interface. Figure is adopted from [148].

2.3.2 Signal Enhancement

Prior to the introduction of signal enhancement techniques, it is essential to start with the basic principle of surface plasmons (SPs). As illustrated in Fig. 2.9, the oscillatory motion of electrons at the interface between two materials with different dielectric constants is assigned to surface plasmons. The charge motion in a SPs generates electromagnetic fields along the interface. The charge density oscillation together with the associated electromagnetic fields are called surface plasmon polaritions (SPP). The intensity of the electromagnetic field is exponentially dependent on the distance along the interface on the both sides of the interface. In the case of a metal-vacuum/-dielectric interface, the electric field decays perpendicular to the metal surface.

For Raman spectroscopy, one often employs field enhancement techniques that amplify the intensity of incident light to excite the vibrational modes in the molecule to increase the Raman scattered signal. Moreover, the emitted Raman scattered light is further enhanced with the same mechanism, resulting in an extensive increase of the total output. As shown in Fig. 2.10a, the molecules are effectively adsorbed on a rough metal surface. The roughness of the surface leads to field line crowding at sharp protrusions on the surface when interacting with light. This phenomenon is termed as surface-enhanced Raman spectroscopy (SERS) [152, 153]. SERS was initially observed by M. Fleischman *et al.* in 1974 [8] and is able to give an enhancement of the signal of up to 10^{11} [154], which has been applied to detect the signal of single molecules with an extremely small cross-section ($\sim 10^{-29}\ cm^2$) [155] since the last two decades [156, 157].

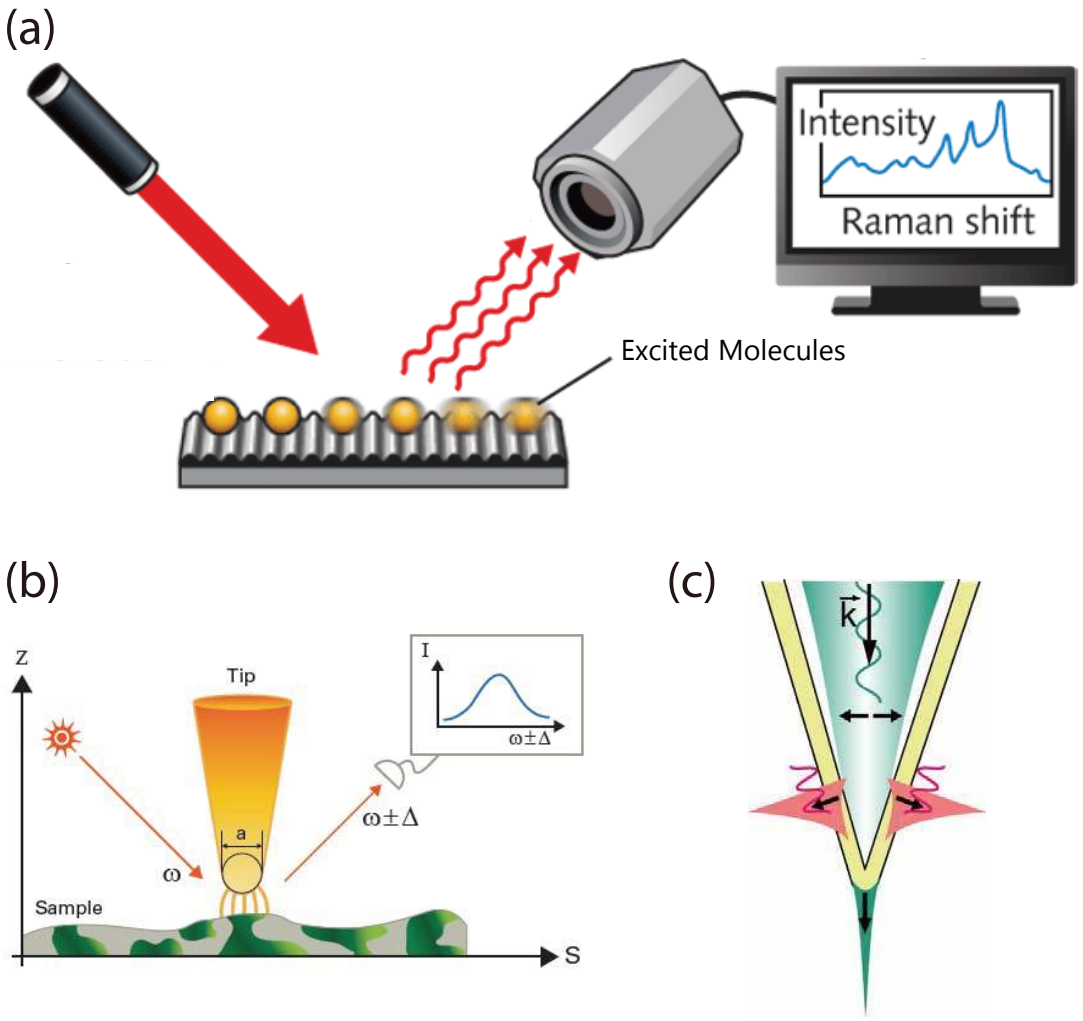

FIGURE 2.10: Signal enhancement techniques. (a) Schematic of SERS, adopted from [149]. (b) Schematic of TERS configuration, adopted from [150]. (c) Schematic of apertureless SNOM, adopted from [151]

The maximum resolution can be achieved by an optical microscopy is limited by the Abbe limit, which is approximately half of the wavelength of the incident light. If a metallic probe is illuminated by a confocal microscope (Fig. 2.10b), SPP are excited by the incident light and will propagate towards the sharp apex of the probe. As a result, field enhancement with a factor of $10^6 - 10^7$ can be achieved at the tip apex with a spatial resolution down to $20 - 30\ nm$ [158]. This variant of SERS overcomes most of the drawbacks of SERS, such as the limitations of the substrate (i.e. rough metal surface), the low sensitivity and lack of spatial resolution, but keeps its advantages is referred to as tip-enhanced Raman spectroscopy (TERS) [159–163].

It has been shown that a tapered optical fiber covered with thin metal film can be used as high efficient optical probe in near-field microscopy [151, 164–167]. As shown in Fig. 2.10c, light reaches the fiber and excited SPP propagates towards the tip apex resulting in a highly confined, extremely intense field. This approach is termed as aperture-less

scanning near-field optical microscopy (SNOM). In this thesis, we applied a gold coated glass tip with atomically sharp apex for the detection of Raman signals of a single molecule.

2.4 Density Functional Theory

DFT has been applied to a wide range of structures, from molecular systems to complex solid structures to calculate their ground state energy and electron density related properties, such as the structure of the molecule, the vibrational frequencies etc. The essential ideas of DFT was reported in two publications: one was by Hohenberg and Kohn in 1964 [168], and the other was by Kohn and Sham in 1965 [169]. Accompanied with the development of powerful computing system, it has become the most popular quantum chemical simulation method nowadays. Thus, it was not a surprise when Walter Kohn received the Nobel Prize in chemistry in 1999 for the development of the density functional theory.

The *Hohenburg-Kohn theorem* affirms that the electron density determines all ground-state properties of a system, meaning that the total ground state energy of a many-body system is a functional of its electron density. In DFT, the functional relates the electron density to the energy in space and time. By solving the functional self-consistently, an approximate solution to *Schrödinger equation* of the N-body system can be found, which gives the ground state energy of the system.

According to the studies of a broad range of molecules [170, 171], DFT tends to overestimate the bond length by $1-2\%$ and provides an accuracy of $5-10\%$ for the simulation of vibrational frequencies. There is no systematic approach to improve the calculated results towards the exact solutions [172].

2.4.1 The Hohenberg-Kohn Theorems

We want to begin with one-particle quantum mechanics [173]. The Hamiltonian of an electron is given by

$$\widehat{h} = -\frac{1}{2}\nabla^2 + \nu(\vec{r}), \tag{2.19}$$

where $\nu(\vec{r})$ is an external potential. The energy eigenstates $\psi_\alpha(\vec{r},\sigma)$ and eigenvalues ε_α are solutions to the time-independent Schrödinger equation

$$\widehat{h}\psi_\alpha(\vec{r},\sigma) = \varepsilon_\alpha\psi_\alpha(\vec{r},\sigma). \tag{2.20}$$

When extended to N electrons, the time-independent Schrödinger equation can be expressed as

$$\left(-\frac{1}{2}\sum_{i=1}^{N}\nabla_i^2 - \sum_{i,j}^{N+N_{nucl}}\frac{Z_j}{|r_i - r_j|} + \sum_{i<j}\frac{1}{|r_i - r_j|}\right)\Psi(r_i) = E\Psi(r_i), \tag{2.21a}$$

$$(\widehat{T} + \widehat{V}_{ee})\Psi(r_i) = E\Psi(r_i), \tag{2.21b}$$

where N_{nucl} is the number of nuclei in the system; r_i and r_j are the positions of the i-th electron and the j-th nuclei; and $\Psi = \Psi(r_1\sigma_1, ..., r_N\sigma_N)$ is the N electron wavefunction; $\widehat{T}$, $\widehat{V}_{ee}$ are the kinetic energy and the electron-electron interaction energy operators, respectively. The electron spin density is defined as $n_\sigma(r_i)$, thus

$$\sum_\sigma \int d^3r n_\sigma(\vec{r}) = N. \tag{2.22}$$

Hohenberg and Kohn proposed that it is possible to reduce the number of degrees of freedom of the time-independent Schrödinger equation [168, 169]. The ground state charge density determines the potential of the system, thus an universal potential $F[\rho]$ can be described as

$$F[\rho] = \langle\Psi^{min}|\widehat{T} + \widehat{V}_{ee}|\Psi^{min}\rangle. \tag{2.23}$$

An external potential $\nu(\vec{r})$ is introduced to describe the external field from the positively charged nuclei. Considering the electron spin density (Eq. (2.22)), the ground state energy can be minimized to

$$E[\rho] = \int d^3r\rho(\vec{r})\nu(\vec{r}) + F[\rho]. \tag{2.24}$$

Eq. (2.23) and Eq. (2.24) are termed to Hohenberg-Kohn first and second theorems.

2.4.2 The Kohn-Sham Method

The ground state energy is then calculated by solving Thomas-Fermi-Hohenberg-Kohn equation in stead of the Schrödinger equation:

$$\frac{\delta E}{\delta\rho} = \frac{\delta F[\rho]}{\delta\rho} + \frac{\delta V_{ext}[\rho]}{\delta\rho} = \lambda, \tag{2.25}$$

where λ is the Lagrange multiplier. This method of getting the ground state energy only in terms of electron density without introducing the concept of electron orbitals is called orbital free kinetic-energy density functional theory (OFDFT) [174].

However, it turns out that the OFDFT method is quite complicated. Kohn and Sham then proposed a simpler way to obtain the ground state energy. For a system without

interacting electrons, the electron-electron interaction energy $\widehat{V}_{ee}$ in Eq. (2.23) vanishes and the universal potential $F[\rho]$ is reduced to

$$F[\rho] = \langle \Phi^{min} | \widehat{T} | \Phi^{min} \rangle, \tag{2.26}$$

where Φ represents the Slater determinant that expresses the Kohn-Sham orbitals[2]. The universal potential of the non-interacting system is redefined in terms of the Kohn-Sham orbitals as

$$F[\rho] = T_s[\rho] + U[\rho] + E_{xc}[\rho], \tag{2.27}$$

where $T_s[\rho]$ is the Kohn-Sham kinetic energy, $U[\rho]$ is the Hartree electrostatic self-repulsion of the electron density [175], $E_{xc}[\rho]$ is the exchange-correlation energy, which is defined as the sum of a distinct exchange and correlation term ($E_{xc}[\rho] = E_x[\rho] + E_c[\rho]$), namely contains the non-Coulomb part of the electron–electron interactions. The ground state energy is accordingly written as

$$E(\rho) = T_s[\rho] + \int d^3r \rho(\vec{r}) \nu(\vec{r}) + U[\rho] + E_{xc}[\rho]. \tag{2.28}$$

Thus, the Kohn-Sham equations can be express as a Schrödinger-like equation

$$\left(-\frac{\hbar^2}{2m} \nabla^2 + V_{eff}(\vec{r}) \right) \phi_i(\vec{r}) = \epsilon_i \phi_i(\vec{r}), \tag{2.29}$$

which is the typical representation of the *Kohn-Sham equation*. V_{eff} is the effective potential, which is the sum of the external potential, the Hartree potential and the exchange-correlation potential.

2.4.3 The Exchange-Correlation Functionals

In practice, the biggest challenge of Kohn-Sham method is to approximate the exchange-correlation energy functional. To this end, the local density approximation (LDA) [176] and the generalized gradient approximations (GGA) [177–181] are the most popular approaches and have been widely used in solid-state physics and quantum chemistry.

LDA is based on the model of an uniform electron gas and is the basis of all the exchange-correlation approximations. Accordingly, the exchange-correlation energy can be expressed as

$$E_{xc}^{LDA}[\rho] = \int d^3r \rho(\vec{r}) \epsilon_{xc}(\rho(\vec{r})), \tag{2.30}$$

where ϵ_{xc} is the exchange-correlation energy per particle which is weighted with the probability $\rho(\vec{r})$ of the existence of an electron at this position. A generalized case

[2] *e.g.*, the 2-electron Slater determinant is $\Phi(1,2) = \psi_{1s}(r_1)\psi_{1s}(r_2)\frac{1}{\sqrt{2}}(\delta_{\sigma_1,\uparrow}\delta_{\sigma_2,\downarrow} - \delta_{\sigma_2,\uparrow}\delta_{\sigma_1,\downarrow})$.

without spin symmetry is given by

$$E_{xc}^{LSDA}[\rho_\uparrow, \rho_\downarrow] = \int d^3r \rho(\vec{r}) \epsilon_{xc}(\rho_\uparrow(\vec{r}), \rho_\downarrow(\vec{r})), \tag{2.31}$$

which is called the local spin-density approximation (LSDA), where $\rho_\uparrow$ and $\rho_\downarrow$ are the two spin densities. However, the accuracy of the LSDA approach is insufficient for molecular simulations including hydrogen bonding [182, 183], band gaps in semiconductors and insulators [184, 185].

If a gradient of the density $\bigtriangledown\rho(\vec{r})$ is introduced to the LSDA (Eq. (2.31)), the approach is advanced to the so called generalized gradient approximation (GGA) which can be written as

$$E_{xc}^{GGA}[\rho_\uparrow, \rho_\downarrow] = \int d^3r f(\rho_\uparrow, \rho_\downarrow, \bigtriangledown\rho_\uparrow, \bigtriangledown\rho_\downarrow). \tag{2.32}$$

In practice, the energy is split into two parts $E_{xc}^{GGA} = E_x^{GGA} + E_c^{GGA}$ which are approximated separately. The exchange part has the form

$$E_x^{GGA} = A_x \int d^3r \rho^{4/3} F_x(s), \tag{2.33}$$

where the function F_x is the reduced density gradient for spin $s = \frac{|\bigtriangledown \rho(\vec{r})|}{\rho^{4/3}}$. The most widely used form of the functional F is constructed by Perdew, Burke and Ernzerhof (PBE) in 1996 [180, 181].

The combination of exchange energy and correlation energy forms the applicable functional. For instance, PBEPBE is the pure form of the PBE functional with the combination of equal weights of exchange and correlation functional. A popular correction functional which is derived from the correlation energy expression of the helium atom is the functional by Lee, Yang, and Parr (LYP) [186]. The functionals whose exchange part with Becke's functional [187] and the correlation part with Perdew's functional in 1986 [188] or LYP functional, are BP86 or BLYP, respectively.

In practice, the exchange functional tends to be weighed stronger than the correlation part. Thus, the accurate expression for the exchange energy is important, which can be accomplished by mixing the calculated exchange part (with Hartree-Fock approximation) with those obtained from DFT methods. These functionals are referred to as the hybird functionals. The B3LYP functional, as an example, was developed by Frisch in 1994 [189]. It was constructed based on the Becke's three-parameter hybrid functionals [190] which is denoted as

$$E_{xc} = (1 - A) * E_x^{VWN} + A * E_x^{HF} + B * \triangle E_x^{Becke} + E_c^{VWN} + C * \triangle E_c^{non-local}, \tag{2.34}$$

where E_{xc} stands for the exchange-correlation energy, accordingly E_x and E_c represent the exchange energy and the correlation energy separately. $A = 0.2$, $B = 0.72$ and

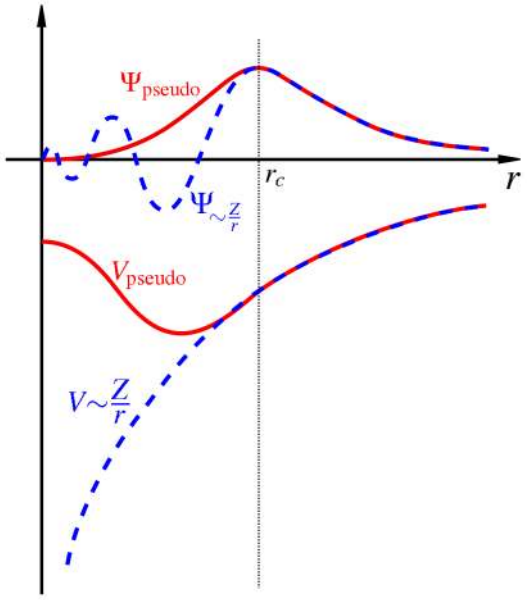

FIGURE 2.11: The wavefunction in the Coulomb potential (blue) and the pseudopotential (red) of the nucleus. The pesudo wavefunction and potential match the all-electron ones above a certain cutoff radius $\mathbf{r_c}$. Figure is adopted from [192].

$C = 0.81$ are the constants determined by Becke [189]. B3LYP is a variant of this hybrid functional that consists of the non-local correlation term provided by the LYP expression and the VWN functional III [185] as the local correlation term in the percentage of 81% and 19% separately [189]. Accordingly, the expression of the correlation functional is

$$E_c^{B3LYP} = C * E_c^{LYP} + (1 - C) * E_c^{VWN}. \tag{2.35}$$

As a result, the exchange-correlation energy of the B3LYP functional becomes

$$E_{xc}^{B3LYP} = (1-A)*E_x^{VWN} + A*E_x^{HF} + B*\triangle E_x^{Becke} + C*E_c^{LYP} + (1-C)*E_c^{VWN}. \tag{2.36}$$

2.4.4 Pseudopotenital

The N-electron Schrödinger equation Eq. (2.21) can be simplified by dividing the electrons into two groups: inner core electrons and valence electrons. The electrons in the inner orbitals are tightly bound and do not play an important role in the chemical binding of atoms. Binding properties are mostly related to the valence electrons, especially in semiconductors and metals. Thus, the Coulombic potential terms in the Schrödinger equation which describes the inner electrons and the nucleus can be replaced with an effective potential, or so called pseudopotential. The pesudopotential approximation was first proposed by Fermi in 1934 [191].

As illustrated in Fig. 2.11, the pesudo wavefunction and potential match the all-electron ones above a certain cutoff radius $\mathbf{r_c}$. With this approach, the time and memory costs

to perform calculations are significantly reduced, while preserving the accuracy of the results. Pseudopotentials with large cutoff radius are assumed to be softer, namely faster to converge but less accurate to simulate realistic properties in various environments. Therefore, pseudopotentials which reduce the size of basis set and the number of electrons, at the same time fit well with the realistic features have been developed. Among them, the norm-conserving pesudopotential [193] and the ultrasoft pesudopotential [194] are the most common forms used in quantum chemistry and solide-state physics software packages.

2.4.5 Basis Set

A basis set in DFT is a set of basis functions that are used to represent the electronic wave function in order to turn the partial differential equations of the molecular model into algebraic equations which are suitable for efficient computing. The molecular orbitals are expressed as linear combinations of the basis functions.

The basis set can either be composed of atomic orbitals, or plane waves which are typically used within the solid state community. Several types of orbitals can be used: Gaussian-type orbitals (GTOs), Slater-type orbitals (STOs), and numerical atomic orbitals. The smallest basis set is called minimal basis set. A minimal basis set includes the basis functions of each atom in the molecule. For example, the basis set of each atom in the second row of the periodic table (Li-Ne) contains five functions (two s functions and three p functions). Additional functions are added to the minimal basis sets to describe the polarization of the electron density of the atom which are called polarization functions. To accurately describe anions, dipole moments or intra- and intermolecular bonding, the so called diffuse functions are added which extent the GTOs with a small exponent to shrink the portion of atomic orbitals that are far away from the nucleus.

Chapter 3

Experimental and Computational Methods

Within this thesis, both experimental and theoretical methods were used for the combined study of electronic and vibrational properties of single-molecule junctions. Initially, a detailed description of the self-built molecular junction spectroscopy (MJS) set-up is presented. Thereafter, the preparation procedures of the tip and substrate are introduced. Then the used experimental procedures are elaborated. Afterwards, the theoretical methods and the essential calculation process are explained. The final part discusses the algorithms contained in a self-developed data analysis software.

3.1 Set-up

The set-up, which allows us to simultaneously investigate electronic and optical features of metal-molecule-metal junctions in strong optical field, is called a molecular junction spectroscopy set-up. Fig. 3.1 illustrates the overview of the self-designed and assembled set-up. It consists of a ultra-high-vacuum (UHV) chamber in where the experiments are performed and a laser optical system which enables the excitation and collection of Raman signals of the molecules. Part of the optical system is assembled on the top of the chamber and connected to the remaining part by a multi-mode optical fiber. There is a CF40 sized window at the front side of the chamber, from where the kernel part of the device can be viewed.

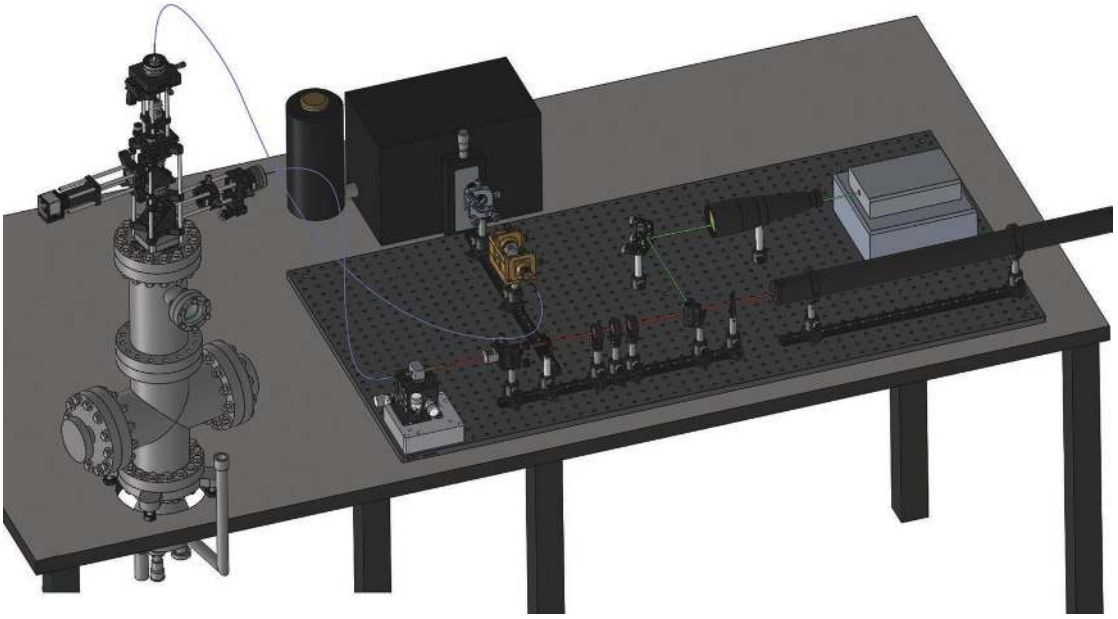

FIGURE 3.1: Overview of the self-built set-up. Besides the electrical equipments to characterize the formed junctions, the set-up mainly consists of a vacuum chamber and an optical system.

Fig. 3.2 presents the components of the set-up. A helium flow cryostat ② (Cryovac Konti-Kryostat UHV) is mounted to the CF100 sized chamber from the bottom. Liquid helium/nitrogen circulation system can be connected to the openings in the cryostat to realize low temperature experiments down to ca. 30 K. A differential screw goes through the cryostat and is connected to the sample holder ①, which is fixed on the top of the cryostat, to adjust the distance between the tip and substrate in a precision of lower μm range by manually turning the knob ④. At the middle section of the chamber, the pumping system including a turbomolecular pump and a rotory pump is connected to one side of the chamber. The UHV chamber is continuously pumped to ensure a base pressure in the lower 10^{-7} mbar range at room temperature, which is sufficient to reduce surface contamination and prevent the molecules from oxidation in the presence of strong optical fields [195]. At the other side of the chamber, a titanium sublimation pump (TSP) ③ is mounted. The base pressure in the UHV chamber can be reduced to the lower 10^{-8} mbar range by applying a current of 40 A to the filament of the TSP for 60 s every four minutes and repeatedly.

As shown in Figure 3.3a, there are two light sources in the optical system, namely the He-Ne laser (Thorlabs HNL225R-EC, 632.8 nm, 22 mW) and the Nd:YAG laser (Coherent Compass 315M, 532 nm, maximum 150 mW). Laser line filters are installed in front of the lasers to eliminate the side bands of the lasers. For example the He-Ne laser, only the light with a wavelength of 632.8 nm can pass through the filter. Two parallel mounted mirrors guide the laser beam from the Nd:YAG laser (green line) into the optical pathway (red line). The mirror at the joint position of the two laser beams is

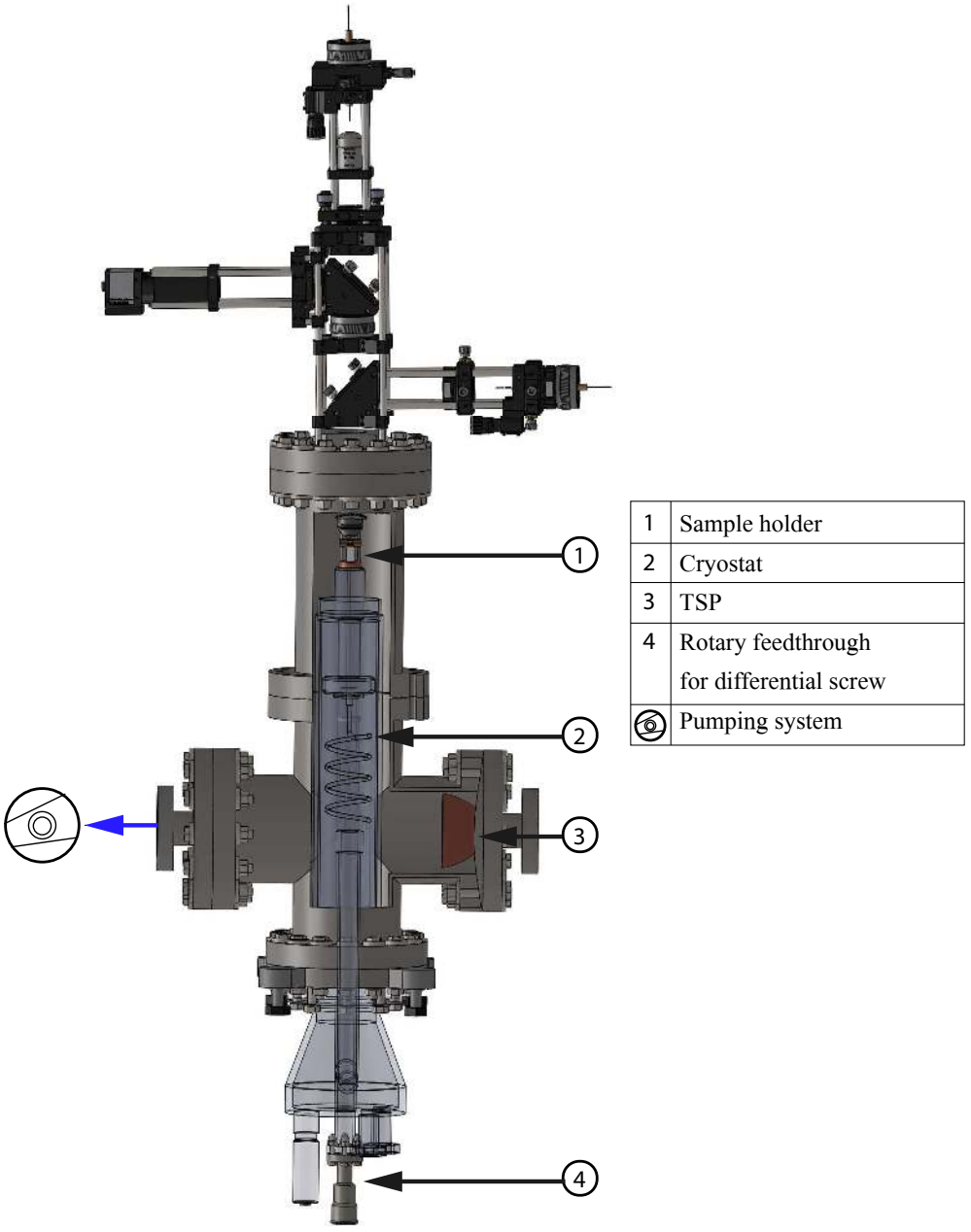

FIGURE 3.2: Section and phantom views of the UHV chamber.

magnetically attached to a holder which can be easily dismounted when the He-Ne laser is used. Three switchable neutral-density (ND) filters, which reduce the beam power to 1%, 10% and 50%, as well as an iris diaphragm are successively installed along the optical pathway to adjust the the power of the incident light. Subsequently, the laser beam is converged to a multi-mode optical fiber by a 4X objective. The light gets out at the other end of the fiber which is connected to the optical system on top of the UHV chamber (Fig. 3.3b) and is collimated by a convex lens. The paralleled light is then reflected by a 45 degree assembled dichroic beam-splitter, perpendicularly through a quartz viewport into the UHV chamber. Inside the chamber, a 100X objective is

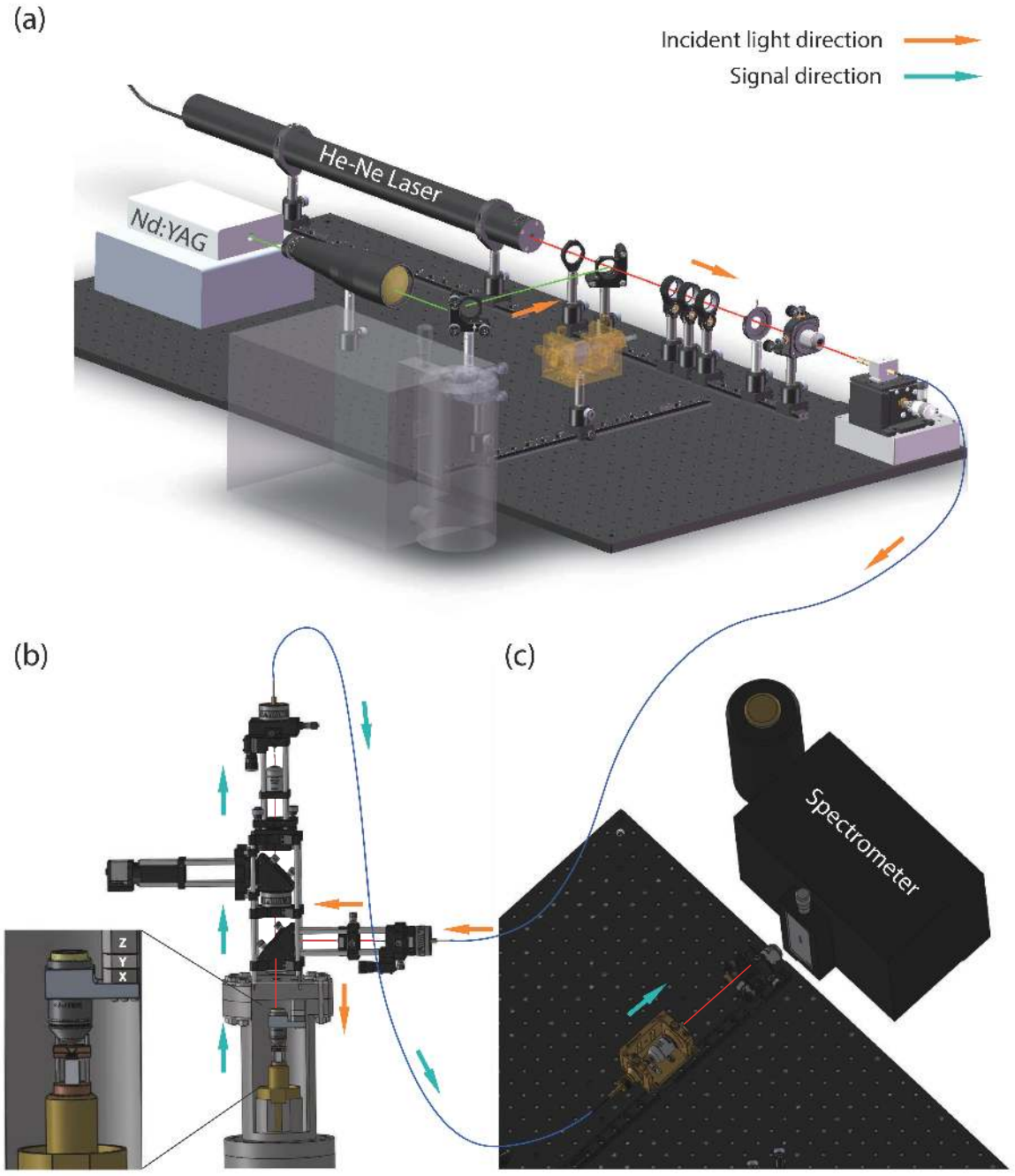

FIGURE 3.3: Illustration of the optical system. (a) The excitation light part of the optical system. (b) The optical part on the top of the vacuum chamber. (c) The signal detection part. The orange colored arrows indicate the propagation direction of the incident light, and the lightgreen arrows point out the traveling direction of the scattered signal.

mounted on a compact actuator system, which enables the objective to move in x-, y- and z-direction with a minimum stepsize of 1 μm in a travel range of 5 mm (Fig. 3.3b enlarged) to focus the laser on the sample.

The scattered light from the sample is then collected through the same objective. Consequently, the inelastically scattered light is separated from the reflected incident light by the already mentioned dichroic beam splitter. The inelastic scattered light can pass through the beam-splitter while light with the same wavelength as the incident laser beam is reflected. Afterwards, the scattered light propagates through a lens and is collimated. A 45 degree mounted low-reflective mirror is on the top of the lens to reflect a small quantity of the scattered light to the CCD camera installed as a side branch horizontally (Fig. 3.3b). From real-time imaging of the CCD camera, one can determinate the focal plane of the movable objective and guide the focal point to the apex of the tip. Back to the light pathway, a notch filter which eliminates more than 99.5 % of the reflected laser light is mounted above the low-reflective mirror. Afterwards, the signal is focused by a 10X objective and guided into a multi-mode optical fiber. After the transmission through the fiber (Fig. 3.3c), the signal is refocused by a 10X objective and then collimated by a 4X objective into the spectrometer (Princeton Instrument SP2300i) for optical analysis.

A source-meter (Agilent E5273A) supplies a DC bias voltage and measures the current in the circuit which consists of the tip, the substrate and the target molecules. The voltage range of the source-meter is 1 mV to 10 V and the current accuracy is about 5 pA. A self-built digital to analog converter (DAC) is used to pattern the voltage applied to a piezo (section 3.2) which controls the tip-substrate distance.

3.2 Sample Preparation

In order to change the samples in the UHV chamber, the chamber is first purged by nitrogen and then carefully opened at the middle of the chamber. As shown in Fig. 3.4, the sample holder is mounted on the top of the helium cryostat. The top part, which can be adjusted by the differential screw ④ and is constraint by three guiding rods ⑤, serves as the tip holder. A glass slab is attached on the 45 degree slope of the tip holder as a isolation medium. A triangular shaped tip ① is mounted on the top of the glass slab. A high precision piezo (Physical Instruments Picma P-877.31) ③ is mounted on the base slab of the sample holder to adjust the distance between the tip and the substrate. The maximum elongation of the piezo is 8.446 μm when a voltage of 90 V is applied. A $5 \times 5 \times 1$ mm^3 magnet is attached to the top of the pizeo in order to magnetically fix the iron substrate holder on which a gold coated substrate ② is glued with colloidal silver. The piezeo can only elongate in z direction and movements in x and y directions to scan the surface have been sacrificed to ensure the stability of the system. The tip and the substrate serve as the electrodes as introduced in section 2.1.

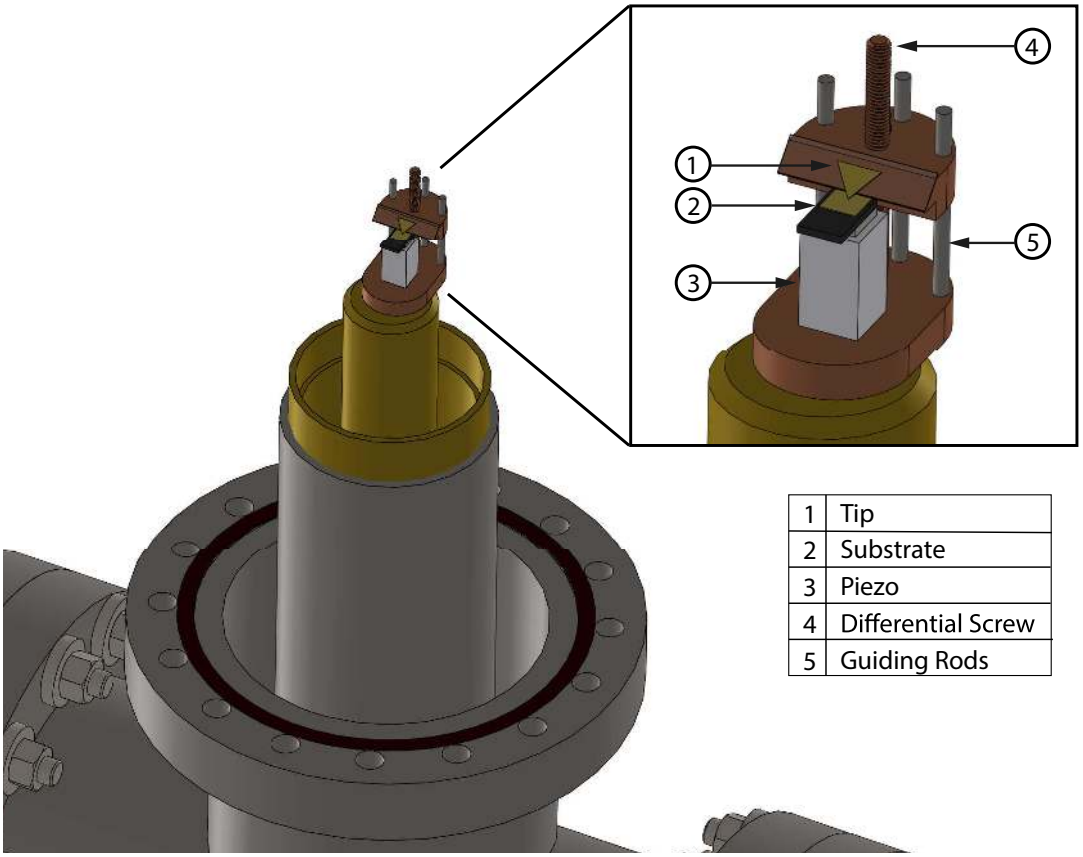

FIGURE 3.4: The Sample holder is mounted on the top of the helium cryostat. The enlarged image shows the kernel of the device, reproduced from [85].

3.2.1 Fabrication of T-tip

The tip is a tetrahedral glass fragment covered with noble metal (gold in this thesis) film which serves as an electrode, light transmission path and TERS hotspot. It is called T-tip due to its tetrahedral geometry [196]. The T-tip was first introduced in 1994 by Fischer [197] as an aperture-less SNOM probe. The T-tip is made from a standard Soda-lime glass sheet (thickness 150 μm). Firstly, the glass sheet is put on a heating plate and heated to $100 - 120\ ^{\circ}C$ for 10 minutes to eliminate water on the surface and to prevent adsorption of contaminates during the next preparation steps. Subsequently, it is cleaned with a CO_2 snow-jet. After cleaning, the glass is cleaved manually into a tetrahedral shape as illustrated in Fig. 3.5a. Then the glass tips are placed in to an electron beam physical vapor deposition chamber [198] to obtain a metal coating. The chamber keeps a base pressure in the 10^{-8} mbar range, in which gold in the crucible gets vaporized. In this way, a well-defined thickness ($\sim 20\ nm$) of gold coating can be formed on the tips to make them conductive while preserving the transparency. As shown in Fig. 3.5b, three facets that join to the apex are covered with gold layers. During the experiment, the laser beam passes through the glass body of the tip and focuses on the apex. In the end, the tips are inspected by the scanning electron microscope (SEM) in

the scale of 10 μm and 200 nm (Fig. 3.5c) respectively, to check the quality of the tips. Defective tips are labeled and will not be used in the experiments.

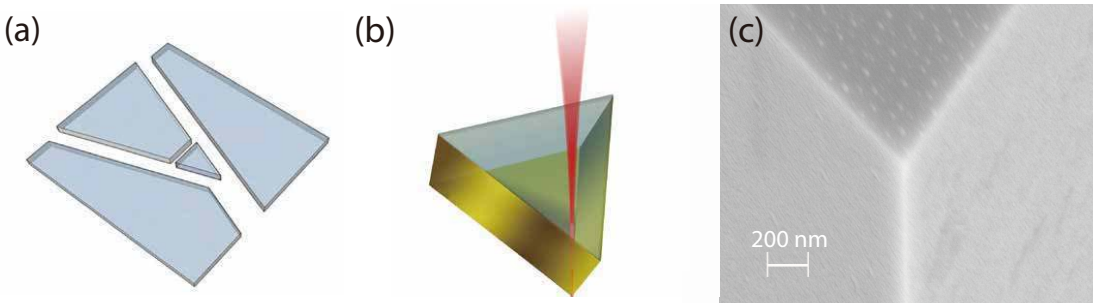

FIGURE 3.5: Fabrication of the tip. (a) Tip fabrication procedure, adopted from [86]. (b) Tip coated with gold film, the laser beam pass through the glass body of the tip and focused on the apex. (c) SEM image of a T-tip in 200 nm scale.

3.2.2 Deposition of Molecules

The substrate is a glass sheet coated with gold film of $300-500$ nm with a roughness of about 50 nm. To improve the adhesion of gold, ~ 50 nm titanium is initially evaporated on the glass as primer material [199], then the gold layer is thermally evaporated.

Two different deposition methods are used based on the type of the molecular anchor groups. The first approach is a variation of the drop-casting method [200]. A droplet of the molecule solution (about 10^{-3} mmol in THF) is deposited with a pipette on a 5×5 mm^2 gold covered substrate. Then the substrate is put in an atmosphere saturated with the solvent tetrahydrofurane (THF) for 3 hours. In this time, a self-assembled layer of covalently anchored molecules forms on the substrate. Afterwards, the substrate is rinsed with the solvent to get rid of the unbound molecules from the surface. Alternatively, for the alkanethiol molecules ($R-SH$), whose terminal group has a strong affinity to gold, in order to shorten the deposition time, the substrate is wetted with a droplet of molecular solution (40 μL) in ambient conditions. The solvent is then evaporated from the substrate under a stream of nitrogen. This process is repeated for $5-6$ times to increase the molecular density on the substrate. In the end, the substrate is rinsed with solvent (500 μL) for 5 times to remove the not covalently bound molecules.

When thioester molecules ($R-S-CO-R'$) are studied, the substrate is dipped into the molecular solution to form self-assembled monolayers (SAM) as illustrated in Fig. 3.6. Within the incubation time, the acetyl protection groups ($-C(O)CH_3$) of the molecules split off and the sulfur covalently bonds to the gold surface. In this approach, several parameters of the process should be well controlled to obtain reproducible SAMs. At a temperature above 25 $^\circ C$, the rate of adsorption can be improved and especially in the first few minutes most of the adsorption and reorganization of the SAM are taking place [201, 202]. Considering the boiling point of THF (66 $^\circ C$), the solution in which the substrate is immersed is heated up to 55 $^\circ C$ for 15 minutes and then spontaneously

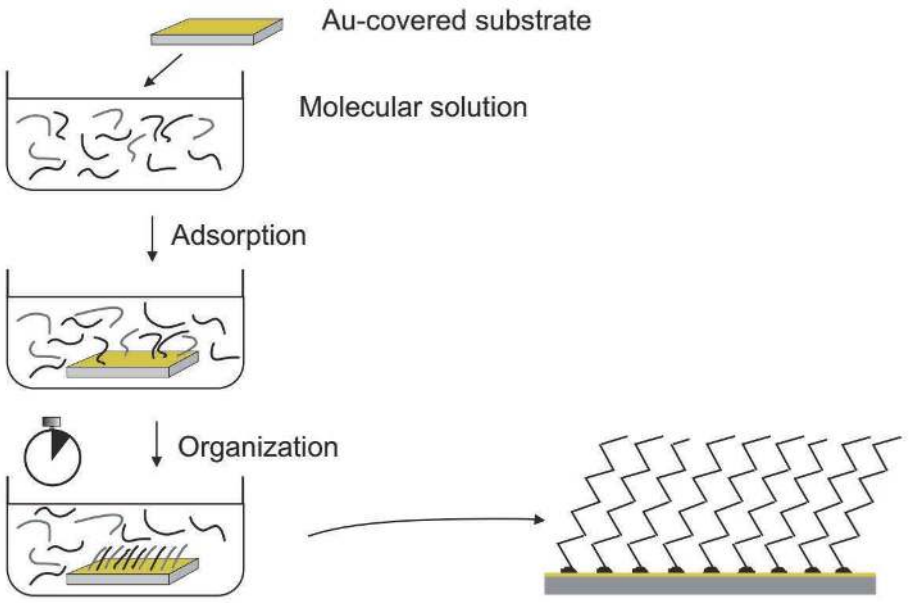

FIGURE 3.6: The procedure of forming SAM. The substrated is immersed into the molecular solution. The molecules adsorb on and covalently anchor to the substrate. Within the incubation time, the molecules on the substrate organize into a SAM. Figure is reproduced from [105].

cool down. Besides, concentration and immersion time are contrary related, namely a lower concentration of the molecular solution requires a longer immersion time [203, 204]. In our experiments, for a solution with a concentration of 1 mM, the immersion time to form desired SAM is about $12 - 18$ hours at room temperature [199]. Before being mounted to the sample holder, the substrate is rinsed with THF to remove the molecules not bound to the surface.

3.3 Experimental Procedures

A fresh prepared substrate and a new T-tip are first mounted in the UHV chamber. The experiments should only be performed when the base pressure in the chamber is lower than 5×10^{-6} mbar. There should be no other light sources than the laser during the optical measurements.

Manual Approach. For a start, the tip holder is manually controlled by the differential screw to shorten the tip-substrate distance, until the working distance of the piezo is reached. This process is monitored by a self-built tunneling electronic feedback loop. The piezo which is underneath the substrate is initially set to its fully elongation by applying a voltage of 90 V. When the tunneling current threshold is reached, the voltage applied to the piezo is reduced to shrink it to keep a proper distance between the tip and the substrate as well as prevent the tip from crashing on the substrate. Afterwards,

the tunneling electronic is switched off. From now on the voltage of the piezo and the current measurement can be controlled by a computer program.

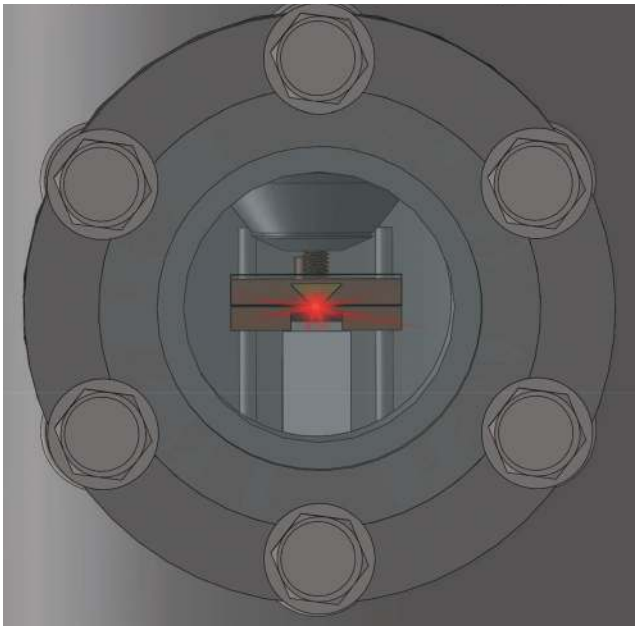

FIGURE 3.7: The sight from the side window. When the laser illuminates on the apex of the tip, a spark can be observed through the window.

Tip Focusing. When the tip-substrate distance is in the working range of the piezo, the laser is switched on and the beam power is attenuated to 1% by flipping a ND filter into the light pathway. The laser light is reflected by the substrate and projected on the CCD camera. Through the real-time imaging of the camera, one can control the movable objective mounted in the chamber to focus the laser beam on the substrate. The radius of the focal spot is about 5 μm. A lamp is attached to the side window on the UHV chamber to increase the brightness of the image. Subsequently, the focal spot is moved by shifting the x-, y-positions of the objective to search the tip. When a brighter area becomes visible instead of the focused spot in the CCD image, the laser beam is supposed to illuminate the tip. Then the objective is moved along the edge of the tip to the apex, in which case a glaring spark at the tip apex can be observed through the side window as illustrated in Fig. 3.7.

Automatic Approach. The tip-substrate distance should be reduced to nanometer range in order to form a molecular junction. To this end, a bias voltage (about 1 V) is applied to the tip-substrate circuit and the piezeo voltage is sequentially increasing to drive the substrate towards the tip with a stepsize of 1 nm. The current in the circuit is measured simultaneously. When the current reaches a certain threshold (about 0.9 nA), a routine maintains the tunneling current to the threshold value by adjusting the piezo voltage continuously. Due to the translation of the substrate in z-direction, the laser beam needs to be refocused. Since the distance between the tip and the substrate is significantly smaller than the focal spot, the laser is considered to be focused on the tip-height as well.

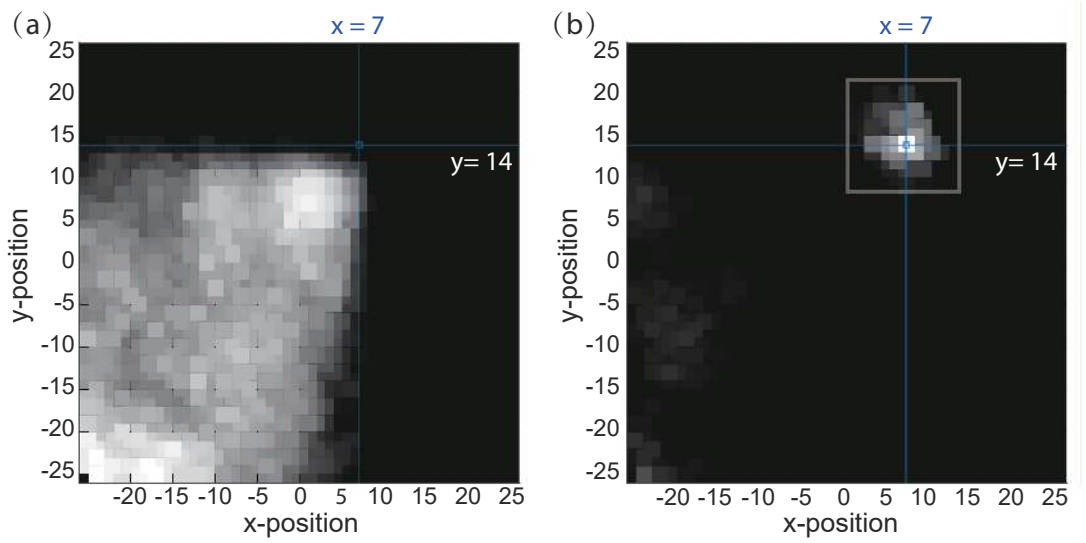

FIGURE 3.8: Scanned tip images. (a) The tip shape in a $50 \times 50\ \mu m^2$ scanned image whose apex localizes at [7, 14]. (b) The most intensive Raman signal with the wavenumber of 1400 $1/cm$ in the scanned area, the strongest signal localizes at [7, 14]. The white square indicates an area of $\sim 10 \times 10\ \mu m^2$.

Tip Scanning. To preciously locate the position of the tip apex and focus the laser beam on it, an automated program is used to control the objective to scan the tip. The actuator-driven objective is set to move horizontally in an area of $150 \times 150\ \mu m^2$ with a stepsize of 5 μm and a Raman spectrum is acquired at each step. Since the reflectance of the glass body of the tip is higher than the gold surface, the reflected incident light is more intensive on the tip. Thus, after the scan, the peak intensities at 0 cm^{-1}, the wavenumber of the laser light, represent a 2D image of the tip shape. According to the coordinates of the apex from the roughly scanned image, the objective position is reset and a fine scan is then performed in an area of $50 \times 50\ \mu m^2$ with a stepsize of 1 μm. Fig. 3.8a shows the tip shape at the wavenumber of 0 cm^{-1} and Fig. 3.8b shows the Raman signal at a wavenumber of 1400 cm^{-1}. The position of the apex in Fig. 3.8a fits well with the brightest location in Fig. 3.8b, which indicates that the tip is in a good functional condition. The white square in Fig. 3.8b indicates an area of $\sim 10 \times 10\ \mu m^2$, with the maximum enhancement at the center $1 \times 1\ \mu m^2$, in which the Raman signal is supposed to be the optimum. In addition, the z-direction displacement of the objective can also be assigned to the scan to find out the optimal focal plane.

***I-d* Measurement.** A newly developed LabVIEW program (Appendix A) based on Hasch's [85] enables the statistical investigation of the conductance of the molecule through current-distance (I-d) measurement. When light is focused in the enhanced region, a bias voltage is applied and the substrate is driven to approach the tip until a certain current threshold depending the bias voltage is reached. In this process, molecular junctions can be formed. Afterwards the substrate is retracted until the current is down to the noise level ($< 0.1\ nA$). The current as a function of the tip-substrate distance is recorded (I-d curve). By repeatedly performing thousands of I-d measurements,

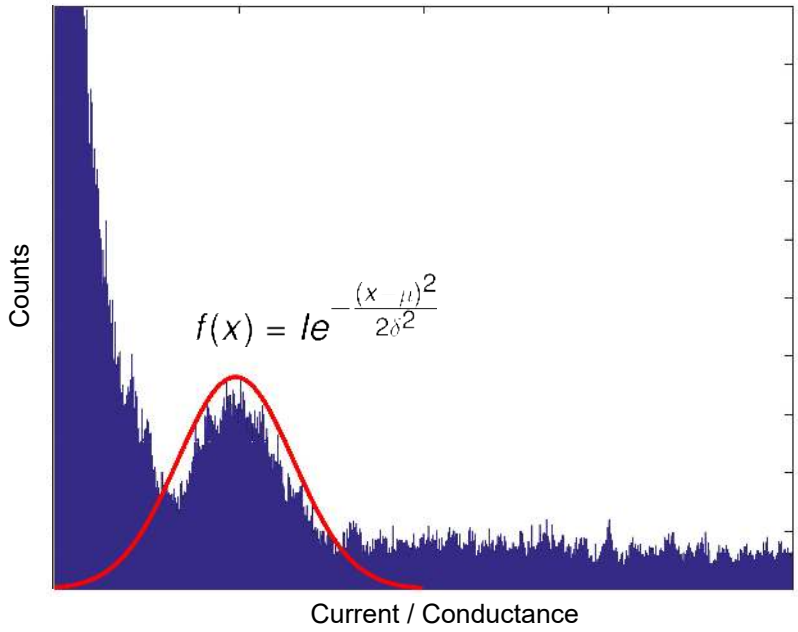

FIGURE 3.9: Illustration of a current/conductance distance histogram. A distinct peak indicates the conductance of a molecule or the current in a single-molecule junction.

one can construct a current-distance histogram which can be easily fitted with a normal distribution (Fig. 3.9). Thus, the current in a single-molecule junction at a certain bias voltage and the corresponding conductance of the molecule can be determined through a current/conductance-distance histogram.

Junction Investigation. Once the current in a molecular junction at a certain bias voltage is determined, the tip-substrate distance can be manually controlled to keep the current around the certain value. A stabilization time for the piezo is needed to reduce the drift and the creep. According to experiences, if a sudden increment in the junction current appears and the current becomes stable, a molecular junction is supposed to be formed. In this condition, current-voltage characteristics (I-V) can be measured by recording the current while sweeping the bias voltage from e.g. $-1.5\ V$ to $+1.5\ V$ in 200 discrete steps. Meanwhile, the Raman spectra can be recorded to investigate the vibrational properties of a molecule in the junction. According to previous studies [85–88], at different bias voltages, the Raman spectra exhibit diverse properties.

Junction Stretching. As a kernel part of this thesis, a stretchable molecule is studied by pulling the junction through increasing the distance between substrate and tip (section 4.3). This approach is realized by the automated LabVIEW program introduced in Appendix A. The Raman spectra are recorded simultaneously with the current-distance (I-d) characteristics, meaning that a spectrum is acquired after each displacement of the substrate. As a results, in a complete loop including approach and retraction, the vibrational frequencies of the molecule can be analyzed as a function of the tip-substrate

distance. If a *I-d* curve indicates that a junction is formed, the corresponding spectra might reveal the tension related vibrational properties of the molecular junction.

3.4 DFT Calculations

In this thesis, two molecular dynamics simulation programs are used: the *Gaussian 09W* software package [205] and the *SIESTA* package [206]. The former is a general purpose quantum chemistry software package which was initially released by Pople and his research group in 1970 [207]. It was used in this thesis for DFT calculations of isolated molecule models in gas phase. The atoms in the ends of the molecules have been constraint to simulate the bonding condition of a molecular junction. Due to the ease of use, *Gaussian* is used for the preliminary theoretical studies. *SIESTA*, the acronym of *Spanish Initiative for Electronic Simulations with Thousands of Atoms*, is applied for the molecular junction simulations containing both the molecule and the electrodes.

Initially, a molecular model with the Cartesian coordinates of the atoms is constructed. For *Gaussian*, effective core potentials are used to freeze the core electrons, the build-in DFT functionals (e.g. B3LYP, PBEPBE) as well as basis sets (e.g. Pople basis [208], correlation-consistent basis [209]) can be chosen to perform the calculations. As to *SIESTA*, norm-conserving pseudopotentials in nonlocal form are used. It uses the Kohn-Sham self-consistent method in the local density approximation (LDA) as well as the generalized gradient approximation (GGA). The atomic orbitals of each atom in the molecule are combined as a basis set.

When the parameters are assigned, the self-consistent field (SCF) procedure is performed as illustrated in Fig. 3.10. The initial charge density is created based on the assumption that there is no interaction between atoms, meaning that the total electron density is simply the summation of the charge densities. Subsequently the effective potential is calculated, which includes the external potential and the effects of the Coulomb interactions between the electrons. By solving the Kohn-Sham equations, a updated electron density is obtained. If the convergence criteria is not reached, the procedure is repeated with calculating the effective potential. Finally, the ground state energy for a given molecular configuration is obtained through the SCF procedure. Afterwards, other properties such as the forces, geometry are generated. The conjugated gradient method is used to minimize the ground state energy and to obtain the optimized geometry of the molecular model. The coordinates of the optimized atoms are extracted to set up an input file for the calculation of vibrational frequencies.

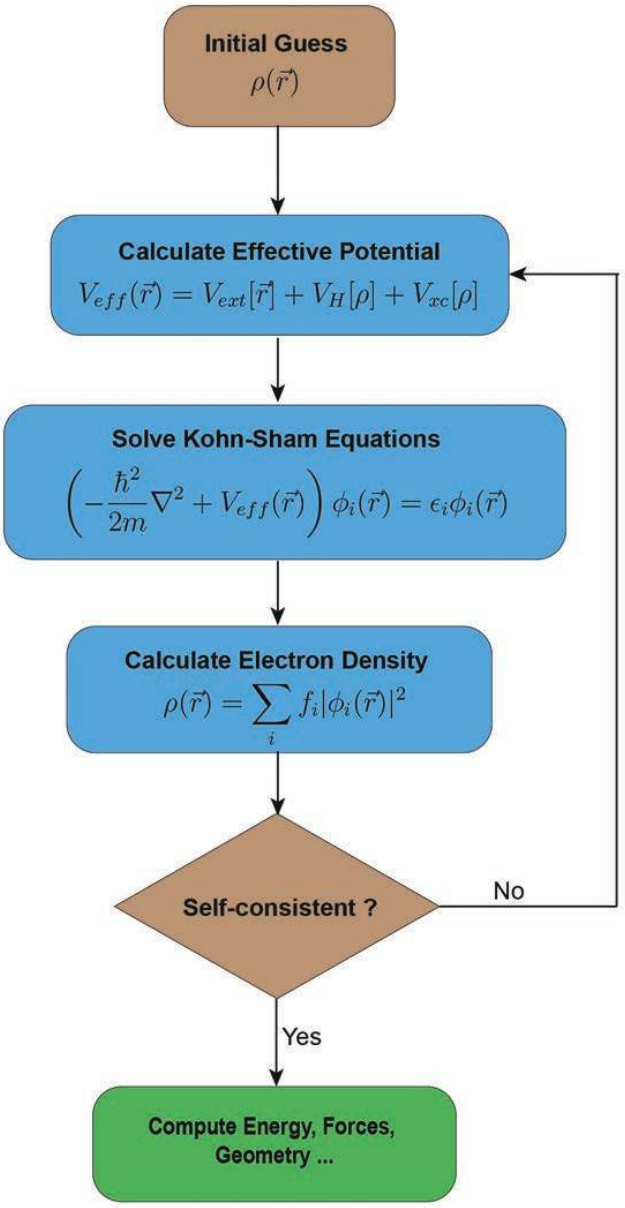

FIGURE 3.10: Schematic of the self-consistent field procedure.

3.5 Data Analysis

To facilitate the data analysis process, the self-developed software contains a spectra viewer tab, a *I-d/I-V* viewer tab and a peak fitting tab. A detailed description of the software is attached in Appendix B. In general, a measured Raman spectrum is composed of a signal, a noise component and a background. The background of the Raman spectrum varies slowly with the wavenumber of the signal. In order to systematically extract the features from the spectra, an uniform baseline correction method to process a series of spectra is necessary. Therefore, the rolling-circle filter (RCF) is used in this thesis to subtract the baseline of the spectra. To study the peak characteristics

(i.e. intensity, peak position and full width at half maximum (FWHM)) in a spectrum, nonlinear regression is applied to fit the peaks with a Lorentzian distribution.

3.5.1 Baseline Correction

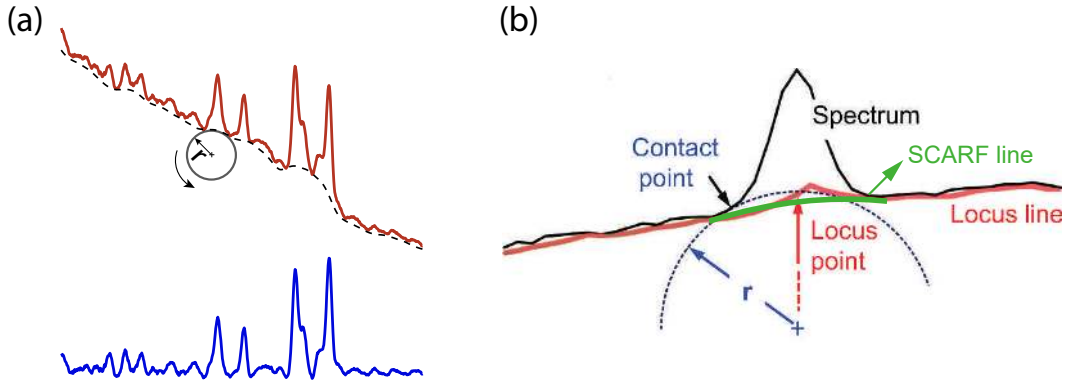

FIGURE 3.11: RCF on an example spectrum. (a) A circle rolls along the raw spectrum and its path defines the baseline (Locus line). (b) The filter tends to roll into the peak and overestimates the background level. This deficiency can be overcome by applying a Savitzky-Golay-filter on the locus line. Figure is adopted from [210].

The rolling-circle filter was proposed by Mikhailyuk in 2003 [211] and further optimized by Brandt in 2006 [212]. As suggested by its name, it treats the spectrum as a rigid surface and rolls a circle of radius r along the bottom side as illustrated in Fig. 3.11a. The radius r is significantly larger than the peak widths and much smaller than the curvature radius of the background. Starting from the first point in the spectrum array, the abscissa of the center of the circle coincides with the corresponding point. While rolling the circle, the spectrum has at least one common point with the circle. The ordinates of the circle should be smaller than or equal to the corresponding ordinates of the spectral fragment, which ensures that the circle lies below the spectrum. The path of the circle along the spectrum defines the baseline. After baseline correction, the Raman peaks remain mostly unchanged.

The efficiency of the background subtraction can be evaluated by the ratio of the areas between the original (S_0) and corrected spectra (S). By analyzing the dependence of the ratio S_0/S on the radius r, the appropriate radius of the circle can be decided. In principle, the larger the ratio S_0/S the better the efficiency, and accordingly corresponding to a smaller radius. Nevertheless, if the radius is smaller than the bottom width of a peak, the circle falls into the useful signal bands, which causes a decrease of the peak intensity (Fig. 3.11b). However, simply increasing the radius of the circle not only decreases the efficiency, but also does not fully solve the problem. This deficiency can be overcome by applying a Savitzky-Golay-filter [213, 214] to the obtained baseline (Locus line in Fig. 3.11b) from the SCF process, which smooths the baseline without distorting

the values too much. Accordingly, the filter is also called Savitzky–Golay coupled advanced rolling-circle filter (SCARF) [210]. According to Brandt's study [212], the best radius for Raman spectrum is 130 cm^{-1}.

3.5.2 Peak Fitting

According to quantum theory, electrons in molecules occupy well-defined energy levels. When a molecule absorbs or emits vibrational energy, the transitions between the energy levels occur in well-defined discrete quanta, which gives rise to a sharp vibrational spectrum. However, most vibrating molecules exist in a bath of the environment, meaning that the molecules interact with the environment which promotes slightly different vibrational frequencies for each molecule. In gas phase, where these interactions happen often, the resulting peak shape is a Lorentzian profile [215, 216] which has a sharp center and long tails. In spectroscopy, a Lorentzian function with three-parameter is often used

$$f(x; x_0, \gamma, I) = I \left[\frac{\gamma^2}{(x - x_0)^2 + \gamma^2} \right], \tag{3.1}$$

where x_0 is the position of the peak, γ represents the FWHM and I is the peak intensity.

Nonlinear regression can be expressed as

$$Y = f(X, \beta) + \epsilon, \tag{3.2}$$

where f is the nonlinear function whose parameter vector β can not be expressed in a linear combinations with the independent variable X and ϵ is an error term. In this thesis, f is the Lorentzian function Eq. (3.1) and $\beta = [x_0,\ \gamma,\ I]$ contains the peak position, the FWHM and the intensity of a peak. The weighted least squares equation

$$Q = \sum_{i=1}^{n} w_i [y_i - f(x_i, \beta)]^2 \tag{3.3}$$

is solved with the Levenberg–Marquardt algorithm [217] in order to find the optimum parameters $\hat{\beta}$ which best fit a peak with corresponding Lorentzian distribution

$$\hat{\beta} = arg \min_{\beta} Q. \tag{3.4}$$

In practice, an initial Lorentzian distribution model $f(X, \beta_0)$ is built with preliminary estimated parameters β_0 in the Raman shift range of interest X_0, and the corresponding intensity values Y_0 are accordingly exported. By solving the least square equation Eq. (3.4), the fitting parameters are determined. The illustration of the result of this fitting procedure is presented in Fig. B.4 in Appendix B.

Chapter 4

Results and Discussion

In this chapter, results of three independent projects obtained by the MJS technique are presented and discussed. Further insights are given by employing the DFT calculations. Initially, a rigid bis-phenylethynyl-anthracene molecule exhibits vibrational excitations provoked by charge-vibrational coupling is investigated. Secondly, a molecule with a ter-phenyl backbone with methyl substituents together with its non-methyl analogue are studied. The molecule turned out to be switching its conformation induced by the bias voltage (published in [88]). Finally, a helically-shaped hept-phenyl backbone molecule has been demonstrated to exhibit vibrational shifts related to tension. In all studies, the experimental investigation of the electronic and optical properties are accompanied by structural and vibrational simulations to develop a coherent picture.

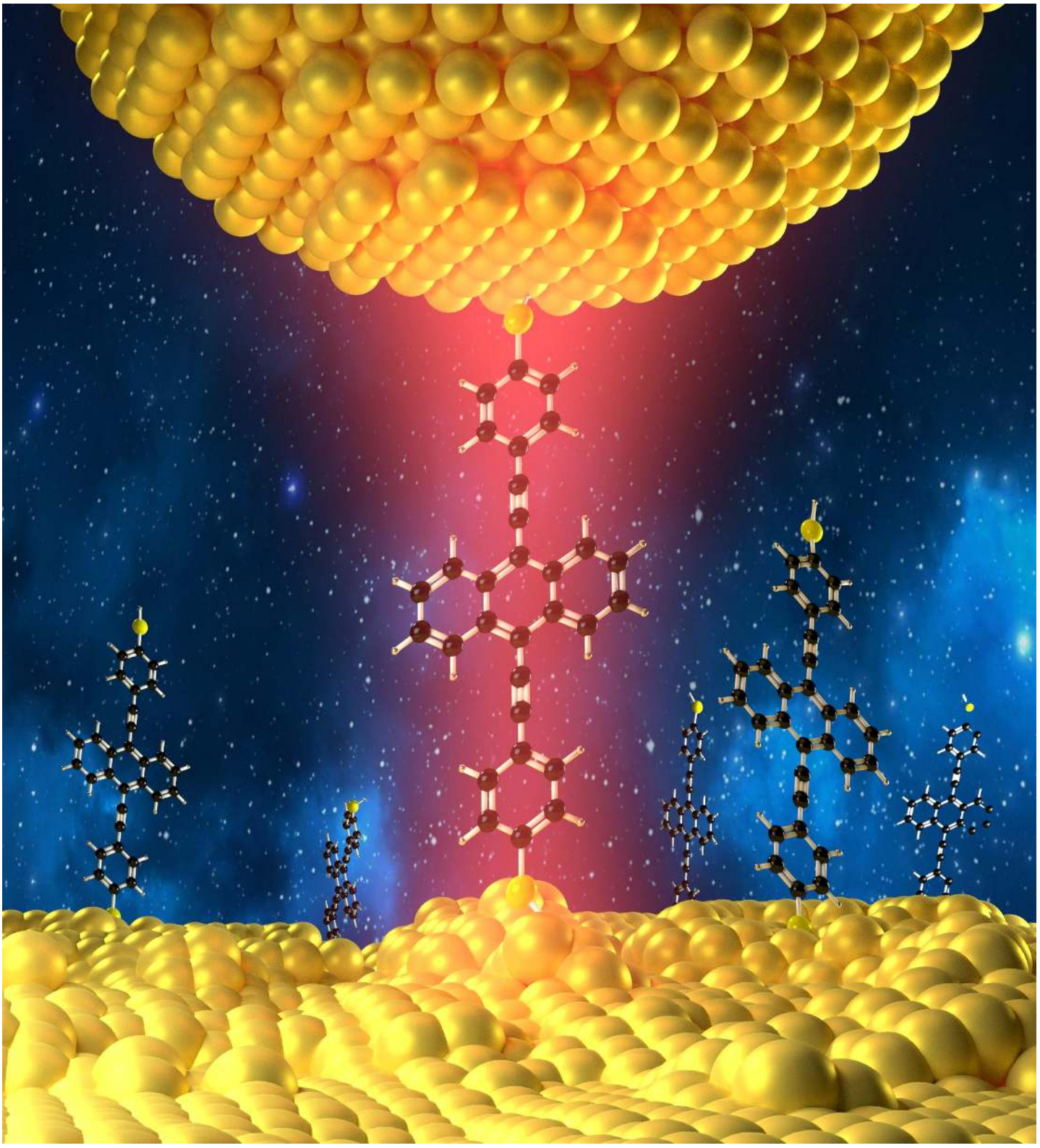

4.1 Vibrational Excitations in Current-Driven Single Molecule Junctions

Understanding loss mechanisms during charge transport through single molecules is fundamental for the development of (macro-)molecular circuitry [218–220]. During conduction through single molecules, electrons from an electrode material can transfer through the (vibrationally excited) molecular states and out into the unoccupied states of a second lead. In metal-molecule-metal junctions, where π-conjugated single molecules may show conductances near 0.5 μS [42, 221–223], electrode-molecule and electron-phonon coupling [224] (or more accurately, charge-vibrational coupling) plays an important role in the resistivity [42, 225–229]. Thus, control over charge-vibrational coupling would enable the optimization of a wide range conductance properties [219], e.g. enhancement or suppression [230, 231] of dissipation.

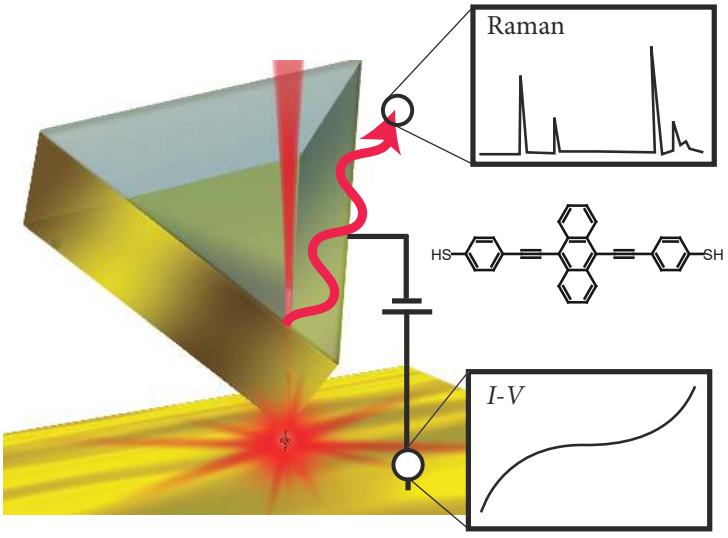

FIGURE 4.1: The MJS setup illustrating a single BPA molecular junction with gold contacts.

In this project, we study the steady-state vibrational distribution during current transport of a single 9,10-bis-phenylethynyl-anthracene (BPA) molecule immobilized with terminal thiol anchor groups (Fig. 4.1). When applying a bias voltage, we record a gap region followed by an abrupt charge transport region above a certain threshold voltage. The Stokes Raman signal allows to unambiguously show that transport occurs through the HOMO and that the molecule can be modeled as transiently charged by DFT simulations during transport. In the transport regime, we detect an anti-Stokes Raman signal. We describe this spectrum by a steady state vibrational population proportional to the charge-vibrational constant times the current passing through the junction and coupled to internal and external relaxations. The internal relaxation rate is measured

in an independent experiment, by means of ultrafast UV excitation of BPA in dichloromethane and subsequent probing of the vibrational mode relaxation. This model yields a charge-vibrational coupling constant of $\lambda = 0.58$ for the lowest lying z-translation mode at 4.11 cm^{-1}, employing the measured internal relaxation of (37 ± 4) ps and current of 35 nA.

4.1.1 Current-Voltage Characteristics of Single-Molecule Junctions

To establish a molecular junction, the sample is carefully approached to the tip repeatedly until a molecular junction has formed. For all subsequent measurements the tip-sample distance was controlled manually by the piezo voltage. After a junction has formed, *I-V* characteristics are recorded which often reveal prominent features at ±0.6 V as shown in Fig. 4.2. A current histogram for a specific bias is generated by analyzing about 2500 conductance curves (insert in Fig. 4.2). A narrow conductance window of $1 - 300\ \mu G_0$ at 0.5 V is chosen to record the Raman spectra (see insert Fig. 4.2). These channels are associated with charge transport through one of the molecular orbitals which is known to accompany inelastic dissipation in the form of vibrational excitation [232]. Accordingly, we monitored these excitations by vibrational spectroscopy in the bias voltage range of 0 to ±1.2 V (Fig. 4.3a).

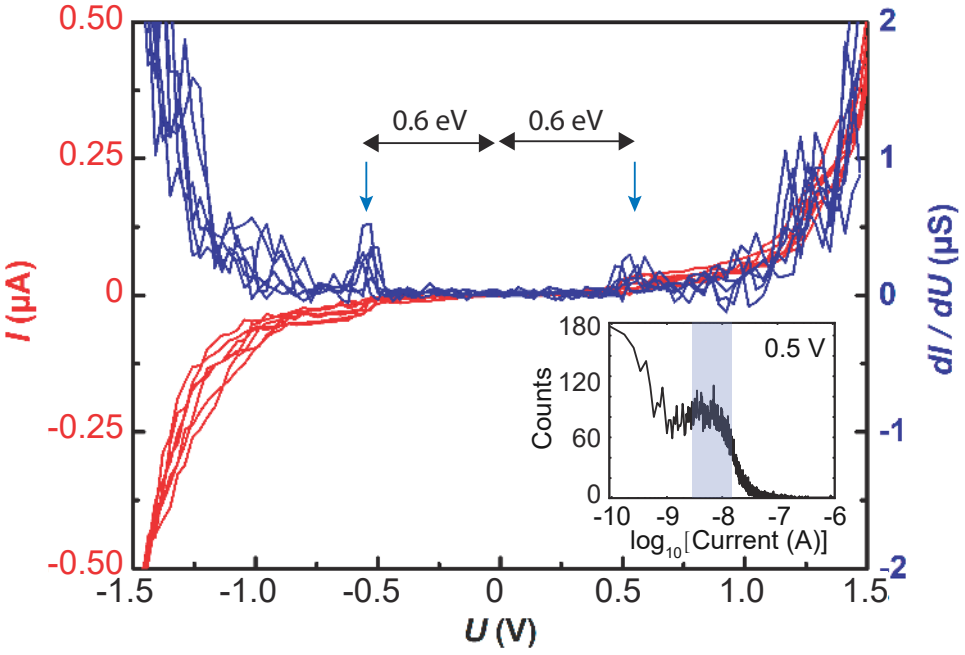

FIGURE 4.2: Typical processed *I-V* curves and the corresponding current derivatives (dI/dV) selected from a raw set of ∼2500 directly measured curves. The inset shows the histogram of ∼2500 *I-V* curves obtained at 0.5 V.

4.1.2 Single-Molecule Raman Spectroscopy

Raman spectroscopy measurements reveal no change in the Stokes spectra intensities at biases between 0 and ±0.6 V. Beyond ±0.6 V, a new sharp signal appears at 1400 cm^{-1} in the Raman Stokes spectrum (Fig. 4.3d). This is a strong indication that the current-carrying molecule is at the origin of the acquired Raman signal: an average Raman spectrum from the surrounding by standing molecules will not give rise to sharp, articulated current-induced Raman signatures. The new signals are understood from the simulated Raman spectra. The spectrum of the neutral species in general matches the experimental spectrum well, whereas the ∼2200 cm^{-1} has a displacement of ∼ 50 cm^{-1} to the higher frequency direction. The ∼1400 cm^{-1} signal is absent from the DFT calculated Raman spectrum of the neutral molecule (Fig. 4.3c) and is observed only for the charged state in Fig. 4.3e. Moreover, the 1400 cm^{-1} calculated intensity from a single molecule, coincides with the observed signal, corroborating the single molecule emitter concept. These observations notably suggest that BPA transiently charges during transport, characteristic of strong-polarization regimes [233, 234]. In addition, the spectra at negative biases exhibit the identical feature as the positive biases (Fig. 4.4).

Figure 4.5 shows several low-energy vibrational modes as well as the modes corresponding to the prominent peaks in the cationic spectrum (Fig. 4.3e). The modes are labeled as '**v**' for vibration and their corresponding peak positions. **v3** and **v11** are out-of plane modes. **v7**, **v49** and **v110** are in plane rocking modes of the center of gravity of the molecule which do not exist for the unrestricted molecular model. These low-energy modes could be of significant relevance for electron-phonon interaction induced by the electron flow through the molecule. One has to remark that changes in the Raman spectrum may not only be induced by changes in the polarizability due to changes in the charge state of the molecule but also by strain on the molecule within the junction. **v1226** and **v1530** are 'C-H' scissoring and rocking modes, which can hardly be influenced by these mechanisms. Thus the corresponding peaks almost remain at the same energy for different voltages. The vibrational modes **v1591** and **v1625** can be assigned to the rather wide peak around 1600 cm^{-1} in the experimental spectrum (see Fig. 4.3d). These modes are stretching modes of the anthracene group and the mercaptophenyl groups. **v1257** and **v1369** are 'breathing' modes of both the anthracene group and the mercaptophenyl groups. The **v2177** mode is the stretching mode of the 'C≡C' bonds.

Above the ±0.6 V transport resonance, an anti-Stokes Raman spectrum appears. Three important implications follow from the occurrence of this spectrum. First, a sharp step in the intensity at ±0.6 V, together with the absence of quadratic shifts, exclude charging-mediated Stark effects [233, 234]. Secondly, that this distribution does not change with applied bias (Fig. 4.6a), implies that the vibrational steady-state distribution cannot be attributed to resistive heating [235–237]. Thirdly, the anti-Stokes spectrum follows a non-linear decreasing envelope of the Raman active modes (Fig. 4.6b&c). This is a

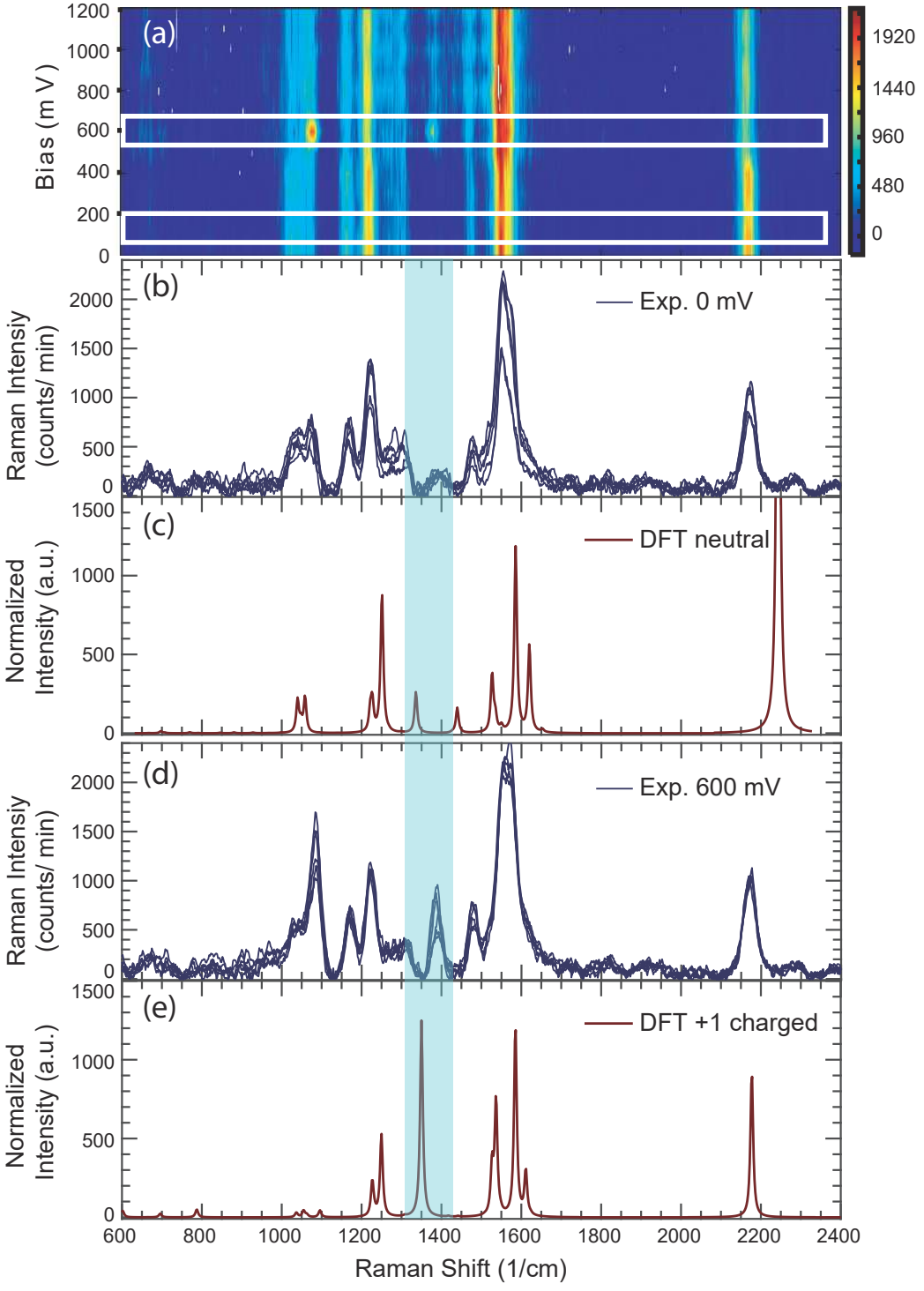

FIGURE 4.3: Single-molecule Raman spectroscopy. (a) Voltage-dependent Raman Stokes scattering from molecular junctions. Experimental Stokes Raman spectra at 0 V (b) and 0.6 V (d). Calculated Raman spectra of the neutral (c) and charged (e) states of BPA.

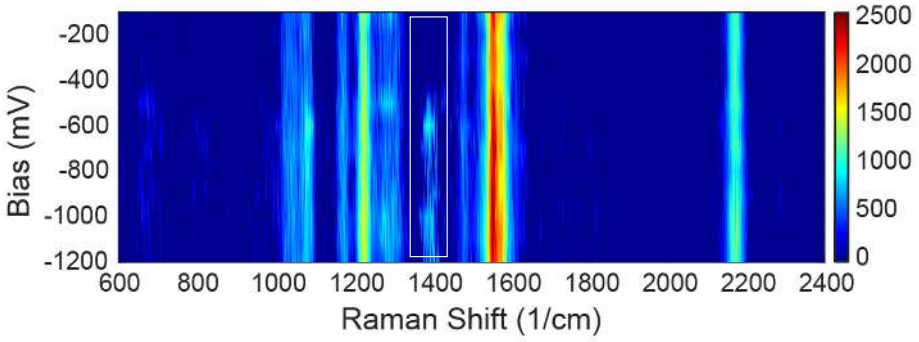

FIGURE 4.4: Stokes Raman spectra at negative biases.

strong indication that the distribution is not considerably affected by a non-equilibrium electronic temperature background [238]. We attribute our observations to phenomenon of charge-vibrational coupling and vibrational-vibrational dissipation in weakly-coupled junctions [239–241]. It follows that the detection of a steady-state, bias-independent, vibrational population during transient molecular charging enables the determination of single molecule charge-vibrational coupling [239–241].

4.1.3 Charge-Vibrational Coupling Through Rate Models

Rate models have been successfully employed [241] to accurately estimate a charge-vibrational coupling from a steady-state distribution, provided that the intramolecular vibrational-vibrational or the metal phonon bath-vibrational relaxation lifetimes are known. In a classical rate model, charge-vibrational coupled modes ν_i, having a vibrational occupation probability of $p_{\nu(i)}$, couple to the current I via the charge-vibrational constant λ. These modes are allowed to relax anharmonically to higher or lower energy modes ν_{i+n} or ν_{i-n} with a rate γ_{vib} and to metal phonon bath with a rate γ_{ph} (Fig. 4.7a). Using infrared (IR) time-resolved spectroscopy we measured an internal vibrational-vibrational relaxation time $\tau_{vib} = 1/\gamma_{vib}$ of 37 $\pm$ 4 ps (see Fig. 4.8). This number is in line with the finding that vibration-vibrational coupling constants are reduced for anthracene derivatives substituted symmetrically at the 9 and 10 position, as in BPA [242]. This time scale agrees with common estimates placing intramolecular relaxation redistribution times between 10 and 100 ps [243–245]. Steady-state iterative methods can be employed to find the two remaining variables γ_{ph} and λ, whereby we assume that only one of the lowest vibrational modes incurs charge-vibrational coupling. This is a valid assumption since low-energy modes have been shown to be responsible for charge-vibrational coupling in benzene [241, 246], fullerene [91, 247] and carbon nanotubes [230, 248]. For instance, the collective excitation of closely spaced modes at low biases strongly contributes to the prominent inelastic tunneling spectroscopy signal of oligo(phenyl-ethynylene) junctions [249]. With these considerations, N steady state linear equations are solved, one for the population of each of BPA's vibrational modes

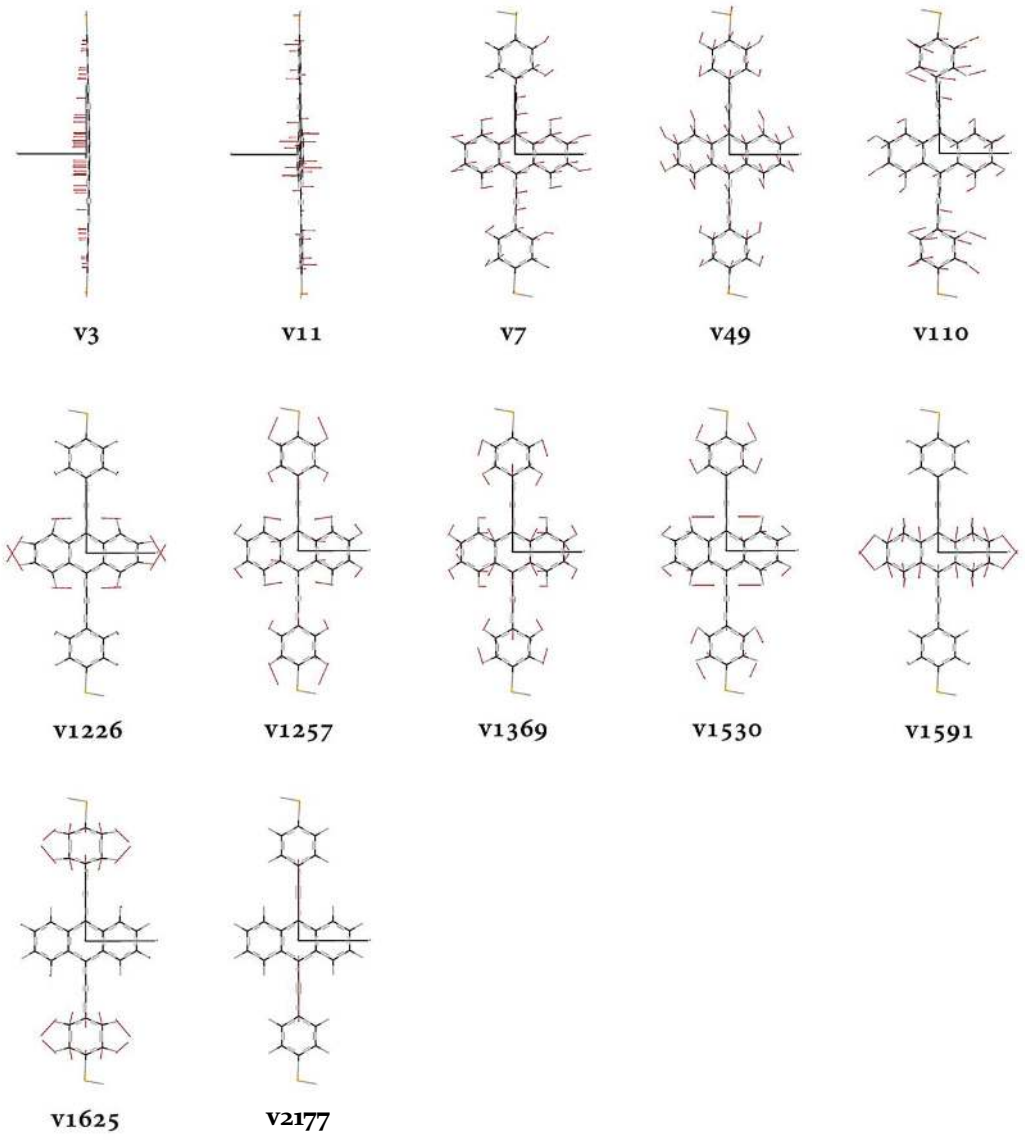

FIGURE 4.5: Vibrational modes of the cationic molecular model. The modes are labeled with the corresponding frequencies which are given in cm^{-1}. The modes v1226, v1257, v1369, v1530, v1591, v1625 and v2177 correspond to the peaks (Raman Shift) presented in Fig. 4.3e. Figure is adopted from [87].

coupling to its immediate neighbors (each mode's energy calculated from DFT). Solving the steady-state rate equations for the 4.11 cm^{-1} excitation mode and an inter-nal relaxation $\tau_{vib} = (37 \pm 4)$ ps yields a best fit to the experimental data of $\lambda = 0.58$, with a R-factor of 0.001 (Fig. 4.7b). The envelope for the vibrational population derived from the model is shown with a red line in Fig. 4.7b, together with the spectroscopic vibrational population (blue line).

As mentioned just above, γ_{vib} can be accessed by infrared pump-probe spectroscopy (see details in Appendix C). We emphasize that the time-dependent spectral dynamics, shown in Fig. 4.8a&b, provides direct information on the internal equilibration time

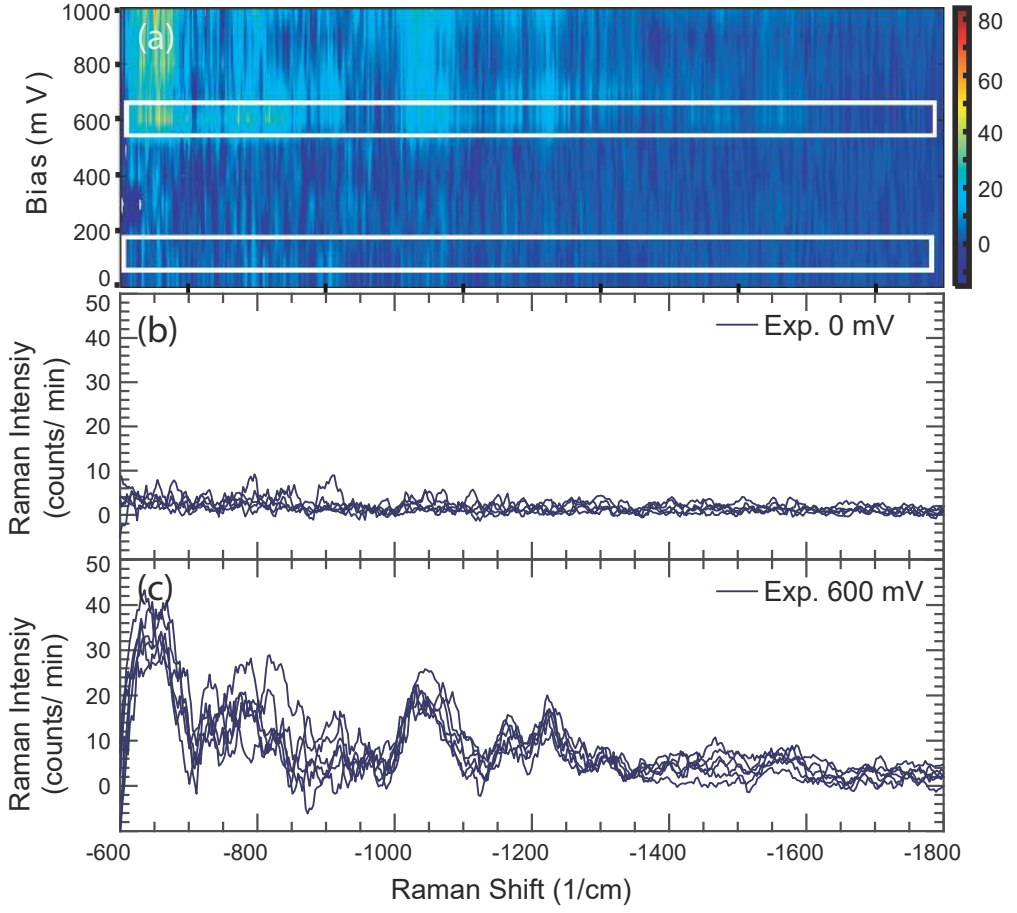

FIGURE 4.6: Voltage-dependent Raman anti-Stokes scattering. The white rectangles in (a) highlight two spectral regions above and below the resonance at 0.6 V (b, c). Anti-Stokes spectral region below 0.6 V (b) and at 0.6 V (c).

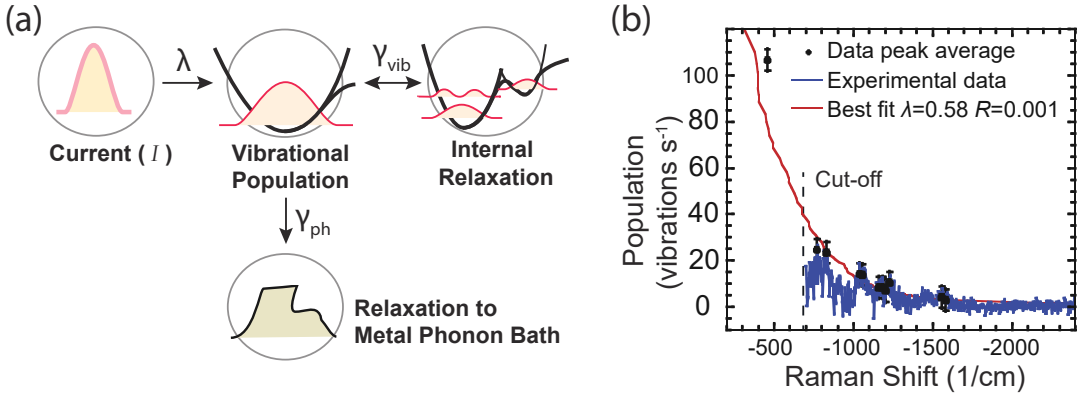

FIGURE 4.7: Charge-vibrational coupling through rate models. (a) A three-step rate model where the initial charge-vibrational coupling λ to a single mode ν_0 is in steady-state equilibrium with intramolecular relaxation through vibrational-vibrational rate γ_{vib} and with dissipation to the metal electrodes through a vibrational-phonon rate γ_{ph}. (b) The best fit to the anti-Stokes Raman intensity envelope showing R-factor with respect to experimental envelope.

(τ_{vib}) [250]. According to the non-equilibrium model [251] the strength of the electron-phonon coupling usually given by the second moment of the *Eliashberg* spectral function is:

$$\lambda \langle v^2 \rangle = \frac{k_B T_l}{3c^2 h \tau_{vib}}. \tag{4.1}$$

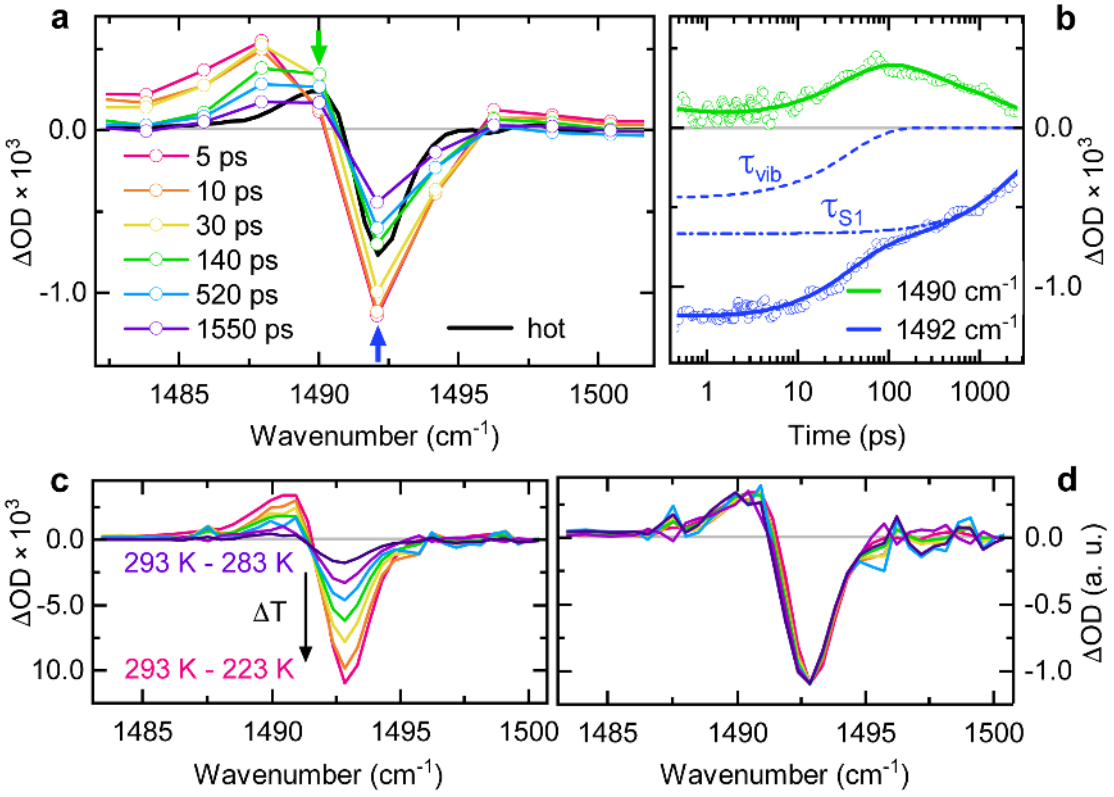

FIGURE 4.8: Vibrational relaxation of BPA in dichloromethane. Data are corrected by solvent background. a Time-resolved spectra for various delay times after excitation at 400 nm. The heating induced absorption change as in (d) is added to demonstrate that the system is in intramolecular equilibrium for longer delay times. The green arrow marks the shoulder developing with internal energy conver-sion. b Temporal evolution at the spectral positions marked by arrows in (a). Solid lines show a multiexponential fit. Dynamics are dominated by the vibration-vibrational relaxation time $\tau_{vib} = 37 \pm 4$ ps and the lifetime of the singlet excited state $\tau_{S1} \approx 3$ ns. c FTIR absorbance changes for various temperature differences in steps of 10 K. d Normalized spectra from (c) reveal that the spectral shape is independent of temperature.

Here $\langle v^2 \rangle$ is the square of the characteristic vibrational frequency and T_l is the inner-molecular lattice temperature. The latter is expected to be close to the solvent temperature, i.e. $T_l \approx 300\ K$ [251]. With a charge-vibrational coupling of $\lambda = 0.58$ this model yields a characteristic vibrational frequency of about 10.4 cm^{-1}. This very low characteristic frequency confirms our assumption that only one of the lowest vibrational modes governs the charge-vibrational coupling, dissipation and inference effects for specific molecular quantum vibronic states.

This work introduces a methodology granting access to the determination of transient molecular charge states and a method to estimate charge-vibrational coupling, by interrogating a molecule with molecular-scale Raman and I-V spectroscopy. The observed vibrational excitations are consistent with those predicted by theoretical treatments [239–241]. By generalizing the use of the MJS setup, we expect that identification and quantification of modes involved in charge transport, heat dissipation phenomena and energy loss mechanisms will become possible. These studies might help to determine charge-vibrational coupling, dissipation and inference effects for specific molecular quantum vibronic states.

April 11, 2018
Volume 140
Number 14
pubs.acs.org/JACS

JACS

JOURNAL OF THE AMERICAN CHEMICAL SOCIETY

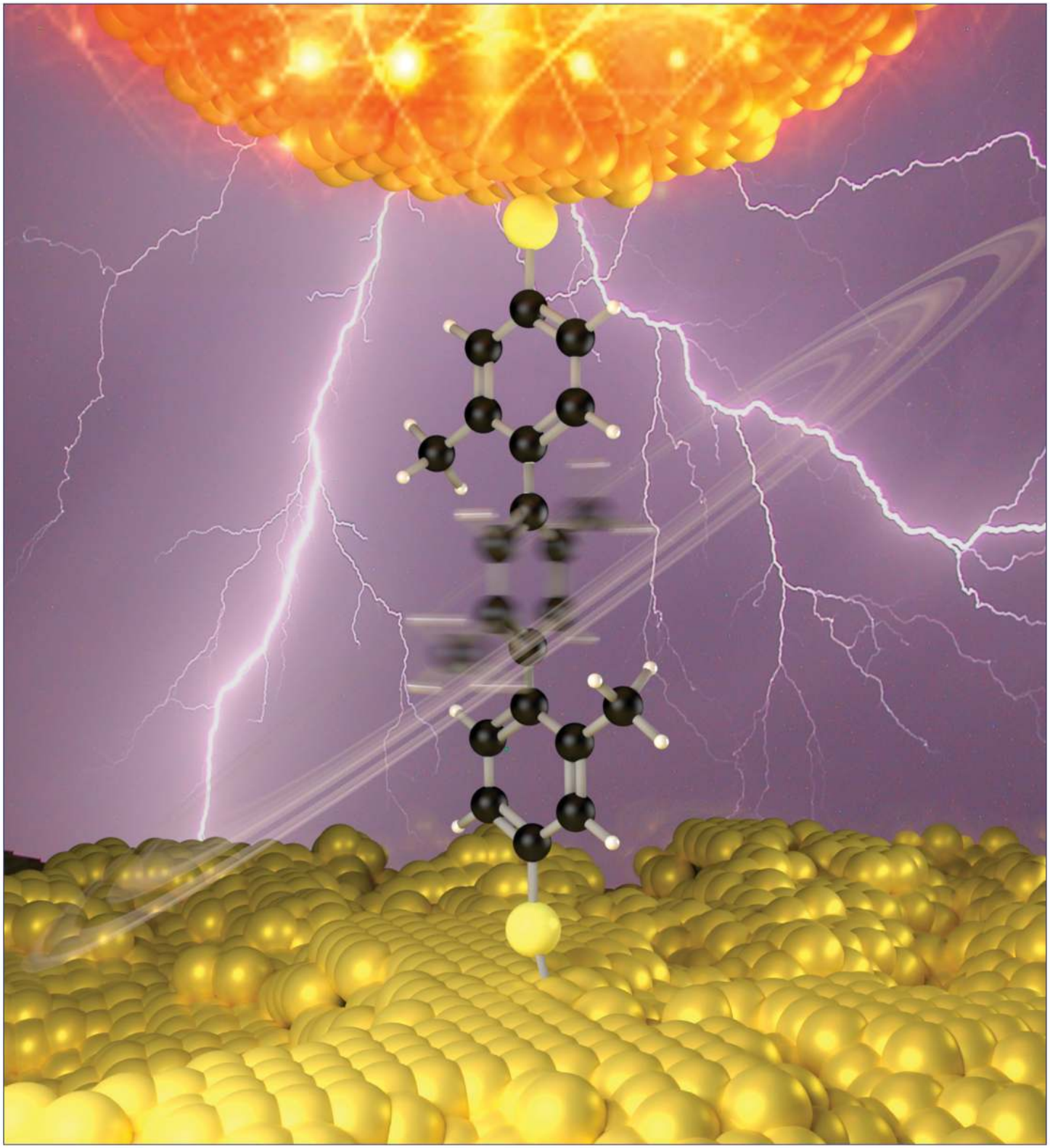

4.2 Voltage-Driven Conformational Switching with Distinct Raman Signature in a Single-Molecule Junction

Performing logic operations with molecules is a frontier in binary digital electronic computing [252, 253]. Many strategies have been proposed toward this goal based on bi- or multi-stable switching [254]. To accelerate progress in molecular-scale computing, both optical and electrical read-out and switching must be demonstrated with stable, controlled single-molecule addressing. In this project, we study on voltage-driven conformational switching in covalently linked metal-molecule-metal junctions of substituted oligoterphenyls, where control over switching and read-out is demonstrated by employing a tetragonal tip serving as an electrode and waveguide as illustrated in Fig. 4.9b. Exploiting Raman selection rules through physicochemical design, we show how voltage-driven conformational changes enable Raman intensity modulation by nearly two orders of magnitude. Specifically, we remove the ground-state polarizability and symmetry of a *p-terphenyl-4,4"-dithiol* (TPD) molecule (Fig. 4.9a right) by employing the *2,2',5',2"-tetramethylated* analogue (TPDT) [118, 255] (Fig. 4.9a left). With the highly sterically hindered, nonplanar TPDT, the Raman signature is strongly suppressed. At high applied biases, the junctions can be modeled as transiently oxidized, and thus, extended π-conjugation, polarizability, and Raman response are recovered (Fig. 4.9b).

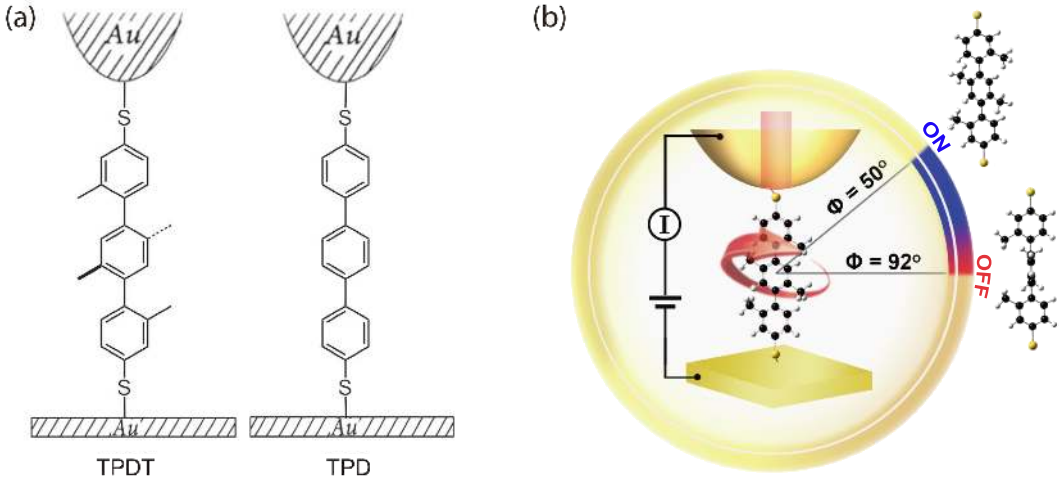

FIGURE 4.9: Illustration of the investigated systems. (a) Schematics of the TPDT (left) and TPD (right) molecular junctions; (b) Illustration of the voltage-driven single-molecule switch in a tip-molecule-substrate junction with Raman read-out by illuminating the molecule with a laser beam through the glass body of the tip to the apex.

In this section, the details of the experiments and the parameters used in the DFT simulation are initially declared. Then the charge-transport characteristics in single-molecule junctions are presented. The conformational change of the molecules caused

by the charge-transport are subsequently elaborated in terms of experiments and calculations. Finally, the hypothesis about the switching behavior is further verified with the cryogenic experimental results.

4.2.1 Experimental and Computational Details

Experimental Procedures. To establish a molecular junction, the sample is approached with a bias voltage of 0.5 V to the tip repeatedly until the current jumps out of tunneling, typically in the range of $1 - 100$ nA. Current-voltage characteristic curves between -1.5 V and 1.5 V are then obtained. When stable I-V curves are occurred, a single-molecule junction is supposed to be established, and the Raman spectra are recorded.

Density Functional Theory. The simulated Raman spectra were calculated with the *Gaussian 09W* package. The geometry of the isolated molecule was relaxed by optimizing the ground state energy with the pure PBE functional (keyword PBEPBE in Gaussian) using a 6-311G basis set. The basis set is automatically abridged at a reasonable angular momentum. Afterwards, the stationary-state geometry were used as an input for calculating the vibrational frequencies with the unrestricted PBEPBE/ 6-311G parameters. The calculation were performed in gas phase, neither current nor electric field are taken into account. The thiol groups are constraint to simulate the rigid bond situation between the electrodes and the molecule.

4.2.2 Charge-Transport Through Single-Molecule Junctions

Upon preparation of a layer of thiol-anchored TPDT on a thin film gold substrate, single molecules are contacted by the aperture-less, gold-coated, near-field tip. Fig. 4.10a shows typical I-V, dI/dV characteristics of TPDT. A I-d approach curve for TPDT at 0.1 V indicates a constant current of 5 nA through a single-molecule junction. In the selected regime of Fig. 4.10a, several junctions of TPDT display broad transport channels appearing at a bias voltage close to ±1.0 V. The ridgy features can be observed in the windows of $\pm[0.8,\ 1.3]$ V in the corresponding dI/dV curves. The current histogram of TPDT (Fig. 4.10b) suggests a conductance between 0.5 and 387 μG_0 during single-molecule junction formation at 0.5 V. To put the intriguing switching behavior of TPDT into perspective, we investigated the reference species TPD. Fig. 4.10d depicts the pertaining histogram along with extracted I-V and dI/dV curves (Fig. 4.10c) for TPD. This time, the contact entails transport resonances starting at 0.5 V. In both cases, the conduction band of the molecules increases when the featured bias voltage is surpassed.

At bias voltages close to or exceed the transport voltages, a clear Raman signal of TPDT is observed (Fig. 4.11a), featuring prominent peaks at approximately 650, 930, 1160,

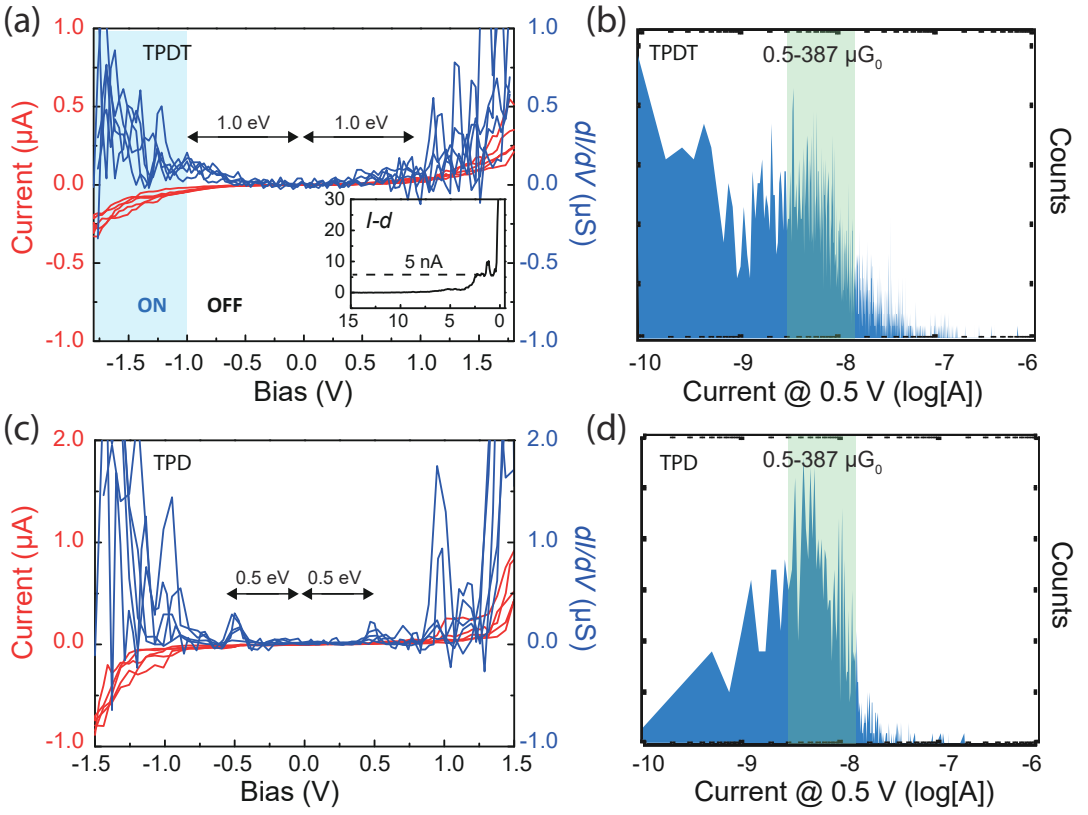

FIGURE 4.10: I-V characteristics of (a) TPDT and (c) TPD junctions. Current histogram curves, measured at 0.5 V while approaching a tip to a substrate covered with TPDT (b) and TPD (d). Figure is reproduced from [88].

1490, and 1580 cm^{-1}. By contrast, approximately 80% of the Raman signals recorded at 0.1 V fall below instrumental detection limits, i.e. the Raman signature is effectively suppressed (Fig. 4.11a). The observed voltage-driven switching can be repeatedly turned on and off at time scales limited by the junction stability only. In striking contrast to TPDT, the experimental Raman signature of TPD reproduced in Fig. 4.11b does not show any significant change at different junction voltages. Rather, the spectra display constant peaks near 1180, 1275, and 1590 cm^{-1}. Because both molecules are relatively apolar and neither linear nor quadratic shifts appear in the Raman spectra, the observed switching of the Raman signal of TPDT is clearly indicative of distinct and reversible conformational changes, whereby Stark or related electric field effects reported elsewhere can be excluded [67, 233, 234, 256].

4.2.3 Charge-Transport Induced Conformational Switch

Further evidence for a transient charging mechanism is provided by the DFT simulated Raman spectra analysis. First, experimental Raman spectra of TPDT (Fig. 4.12a&b) and TPD (Fig. 4.12e&f) are chosen from the molecular junction Raman survey in

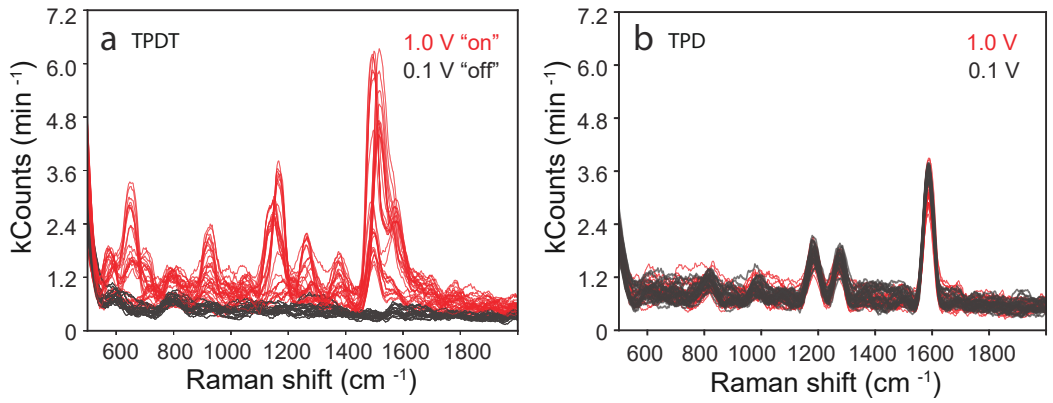

FIGURE 4.11: Raman signature of the pertinent junctions at biases of 1.0 and 0.1 V for TPDT (a) and TPD (b), respectively. Figure is adopted from [88].

Fig. 4.11. From various calculated oxidation states, the experimental Raman spectra of TPDT at 1.0 V fits best to the DFT simulated Raman spectra of positively charged (+1) species (Fig. 4.13). This suggests that charge (hole) transport in the molecule takes place through a (partially) depleted HOMO. Switching to a seemingly formal positively charged state could imply that electron depopulation is much faster than the electron repopulation. For the neutral state of TPDT, the Raman activity of the $\sim 1600\ cm^{-1}$ mode is 300-fold less than the computed charged species (Fig. 4.12e), in agreement with the experimental results.

The optimization of neutral TPDT at the PBE level of theory features the inter-phenyl torsion (IPT) angle of $\phi = 92°$ (Fig. 4.12c insert). Contrarily, the positively charged, singlet state of TPDT shows a geometrical stationary point with reduced IPT angles of $\phi = 50°$ (Fig. 4.12d insert). The Raman activity of a molecule is dictated by the internal product of the polarizability tensor with the overlap between initial and final phonon wave functions. Extended π-conjugation allows for higher molecular polarizabilities due to wave function delocalization and, consequently, increased Raman signals. Therefore, by decreasing the mode's polarizability, Raman activity can be turned "off" from an active "on" state. It is therefore expected that the Raman signature of TPDT decreases in its neutral form, where the π-conjugated character is at its lowest. The case is sensibly different for molecule TPD. As shown in Fig. 4.12g&h, the ground-state IPT of TPD (37°) is close to the oxidized form (25°). Thus, the Raman activity of TPD should remain similar between neutral and transiently charged, consistently with the experimental findings.

Transient charging effects [234, 257] are a well-known point of departure for the elucidation of bias-induced conformational effects. In oligophenylenes, the removal/addition of one electron increases the π-conjugation along the oligophenylene backbone due to the formation of quinoid or semi-quinoid resonance structures [258]. Such transient charging events occur during hopping transport or under a strong polarization regime [219]. In

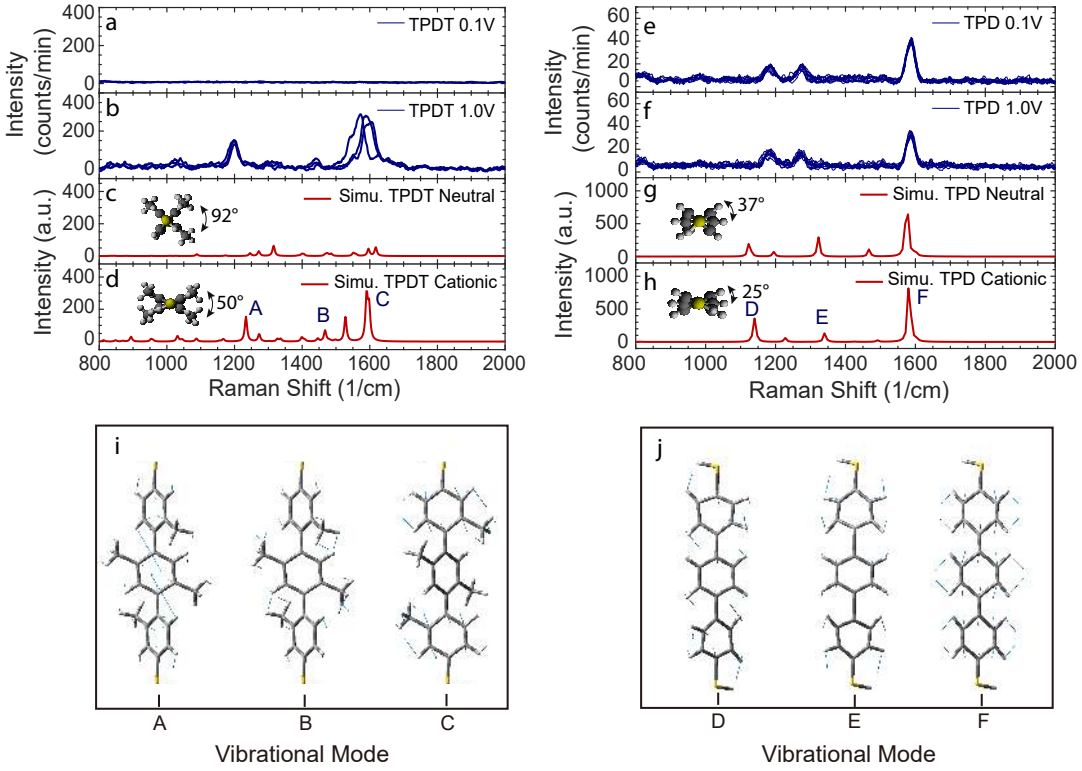

FIGURE 4.12: Experimental and computational Raman spectra of TPDT and TPD. Typical spectra of TPDT at 0.1 V (a) and 1.0 V (b). Neutral (c) and cationic (d) singlet state DFT Raman spectra of TPDT. Typical spectra of TPD at 0.1 V (e) and 1.0 V (f). Neutral (g) and cationic (h) singlet state DFT Raman spectra of TPD. (i) Vibrational modes of the prominent peaks (A- 'breathing' mode of phenyl rings, B- rocking of methyl groups, C- stretching of the upper and lower phenyl rings) of TPDT. (j) Vibrational modes of the prominent peaks (D- twisting of phenyl rings, E- intra-phenyl bond stretching, F- symmetrical stretching of phenyl rings) of TPD.

the semi-quinoid form, bond orders between phenyl rings amount to one and two, and the phenylenes' conformation is semi-coplanar. In the quinoid form, bond orders are close to two, and conformation is close to coplanar. Thus, oligophenylenes generally tend toward planar π-conjugation upon reduction or oxidation [259]. In this manner, a stationary point in the inter-phenyl torsion (IPT) potential energy surface (Fig. 4.14a, blue line) of an oligophenylene such as TPDT can be rationalized and further engineered through the interplay between the gradient of the attractive conjugation energy, which tends to planarize the structure, and the gradient of the steric repulsion. Thus, planarization is maximum for the oxidized form of TPDT , which is in agreement with its transient occurence during charge transport. Because of the large steric repulsion caused by the methyl substituents, the positively charged TPDT cannot adopt a fully planar quinoid structure. The increased π-conjugation in this case is geometrically manifested in π-twisted orbitals (Fig. 4.14b).

To investigate the role of π-conjugation in "switching on" the Raman activity, we performed DFT calculations of the cationic TPDT with different IPT angles (Fig. 4.15).

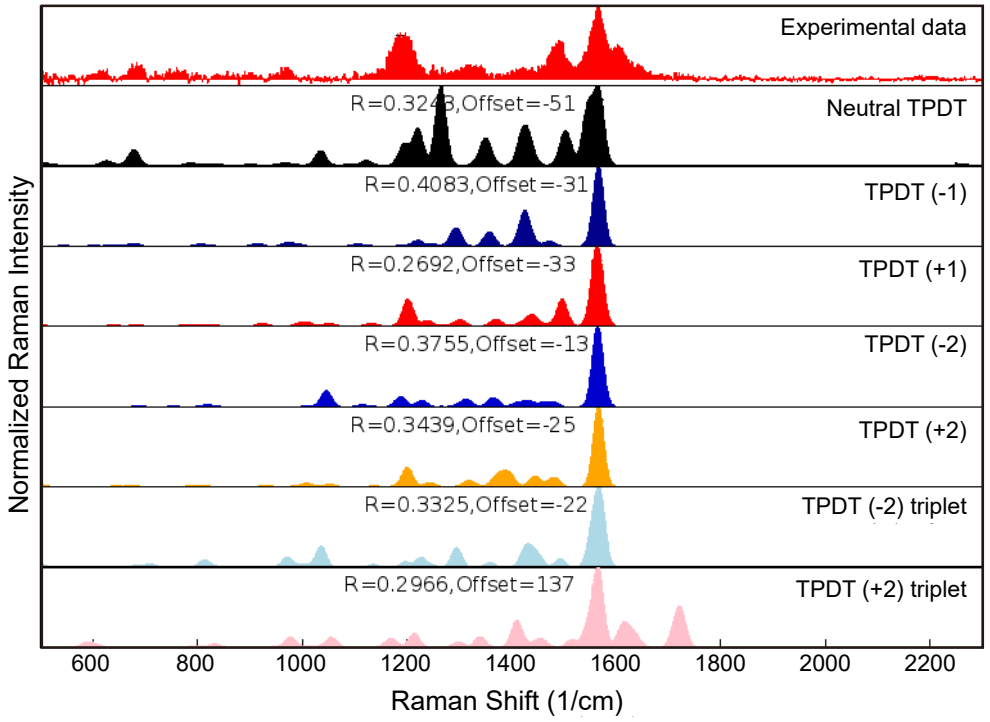

FIGURE 4.13: Correlation between DFT-simulated (PBE functional) Raman spectra of TPDT and the experimental data at a bias voltage of 1.0 V. Figure is adopted from [88].

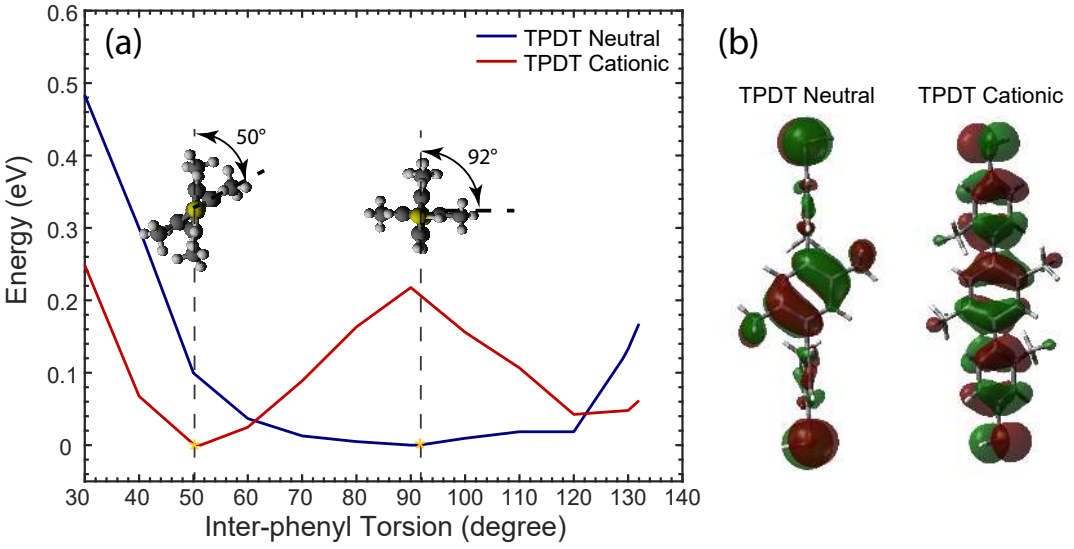

FIGURE 4.14: DFT total energy of TPDT at the neutrual and cationic states along the inter-phenyl torsion of the center ring (a) and the charge density at HOMO (b).

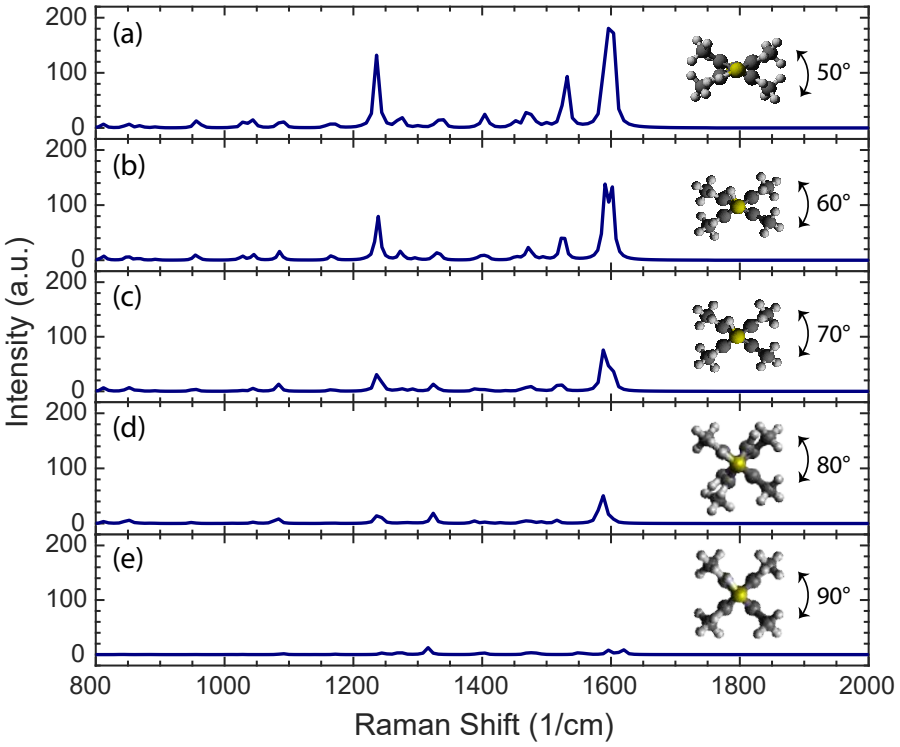

FIGURE 4.15: DFT Raman spectra in IPT of 50°(a), 60°(b), 70°(c), 80°(d) and 90°(e) for the cationic TPDT.

Spectra (a) and (e) were calculated from fully optimized molecular structures with fixed hydrogens at the sulfurs. We can find that the positions of the peaks almost stay unchanged with the alternation of the IPT angles. However the calculated Raman intensity decreases expeditiously with the increment of IPT. These observations and comparisons indicate that increased polarizability via extended π-conjugation is decisive for the switchable Raman activity of TPDT.

Conversely, the simulated Raman spectra of TPD (Fig. 4.12g&h) are not influenced significantly by its charge state. The ground-state IPT of TPD (37° Fig. 4.12g insert) is close to the oxidized form (25° Fig. 4.12h insert). Thus, the Raman activity of TPD should remain similar between neutral and transiently charged states, consistently with the experimental findings.

Finally, no anti-Stokes Raman signal was detected during HOMO charge transport for both TPD and TPDT molecules. One explanation for the absence of a significant anti-Stokes signal in the -2000 to -800 cm^{-1} region is the high resistance of TPDT and TPD. Lower currents imply that current-driven excitations of vibrational states are smaller and therefore below detection limits. The studies of TPDT and TPD thus demonstrate that a Raman on/ off switch is fundamentally accomplished by strongly increasing/ decreasing the polarizability of one state, since symmetry selection rules for both charged and neutral IPT geometries are similar.

4.2.4 Cryogenic Molecular Junction Raman Spectroscopy

From the analysis presented above, it follows that TPD should retain Raman activity independent of transient charging effects. The Raman spectrum of TPD also provides important insight into a freely rotating IPT barrier contributing to the Raman activity. DFT predicts similar IPT angles of 25° and 37° between the charged and neutral state of TPD. Attenuating room-temperature librations may allow bias-dependent detection between the small, but noticeable, differences in Raman activities predicted by DFT (Fig. 4.12g&h).

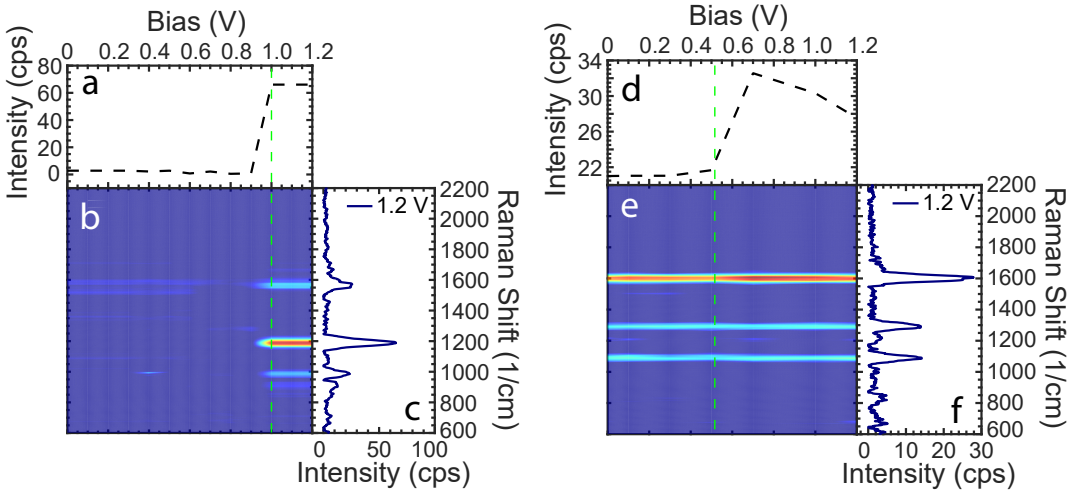

FIGURE 4.16: On/ off Raman behavior of TPDT and TDP at cryogenic condition ($T = 77K$). (a) 1200 1/cm peak intensity with respect to bias voltage; (b) Waterfall plot of Raman spectra along bias voltages; (c) Raman Spectra of TPDT at 1.2 V; (d) 1600 1/cm peak intensity with respect to bias voltage; (e) Waterfall plot of Raman spectra along bias voltages; (f) Raman Spectra of TPD at 1.2 V.

To substantiate this hypothesis, we performed cryogenic measurements at 77 K, whereby we also monitored the systems' response over the entire bias sweeps (Fig. 4.16). The corresponding data sets identify again a switching behavior of TPDT with a turn-on voltage at $\sim 1.0\ V$. For TPD, we detect a marked $\sim$ 1.5-fold increase in the $\sim 1600\ cm^{-1}$ Raman signal peaking beyond 0.5 V. This change is assigned to the different response of the neutral IPT 37° and transiently oxidized IPT 25° conformations at low temperatures. Evidently, the Raman signal of TPD cannot be turned off, because the unhindered ground-state IPT 37° remains polarizable (for comparison, the polarizable "on" state of TPDT is achieved at the theoretically predicted IPT of 50°).

We have shown conformational switching controlled by voltage in a single-molecule junction. Comparative low-temperature and theoretical studies served to experimentally identify alterations in the Raman spectrum with applied bias as polarizability switching driven by π-conjugation, which can be tailored by molecular design. The possibility of addressing physicochemical phenomena with single-molecule resolution shown here

serves as a departure point for a new generation of nanomechanical studies using MJS setups. Technologically, our investigations present single-molecule monitoring and manipulation with exquisite control, opening new avenues in multi-logic single-molecule computing.

This text has been published in [88].

4.3 Tension Induced Vibrational Frequency Shifts in Helicene Molecules

Helicene molecules, possessing a spring-like carbon backbone structure constructed by phenyl or other aromatic rings, exhibit a nonplanar structure due to the steric hindrance of the twisted phenyl ring connections. Benefiting from their intrinsic helical geometry, the π-conjugated backbone has an extraordinary deformation capacity [260–263]. Therefore, nanoelectromechanical systems are often investigated with helicenes [264–266]. Helicenes were proposed to be a potential spin filter due to their chirality which couples to the spin and linear momentum of the electrons, so that the molecule transmits one preferred spin [267–269]. Moreover, the electromagnetic field of light can induce a transport of polarized electrons along the helical backbone of the molecules [270–272]. Thus, the chiroptical properties of helicenes are widely studied, for example, circular dichroism [273, 274], non-linear optical response [275–277] and circularly polarized luminescence [278, 279]. Other promising applications include asymmetric catalysis [280], molecular switches [264], Langmuir–Blodgett films [281], etc.

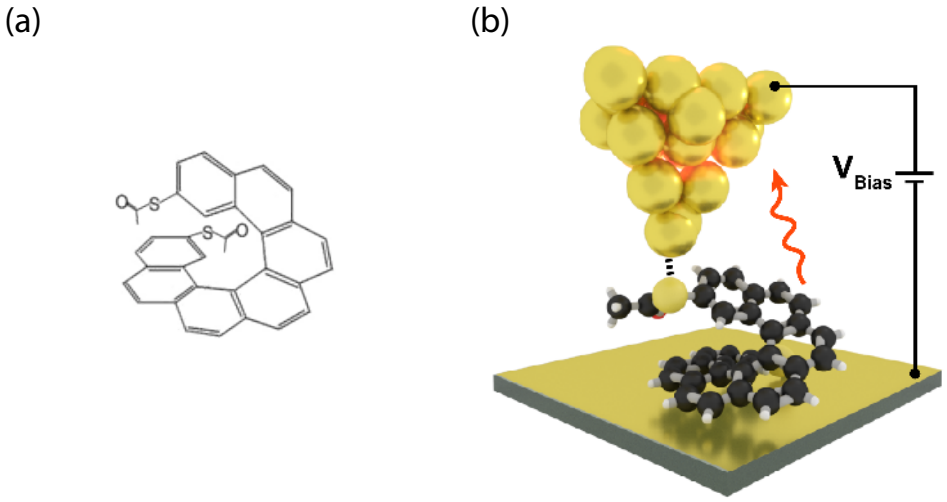

FIGURE 4.17: Molecular structure and junction schematic. (a) Chemical structure of the 7HdiET molecule; (b) Illustration of the single-molecule junction. The 7HdiET molecule is bonded in between the substrate and the gold covered glass tip. Raman signal is generated by focusing a laser beam through the glass body to the apex of the tip.

In this project, the electrical and optical properties of the *S,S'-Heptahelicene-2,17-diyl diethanethioate* (7HdiET) molecules [266, 282] (Fig. 4.17a) were studied by means of experiments and DFT simulations in single-molecule junctions. This molecule is choosing because it is the smallest helicenes with spring-like character. As illustrated in Fig. 4.17b, the central functional structure of the molecular junction is established by bonding a molecule to the electrodes in an electric circuit. By illuminating the junction with a

laser beam, the Raman signal of the molecule as well as the current through the junction can be simultaneously recorded.

In this section, the results are presented following the experimental produces as elaborated in section 3.3. First, the sample preparation details as well as the parameters used in the simulations are described. Then results of the statistically analyzed electrical characterization are presented. Thereafter, the obtained Raman spectra are compared with the DFT simulations of the isolated molecule and the molecular junction. In the end, tension-induced shifts in Raman spectra are discussed and explained in the context of DFT simulations.

4.3.1 Experimental and Computational Details

Substrate Preparation. The 7HdiET molecules were dissolved in THF, resulting in a solution with a concentration of 1 mM. A gold coated substrate was prepared as described in section 3.2 and immersed in 300 μL of 7HdiET solution. The immersed sample was heated up to 55 $^{\circ}C$ for 15 minutes and kept at room temperature for 24 hours to produce a Au-S anchored molecular layer on the substrate.

DFT Simulation. Initially, the ground state geometry of the isolated molecule was simulated with the *Gaussian 09W* package. The molecular structure of 7HdiET was optimized using a hyper-GGA functional (B3LYP) and a Pople (6-311G) basis set. Subsequently, the anchor ends (S atoms) of the relaxed structure were constrained to calculate the Raman spectrum using the same functional and basis set.

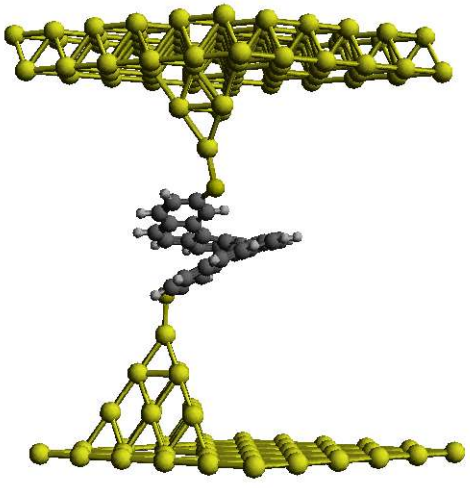

FIGURE 4.18: The 7HdiET junction model for DFT simulation consists of two Au layers on the top and one layer on the bottom. The tip and the rough surface are modeled in tetrahedral shape to contact the molecule.

In a more sophisticated model (Fig. 4.18), the electrodes are taken into consideration. The Au surface is included with 36 atoms in each Au layer. The molecule is contacted

by a tetrahedral tip and a rough surface with Au-S covalent bonds. The tip consists of two Au layers and a four-atom tetrahedron. One layer of gold and a larger tetrahedron is used for the substrate. The upper electrode was retracted with a stepsize of 0.2 Å with a total displacement of 4.6 Å to simulate the experimental conditions during pulling of the junction. After each displacement, the geometric structure was optimized, and the corresponding vibrational frequencies were calculated.

The geometric structure was relaxed with the *SIESTA* code. The Au atoms of the electrodes were fixed and the coordinates of the atoms in the molecule were optimized until the maximum atomic force reaches 0.02 eV/Å. The junction electronic structure was calculated using a $5 \times 5 \times 1$ Monkhorst–Pack k-point grid. Norm-conserving non-local Kleinman-Bylander type pseudopotentials were used. Exchange-correlation was described with the semi-local generalized gradient approximation(GGA) in the BLYP implementation. The local-orbital basis sets adopted from Vázquez [283–286] were used in the calculations. Au atoms were described with single-ξ polarized basis, while a double-ξ polarized basis was applied for C, S and H atoms. For the Au atoms of the surface layer and the tetrahedrons, a diffuse orbital basis was used to distinguish them from those in the bulk [287].

The vibrational frequencies were simulated based on the optimized structure with the *VIBRA* package. The exchange-correlation functional applied was PBE. Since only the phonons in Γ-point (i.e. center of the first Brillouin zone) can contribute to Raman signal, the supercell can be just the unit cell (i.e. k-point sampling is $1 \times 1 \times 1$) [206].

4.3.2 Statistical Conductance Characterization of Single-Molecule Junctions

The experimental procedures are elaborated in section 3.3. The first experimental approach to the molecules 7HdiET were repeated *I-d* measurements. Fig. 4.19a shows retraction *I-d* curves at a junction voltage of 0.1 V, whose tip-substrate distance were altered with a constant stepsize of 1 Å. A step-like feature appears in the current region of $10 - 15$ nA and extends for about 4.5 Å. The step indicates that a molecular junction has formed and can be stretched up to $\sim$ 4.5 Å until it is broken. In order to statistically determine the current through a molecular junction at a certain bias, thousands of *I-d* curves were analyzed by dividing them into nanoampere ranges and accumulating the counts in each range. This way, one can construct a current histogram which indicates a constant current by a pronounced peak. As shown in Fig. 4.19b, a current histogram constructed from 5000 *I-d* curves at 0.1 V presents a pronounced peak whose center is located at $\sim$ 10 nA.

When the bias voltage is gradually increased, the pronounced peaks in histograms move to higher currents as shown in Fig. 4.20. At negative bias voltage range, the peak

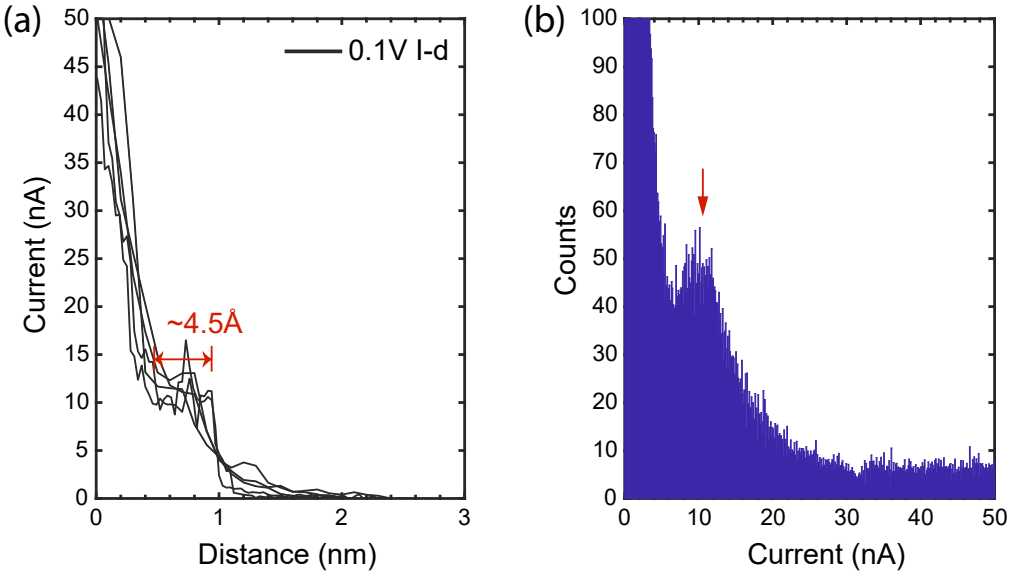

FIGURE 4.19: *I-d* measurements of 7HdiET at 0.1V. (a) *I-d* curves indicate a stable junction length of $\sim$ 4.5 Å at about 10 nA; (b) Histogram of *I-d* curves shows a peak whose center is located at ca. 10 nA.

shifts with the same tendency. It can also be noticed that, the width of the peak gets broader with increasing bias. This phenomenon indicates that, in a molecular junction, the current of the junction spreads more out from the average value with higher voltage. In practice, it is preferred to probe the repeatability and stability of the single-molecule junctions at a bias voltage $< 0.7\ V$. According to the acquired *I-d* data, the average probability of forming a molecular junction is about 3% for 7HdiET with our MJS device.

A pseudocolor plot in Fig. 4.21a combines the histograms at different bias voltages to reconstruct a *I-V* characteristics of 7HdiET. The bias voltages are taken as the abscissa and the corresponding counts of the current are displayed as "height". The insert depicts a component of the combined plot at 0.5 V. A step-like feature appears in the interval of 0.4 V to 0.5 V with about 50 nA which indicates that molecular orbitals are contributing to the charge transfer. A similar feature at the negative biases appears in between $-0.4\ V$ and $-0.3\ V$. The *I-V* characteristics is slightly asymmetric with higher conductivity at positive voltages where the current reaches 350 nA, while the current at negative biases reaches $-200\ nA$ at 1 V.

As the current of a single-molecule junction at a certain voltage has been determined, the bias voltage was set to 0.1 V and the current was manually kept in the range of $5-15\ nA$ to obtain a junction. When a sudden increase of the current occurs and stabilizes in a certain range, a metal-molecule-metal junction is supposed to have formed. From this moment, direct measurements of *I-V* characteristics were performed by sweeping the bias voltage from $-1.0\ V$ to 1.0 V in 200 equivalent steps. The current as a function of the voltage is presented in Fig. 4.21b (blue lines) and the corresponding differential

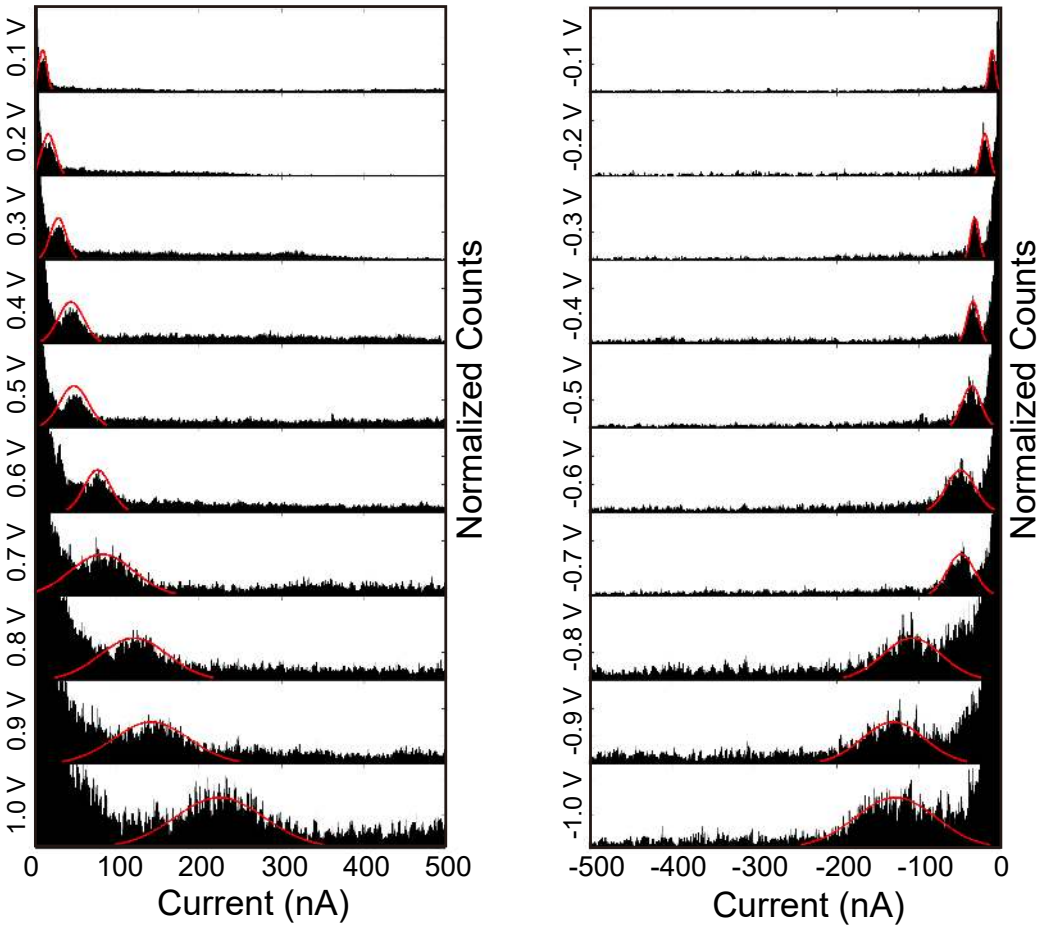

FIGURE 4.20: Histogram of *I-d* characteristics at different bias voltages. The red curves represent normal distribution of the molecular features.

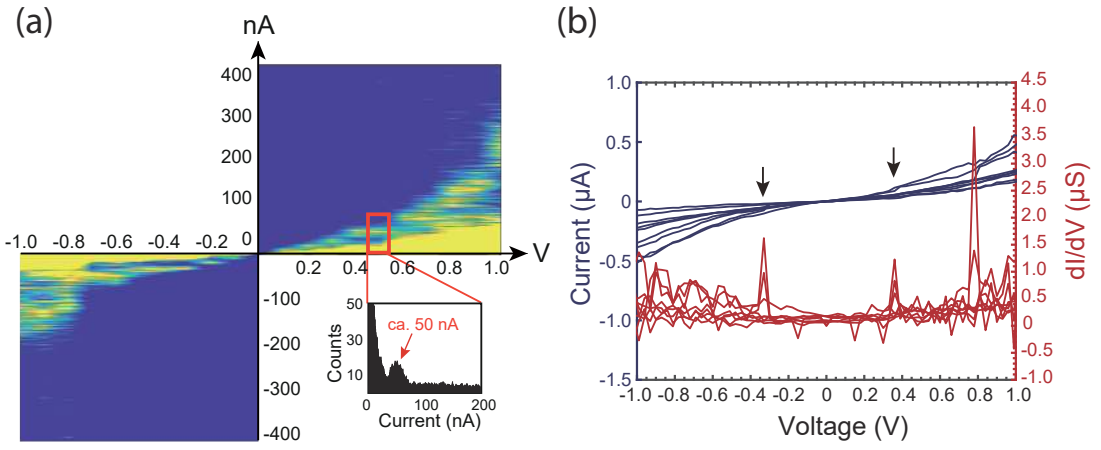

FIGURE 4.21: (a) Statistical reconstruction of a current-voltage characteristics. The insert indicates the *I-d* histogram at 0.5 V. (b) Direct *I-V* characteristics and the corresponding derivatives dI/dV.

conductance is calculated (red lines). The step-like features in the I-V curves located close to 0.4 V and -0.3 V appear as distinct peaks in the dI/dV curves, which fit well with the statistically reconstructed results demonstrated in Fig. 4.20 & 4.21a. We note that the current has strong variations when the bias voltage is above 0.4 V. This is a typical behavior in single molecule experiments, considering that the atomistic structure of the Au-S contact is different from junction to junction and the current is not averaged by many molecules.

4.3.3 Molecular Junction Raman Spectroscopy

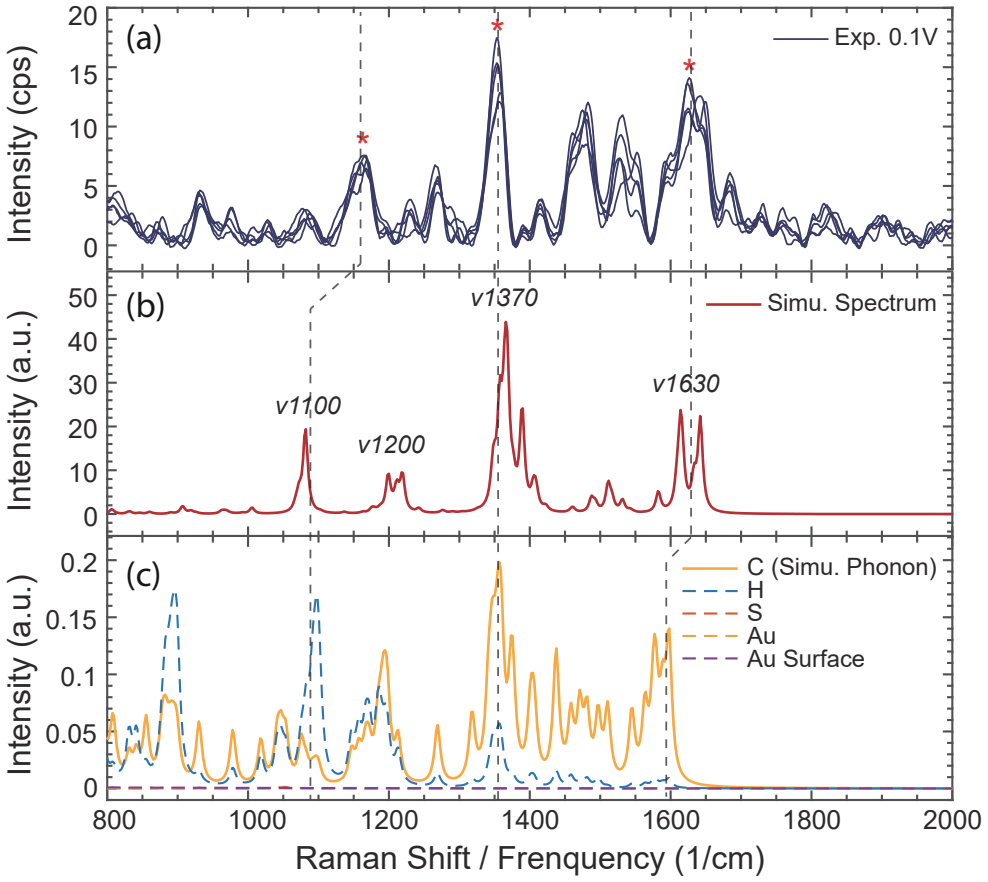

FIGURE 4.22: Experimental and computational vibrational frequencies. (a) Experimental Raman spectra at 0.1 V. The highly reproducible peaks in the measurements are marked with stars; (b) DFT simulated Raman spectrum, the annotated peaks whose vibrational modes are illustrated in Fig. 4.23; (c) Simulated vibrational frequencies.

Fig. 4.22a shows typical Stokes Raman spectra of 7HdiET measured at a bias voltage of 0.1 V. The peaks, marked by stars, at approximately 1170, 1370 and 1620 cm^{-1} exhibited a high reproducibility during the measurements. The peak at $\sim$ 900 cm^{-1} is the signal from the glass which served as the base material of the tip and the substrate [288] which are always present in the Raman spectra. Fig. 4.22b presents the Raman

spectrum of an isolated molecule from DFT simulation whose dominant peaks fit overall well with the experimental ones. Due to the various junction conformations and bonding configurations, the peaks appear at $\sim 1300\ cm^{-1}$ and in the range of $1500 - 1600\ cm^{-1}$ in the experiments are rather mutable. This is typical for single-molecule vibrations [289–291]. Furthermore, the vibrational frequencies of each element in a molecular junction were calculated as depicted in Fig. 4.22c. The symmetric charge distributions of bonds (e.g. C-C, C=C) will have large effects on the polarizability during a vibration and will be highly Raman active. Thus, the vibrational frequencies of those atoms mainly contribute to the Raman signal. For 7HdiET, the prominent peaks of carbon in the vibrational spectrum at around 1200, 1370 and 1600 cm^{-1} match well with those prominent peaks in the experimental spectra.

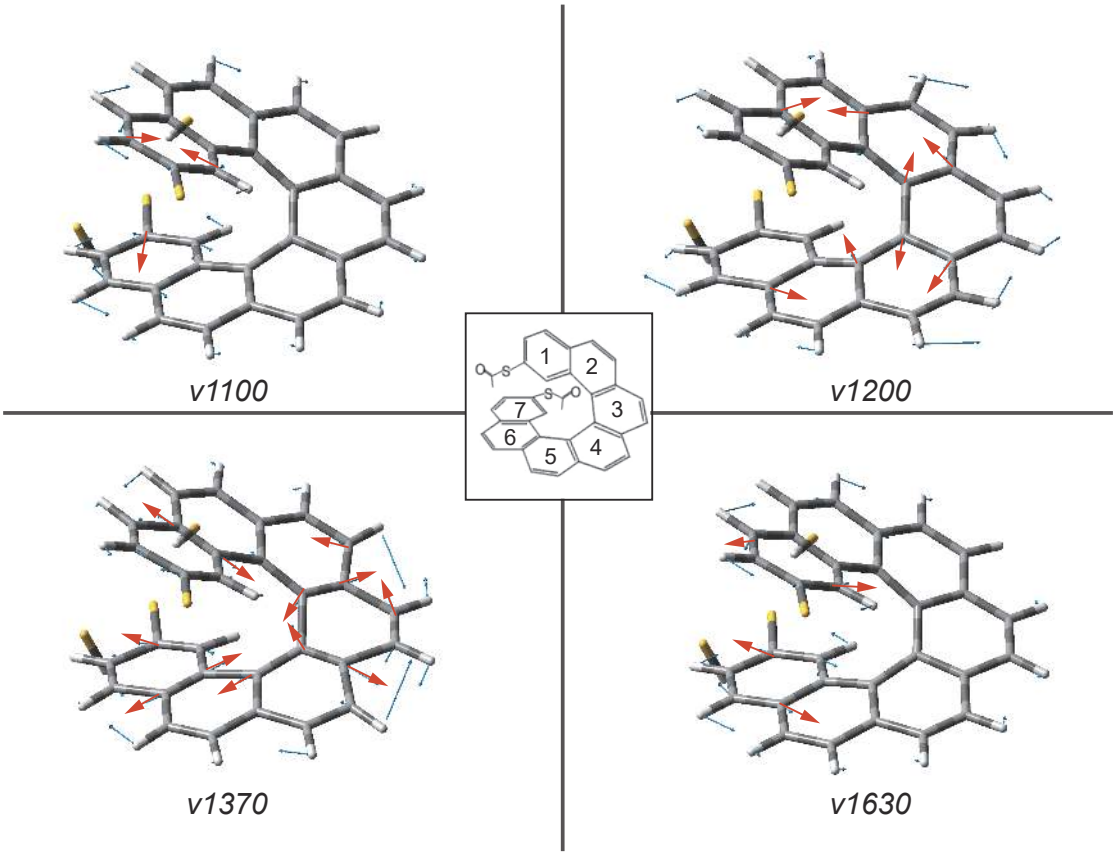

FIGURE 4.23: Vibrational modes of 7HdiET corresponding to the prominent peaks in the simulated Raman spectra (Fig. 4.22b). The red arrows indicate the drastic asymmetric stretching motions of the C-C & C=C bonds which distort the phenyl rings in the ring planes, and the blue arrows show the C-H rocking vibrations. For *v1100* and *v1630*, carbons in 1 &7-phenyl rings contribute to the vibrations, the 2,3,5,6-phenyl rings contribute to the vibration *v1200* and all of the phenyl rings involve in the vibration *v1370*.

Moreover, the vibrational modes of the prominent peaks in the simulated Raman spectra (Fig. 4.22b) are illustrated in Fig. 4.23. The mode at 1370 cm^{-1} is predicted by DFT simulations to shift with molecular strain (see Section 4.3.4). Furthermore, in practice,

the 1370 cm^{-1} peak is the most stable signal observed. Therefore, we focus on the analysis of this characteristic peak for further studies.

4.3.4 Strain Induced Shifts in the Vibrational Frequencies

Strain can be applied to the molecular junction by increasing the tip-substrate distance. In experiments, this was performed by retracting the substrate from the tip with a stepsize of 0.26 Å (the minimum stepsize of the piezo). After each displacement of the substrate, a Raman spectrum with an exposure time of 10 s was acquired. These procedures were executed by a newly developed automatic program which is introduced in Appendix A.

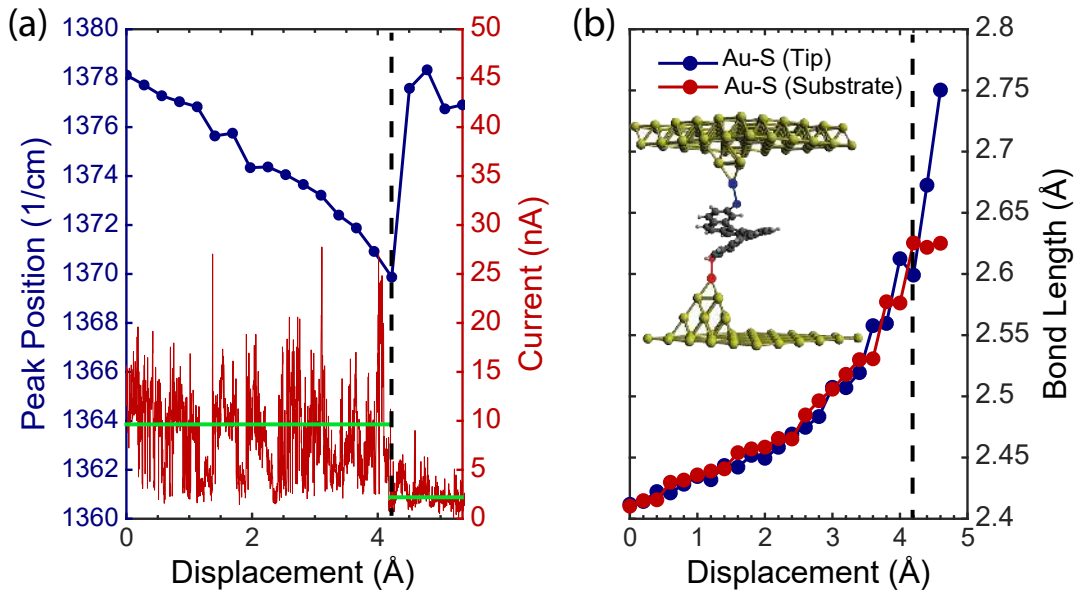

FIGURE 4.24: The analysis of helicene stretching experiment. (a) Peak position of the 1370 cm^{-1} peak in dependence of the sample displacement with the simultaneously recorded current at 0.1 V; (b) Simulated Au-S bond lengths.

The characteristic peak at 1370 cm^{-1} was chosen to investigate the correlation between the electrode displacement and the Raman shifts for its high reproducibility and analyzed regarding its peak position as described in section 4.3.3. As shown in Fig. 4.24a, the peak position (blue line) shows a decreasing tendency of the Raman shift with respect to the displacement. The current in the junction (red line) at a bias of 0.1 V initially fluctuates around 10 nA during the pulling procedure, in agreement with the statistical results. When the displacement of the substrate reaches 4.2 Å, the current drops to about 2 nA immediately. During this process, the Raman peak shifts about 8 cm^{-1}, and jumps back to its initial position subsequently. We presume that junction is broken at this point and the maximum stretch distance for this molecular junction is ca. 4.2 Å. A rupture force of about 1.5 nN for the Au-Au bond is commonly assumed [292–294]. Studies have shown that, the breakdown of the alkanethiol junction most likely occurs

at the Au-Au bond [295, 296]. For the 7HdiET molecule, a donor-acceptor Au-S bond [297, 298] is supposed to be formed between the molecule and gold electrodes, which can bear a force up to 0.9 nN [299]. Therefore, the donor-acceptor Au-S bond is more likely to be ruptured when the molecular junction is broken in our experiments.

In simulations, the z coordinates of the gold atoms of the tip were increased by 0.2 Å/step and the geometry of the molecular junction was subsequently relaxed. Afterwards, the vibrational frequencies of the elements in the optimized structure were calculated. The Au-S bonds length to the tip and substrate were analyzed as illustrated in Fig. 4.24b. The Au-S bond lengths at both sides increases nonlinearly with the change of the tip-substrate distance. When the displacement exceeds 4.2 Å, the Au-S bond on the tip side (blue) increases drastically and the one on the substrate side (red) keeps constant. This asymmetric behavior could indicate that the Au-S bonds are about to rupture with the maximum bond length of about 2.6 Å. The experimental and simulated results fit well with each other and indicate that Au-7HdiET-Au junction could be broken at a stretching distance of about 4.2 Å.

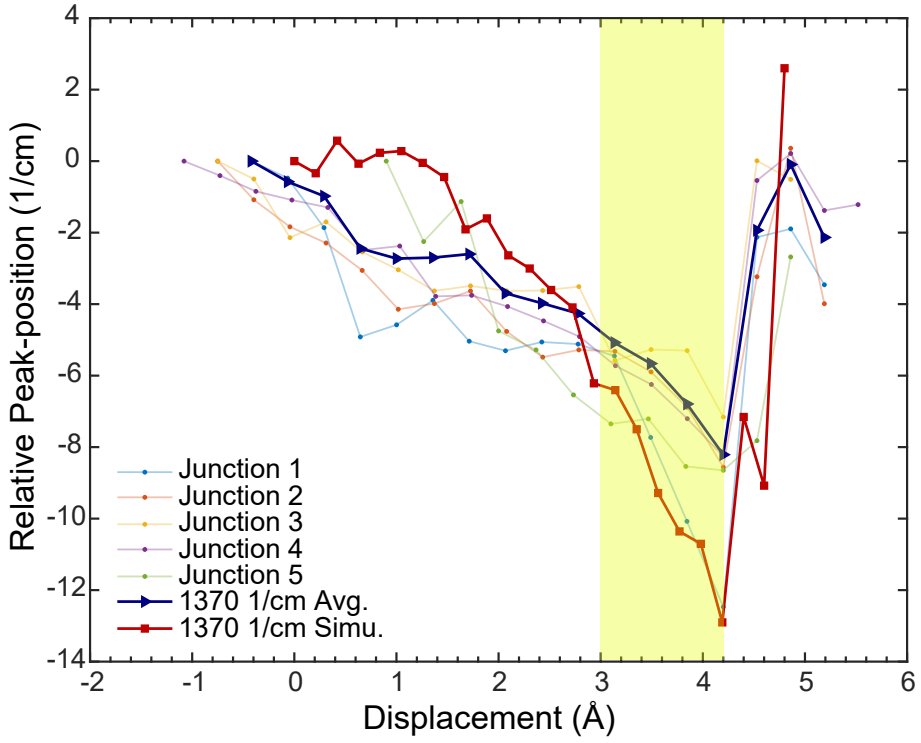

FIGURE 4.25: The experimental and computational shift tendencies of the characteristic peak (1370 cm^{-1}) while pulling the junction. The experiments were performed at a bias voltage of 0.1 V.

Fig. 4.25 depicts the relative peak position with respect to the tip-substrate displacement of five different junctions at a bias voltage of 0.1 V. The averaged value of the peak position shifts with the displacements is presented as the blue line. The simulated relative mode frequencies of the characteristic peak as a function of displacement is

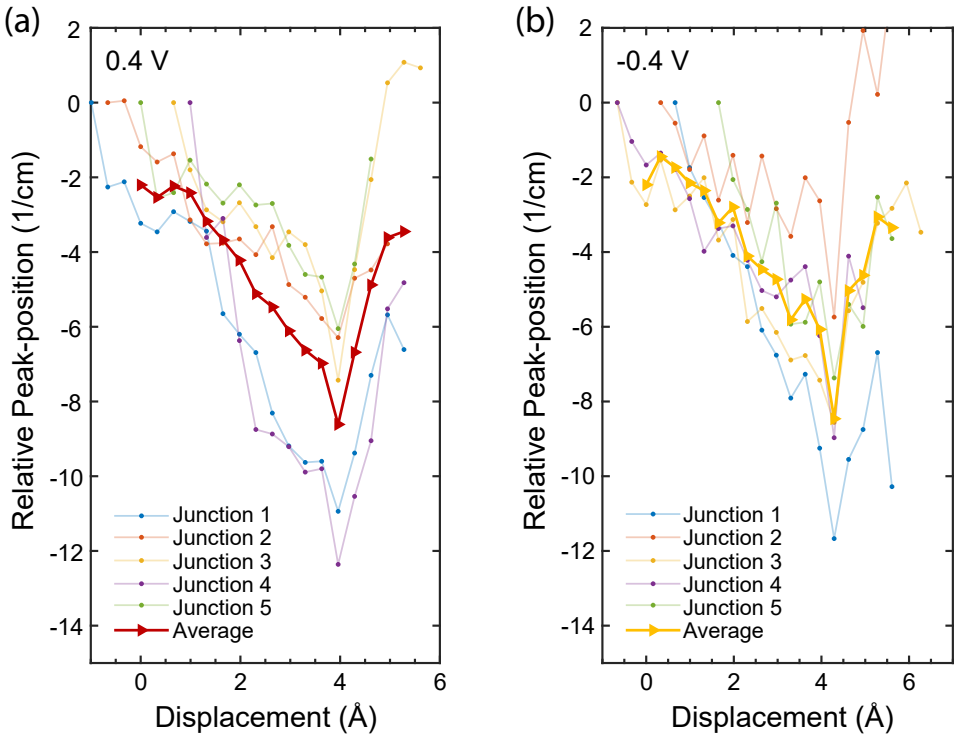

FIGURE 4.26: The experimental shift tendencies at (a) 0.4 V and (b) -0.4 V of the characteristic peak.

depicted as the red line. Since the initial situation while forming a junction is not necessarily identical in practice, the breaking points in the experimental and simulated curves were fixed at the same displacement to better compare the results. Both results show similar tendencies as well as a rapid recovery after the breaking point and have a similar maximal stretching lengths of $\sim$ 4.2 Å. Previous studies have shown that vibrations involving carbon-carbon bonds are stress sensitive and the corresponding bands tend to shift to lower frequencies [300–302] which agrees well with our results. It is noteworthy that the slope of the simulated curve after 3 Å is larger than that of the experimental curve. It shows a peak shift up to 13 cm^{-1} while the peak shift for the averaged experimental results is only 8 cm^{-1}. According to literatures [295, 299], structural rearrangements within the Au electrodes could happen during the stretching of the molecule, which could compensate the tension in the molecular junction. However, in the simulations, the softness of the gold electrodes was not taken into consideration, which might be responsible for the mismatch in the slope of the shifts. In addition, other relatively reproducible peaks at approximately 1200 cm^{-1} and 1600 cm^{-1} have been analyzed both in experiments and simulations but did not exhibit any significant shifts.

Further stretching-dependent vibrational investigations were performed at biases of ± 0.4 V, where the step-like features appear in the I-V characteristics (Fig. 4.21). Each averaged line is obtained from five independent junctions as depicted in Fig. 4.26. The

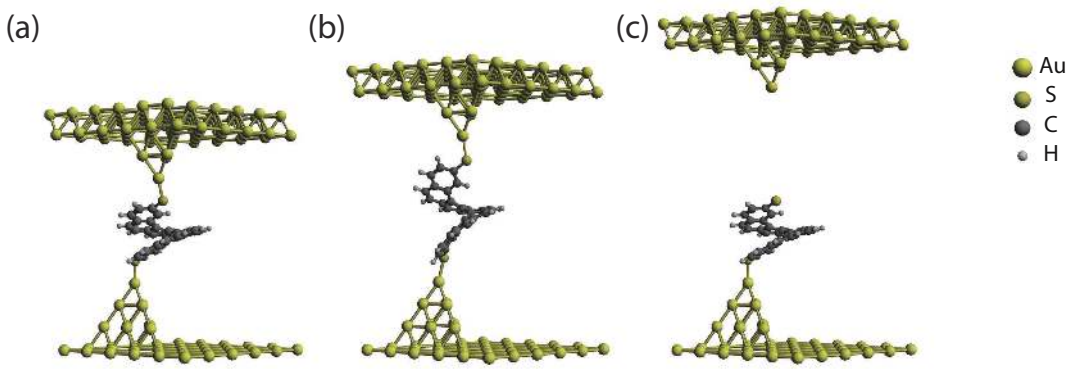

FIGURE 4.27: Schematic of the stretching and rupture process in a single-molecule junction.

shift tendencies at 0.4 V and -0.4 V present similar rupture lengths as well as relative frequency shifts compare to these at 0.1 V.

The pulling procedure of the junction is illustrated in Fig. 4.27. Initially, the 7HdiET molecule is bonded in between the gold electrodes to form a junction (Fig. 4.27a). Subsequently, with the increasing tip-substrate distance, the molecule is stretched which gives rise to the frequency shifts of a certain vibrational mode (1370 cm^{-1}), as illustrated in Fig. 4.27b. When the displacement reaches a threshold ($\sim$ 4.2 Å), the Au-S bond can not sustain the tension and the junction breaks, as shown in Fig. 4.27c.

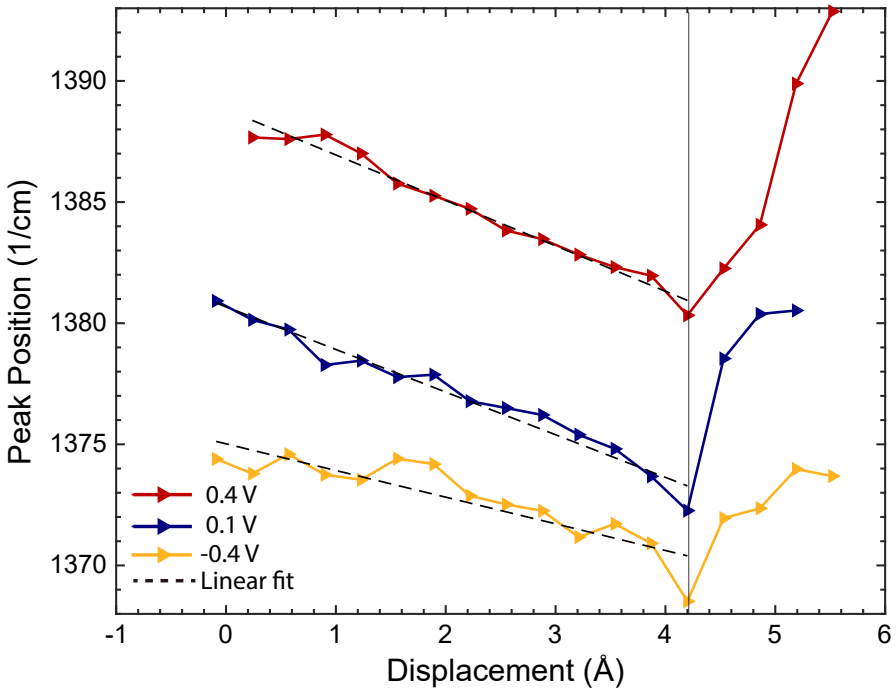

FIGURE 4.28: The tendencies of the characteristic peak at -0.4 V, 0.1 V and 0.4 V respectively.

Within this context we wanted to investigate how an applied bias voltage affects the Raman frequency shifts. Fig. 4.28 displays the vibrational shift tendencies in dependence of the substrate displacement of the characteristic peak at $-0.4\ V$, $0.1\ V$ and $0.4\ V$, respectively. The average tendencies are aligned to have the same rupture point. It is worth mentioning that the vibrational frequency of the characteristic peak alters with the bias voltage. According to the research of Stetsovych *et al.* [266], with the same molecule (7HdiET) as in this study, helicene molecules on surfaces show a converse piezoelectric effect. That is, the bias voltage could induce deformations of the molecule. The charge transfer between the molecule and the electrodes induces an electric dipole moment along the helix axis in the molecule, which in turn results in a piezoelectric effect. Therefore, when a positive bias voltage crosses the electronic barrier is applied, the molecule is pre-compressed which shifts the vibration to higher frequencies. In our case, the wavenumber of the characteristic peak decreases from a start position of 1389 cm^{-1} to 1381 cm^{-1} and keeps above the neutral state along the pulling process. Contrarily, a negative bias would pre-stretch the molecule and shifts to lower vibrational frequencies.

It has been reported that bias-driven charging can be responsible for vibrational shifts in single-molecule junctions [233, 234]. In this case as well as for a symmetric junction geometry as described above, the vibrational shifts at negative and positive biases should be identical, which is contradictory to our results. The presence of pertaining dipole moment or structural asymmetries within the junction are expected to contribute to the asymmetric shift with the bias voltage. Thus, further simulations are necessary to disentangle structural and electronic asymmetries and are under way by our collaborators [283–286].

We can conclude that the 7HdiET molecules show a linear shift tendency when strain is applied to the molecular junction. The junction can be stretched up to 4.2 Å where the Au-S is ruptured. A strong converse piezoelectric effect is observed when higher bias voltages are applied. These properties indicate that surfaces functionalized with 7HdiET molecules have the potential to be applied in touch sensitive devices, as described in [303].

Chapter 5

Summary

The major objective of this thesis entitled *Single-Molecule Junction Spectroscopy and Computational Modeling for Molecular Electronics* is to investigate the electrical and optical characteristics of single-molecule junctions and compare it to stimulations. A self-built molecular junction spectroscopy set-up is used to perform the experiments. DFT simulations with *Gaussian 09W* and *SIESTA* packages serve to predict the conformations and vibrational frequencies of the molecular junctions.

The ability to record single molecule charge-vibrational coupling, grants access to the determination of charge transport efficiencies for specific molecular configurations and currents. The charge-vibrational coupling for a current-carrying chemically well-defined molecule was studied by synchronous vibrational and metal-molecule-metal junction current-voltage spectroscopy. By measuring the steady-state vibrational distribution during charge transport in the BPA molecules by anti-Stokes Raman scattering, we find an electron-phonon coupling of 0.58 vibrational excitations per charge carrier.

For the molecular switch study, the TPDT and TPD molecules were employed. The *I-V* characteristics and Stokes Raman spectra were recorded and typical results were compared with DFT simulations. The Raman activity at low bias voltages is below the detection range of the device, whereas a clear Raman spectrum appears at higher voltage. This phenomenon can be explained by comparing experimental and computational results. The optimized structure of TPDT shows a remarkable alternation of the IPT within the molecule when being charged. This conformational change in the molecule, which goes along with a charge redistribution of the π-electron system allows

us to propose a prototype of a conformational switch to describe the conductance behavior of TPDT. As a comparison, the ground state of TPD remains polarizable at every voltage, hence no switching behavior is found.

The single-molecule junction can be established by approaching the substrate to a gold covered tetrahedral near field tip. The 7HdiET molecules were used to study the tension related vibrational properties. The statistical reconstructed current-voltage characteristics are investigated to determine the current through a molecular junction. After junction formation, the substrate is carefully retracted, stretching the molecule. At each step, a Raman spectrum is acquired. One distinct vibrational mode is systematically analyzed, and reveals a systematic redshift corresponding to the applied strain in the single-molecule junction. The investigations at different bias voltages might indicate strong converse piezoelectric effect.

Appendix A

LabVIEW Program

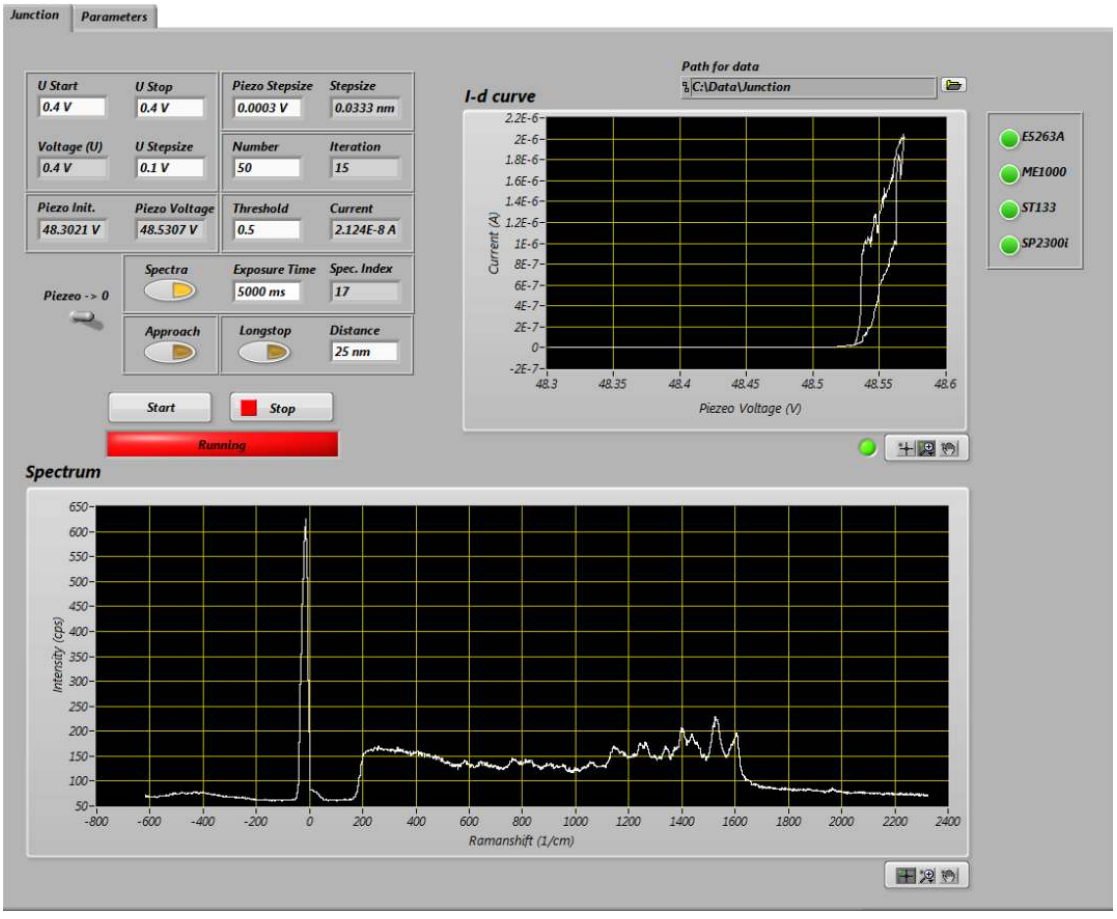

Figure A.1: The automated LabVIEW program which enables the synchronous investigation of I-d curves and Raman spectra.

In this appendix, a newly developed LabVIEW program is introduced. Fig. A.1 is the screenshot of the user interface panel. It is a software dependent program, meaning that it can only be executed with the Natioanal Instruments LabVIEW (2017) software. There are two tabs in this program, the *Junction* and the *Parameters* panels. The latter includes the default parameters, such as the laser wavelength and the saving path, will not be elaborated. The *Junction* tab contains the parameters setting part, the I-d curve display panel, the spectrum display panel and the hardware status indicator (rightmost).

The program enables the automated study of the distance dependent vibrational properties of the molecule as well as the statistic achievement of *I-d* characteristics. Each loop contains an approaching and a retracting process. The initial piezo voltage is adopted from the value after the automatic approach (section 3.3) and sequentially increases with a certain stepsize. When the current reaches an assigned threshold, the piezo is retraced by reducing the voltage with the same stepsize till the noise level or a certain assigned distance (when the *Longstop* button is switched on) is reached. When acquiring Raman spectra simultaneously, the *Spectra* button is switched on and an exposure time is assigned. One spectrum is recored after each displacement of the piezo. On the other hand, the *I-d* curves can be recorded independently by switching the *Spectra* button off. Additionally, by switching the *Approach* button on or off, one can decide whether to record the Raman spectra during the approach process or not.

The start voltage (*U Start*), stop voltage (*U Stop*), voltage stepsize (*U Stepsize*) and number of loops (*Number*) can be set to perform the measurements circularly at different bias voltages. When it starts, a folder named as the current date in the format of "yyyymmdd" is automatically created in the appointed path. If more than one tasks are performed in a day, the folder name is created with an appended number (e.g. 20180101_3) to the date. The bias voltages are created as sub-folders in the date folder, in which the I-d curves are organized in a folder named as *Id*, and the spectra in each loop are saved into a folder named with the count number of the loop. In this way, the data analysis can be performed systematically by programming.

In addition, the switch $Piezo -> 0$ can be triggered on to retract the substrate from the tip after the entire procedure in order to prevent the tip from crashing on the substrate due to ambient vibration or drift of the piezo.

Appendix B

Data Analysis Software

A self-developed software is introduced in this appendix. The software is an executable program (.exe) for Microsoft Windows system which is developed with MATLAB. The software contains three tabs which enable spectra processing according to the date, *I-d* and *I-V* characteristics checkup as well as peak analysis respectively.

B.1 Spectra Viewer

Fig. B.1 is the user-interface of the spectra viewer panel. The function of this panel is to visualize the Raman spectra and simultaneously substrate the baselines of them. First of all, the folder which contains the spectra data should be selected by click the *PATH* button in the **Database Path** module. The filename of a spectrum is created according to the data type, acquired date and time, exposure time and bias voltage (e.g. 'SP 18.12.31 12.30.05 Uhr 1000ms 0.100V.dat').

When the path is assigned, all of the files whose name start with 'SP' are collected and their date information are extracted. Then by clicking the *DATE* button in the **Choose Date** module, a pop-up calender (Fig. B.2) appears. According to the date information, the date which has at least one spectrum is is marked as red in the calender. One can select the interested date by simply clicking on the it and confirm by the *OK* button, then the spectra acquired in the selected date are listed in the **Data List** module and the number of files is display in the **Counts** module next to the **Choose Date** module. If specific data are going to process, one can click the *LOAD* button in the **Select Data**

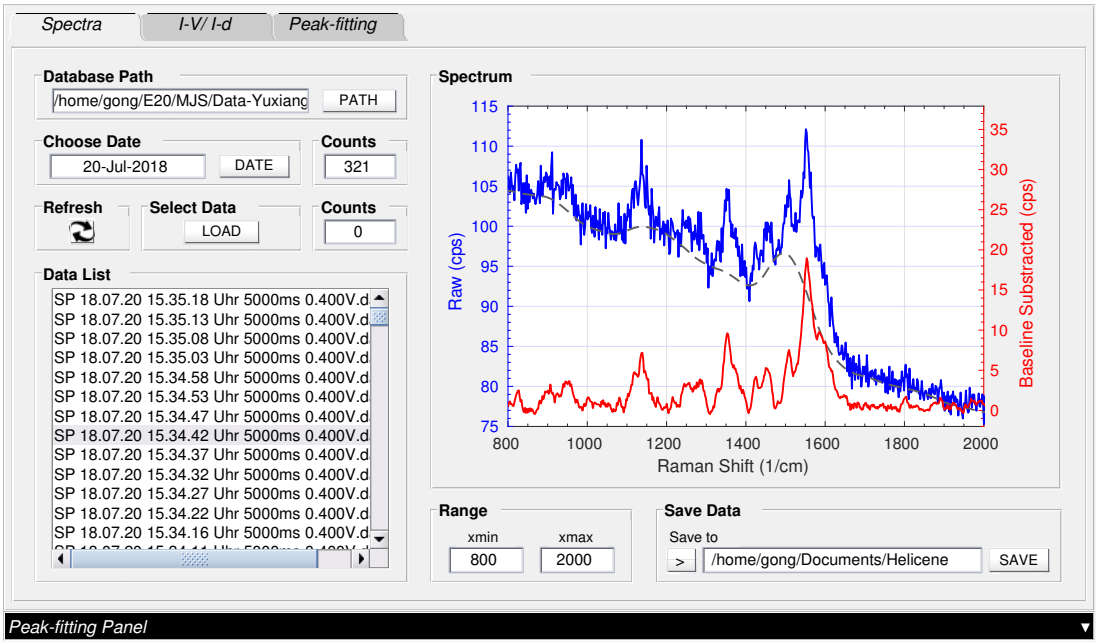

FIGURE B.1: The spectra viewer tab of the software.

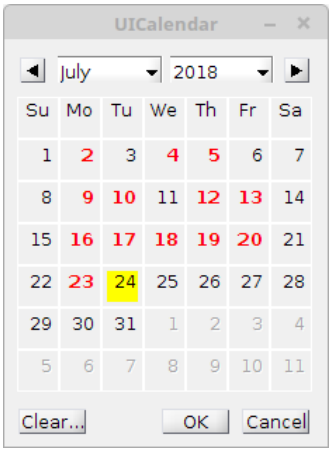

FIGURE B.2: The pop-up calender after push the *DATE* button. The dates when the spectra are acquired are marked as red. The yellow marker indicates the current date.

module, and select the files in the pop-up window. The assigned files are listed in the **Data List**, and the number is display in the adjacent **Counts** module.

By clicking on a filename or striking the up/ down arrow keys on the keyboard, the corresponding spectrum is displayed in the **Spectrum** module. A XYY plot is displayed whose X-axis is the Raman shift $(1/cm)$, left Y-axis indicates the intensity of the raw data (blue) and right Y-axis is the intensity after baseline correction (red). The rolling-circle filter (RCF) is used to subtract the baseline as introduce in Section 3.5. The display Raman shift range can be change in the **Range** module and the intensity is adjusted automatically according to the window size.

If a certain spectrum needs to be saved, the save path can be assigned by clicking the > button in the **Save Data** module and a spectrum file contains the baseline subtracted

data with an appended '*_BC*' (Baseline Corrected) to its filename is created by clicking the *SAVE* button.

B.2 *I-d/I-V* Viewer

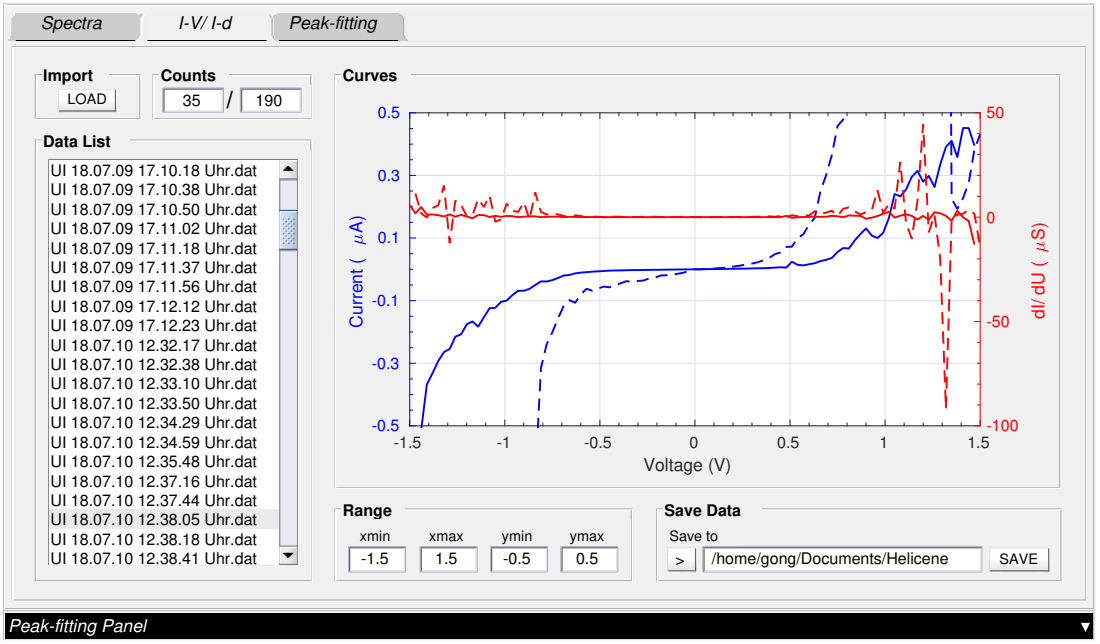

FIGURE B.3: The *I-d/I-V* viewer tab of the software.

The *I-d/I-V* viewer is presented in Fig. B.3. Same as the data loading function in the spectra viewer, the *I-V* or *I-d* files can be selected by clicking the *LOAD* in the **Import** module and listed in the **Data List** module. The current file index as well as the total number of files are displayed in the **Counts** module.

A file is saved with the name contains the data type (UI or Id), the acquired date and time (e.g. 'UI 18.12.31 12.30.05 Uhr.dat'). If a file contains *I-V* data (i.e. filename start with UI), the **Curves** module displays a XYY plot whose X-axis is the voltage, left Y-axis is the current (μA) and right Y-axis is the conductance (dI/ dU μS). The 'xmin' and 'xmax' values in the **Range** module are automatically assigned to -1.5 and 1.5 separately. If a *I-d* data is selected in the **Data List**, the **Curves** module displays a XY plot with X-axis as the distance ($\mathring{A}$) and Y-axis as the current (nA). The range of interest can be changed by typing values in the **Range** module. Once certain values are assigned, they are not alternated by selecting other files.

To save a specific file, a save path has to be chosen and the filename is attached with a '*_selected*' character.

B.3 Peak Analysis Panel

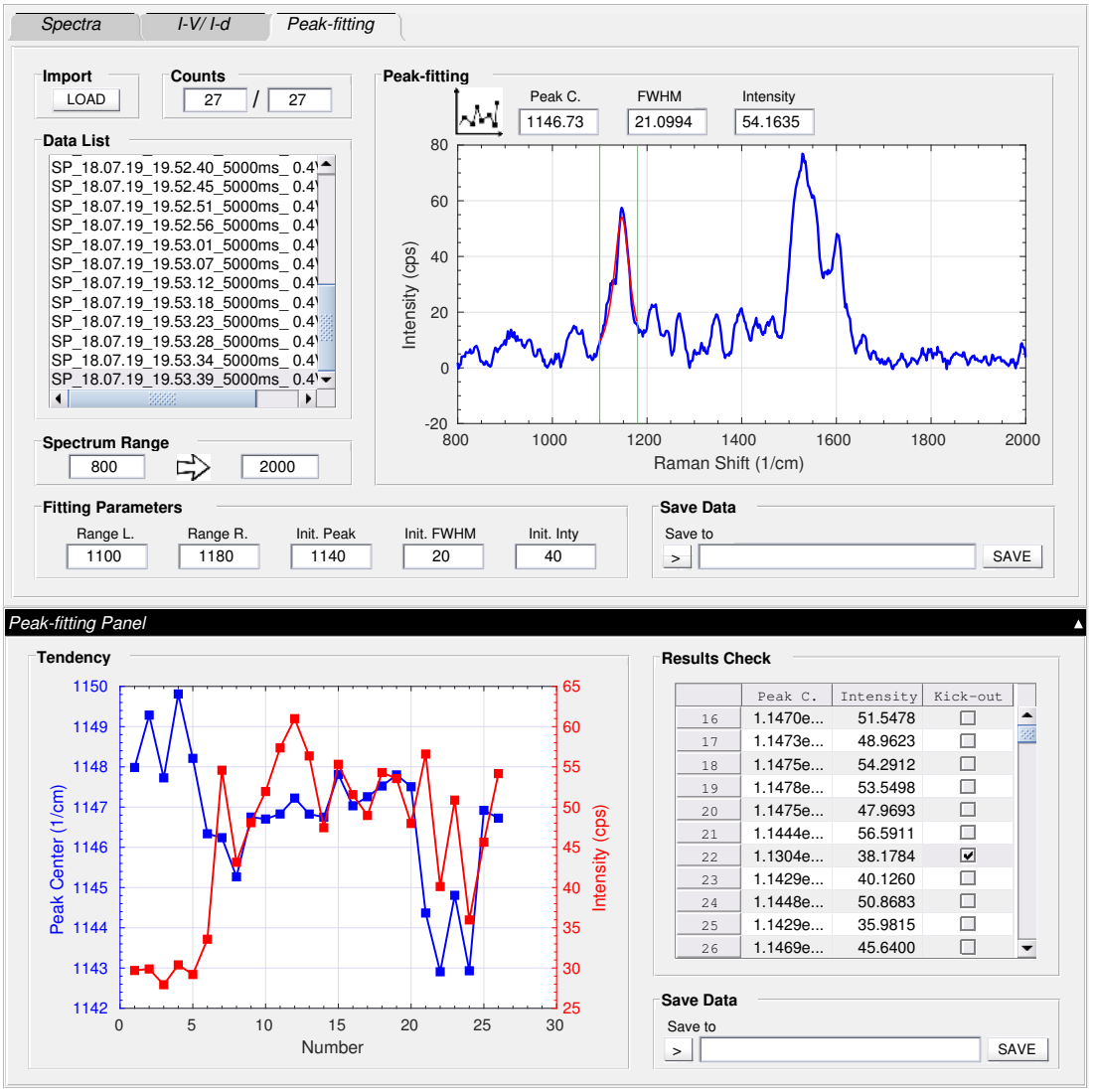

FIGURE B.4: The peak analysis panel of the software.

The peak-fitting tab is a foldable panel as illustrated in Fig. B.4. The lower panel can be hidden when the spectra and *I-V/I-d* viewers are used. The files can be loaded through the **Import** module and listed in the **Data List** which procedure is the same as the spectra viewer. The index and counts are displayed in the **Counts** module.

A selected spectrum whose baseline is automatically subtracted with the RCF is displayed in the **Peak-fitting** module. The Raman shift range can be changed in the **Spectrum Range** module. The initial parameters are assigned in **Fitting Parameters** to perform the peak-fitting as introduced in Section 3.5. Two green lines bounds the fitting range according to the parameters 'Range L.' and 'Range R.'. The fitted peak is plot in red color and its parameters are displayed on the top of the axes in the **Peak-fitting** module. Synchronously, the fitted peak center as well as the intensity are plotted as a function of the data index in the **Tendency** module. The **Results Check** module enables the user to get rid of the 'bad' values by checking the box in the *Kick-out* column. If a group of results is checked, the peak center as well as the intensity values will disappear in the **Tendency** module and the tendency curves are replotted. In this way, the overall trend will not be affected by a few abnormal data points.

The **Save Data** module at the lower panel is used to save the unchecked parameters in the **Results Check** module plus the FWHM list to an assign folder. The saved filename is 'parameters.txt'. The upper **Save Data** module has the same function as in the spectra viewer to save certain baseline corrected spectrum.

Appendix C

Steady-state and Time-resolved Spectroscopy in BPA

Time resolved IR spectra were obtained with a pump-probe setup based on a commercial Ti:sapphire amplifier (Libra, Coherent Inc.) with pulse duration of 130 fs, central wavelength of 800 nm, and repetition rate of 1 kHz. Part of the output was frequency doubled to obtain pump pulses at 400 nm with an energy of 0.5 μJ. Their polarization is adjusted to a magic angle (54.7°) setting with respect to the probe beam. To generate probe pulses, the signal and idler pulses produced by a two-stage optical parametric amplifier are overlapped in a type I AgGaS2 crystal to yield mid-IR light via difference frequency mixing. Probe pulses were tuned to 1500 cm^{-1} (spectral width $\sim$ 200 cm^{-1}). Pump and part of the probe beam are overlapped at the position of the sample. The remaining fraction of the probe passes the sample without spatial overlap with the excitation pulse and serves as an additional reference. The probe beams are spectrally resolved in a polychromator (SureSpectrum/Chromex 250is) and recorded on a 2×64 pixel HgCdTe detector (InfraRed Associates Inc.). The spectral resolution of the system is 2 cm^{-1}. Transient dynamics are monitored as the change in the optical density $\Delta OD = -log(T/T0)$ with T being the probe beam's transmission through an excited sample and T0 the transmission through an unexcited sample, i.e. with pump beam blocked. The sample compartment is flushed with dry air to avoid absorption lines due to atmospheric water vapor. The sample was pumped through a cuvette consisting of two 2 mm thick CaF_2 windows with a PTFE spacer of about 90 μm thickness in between from a reservoir in a closed cycle. To avoid degradation of the sample in the course of a longer measurement a large sample volume of 40 ml was used.

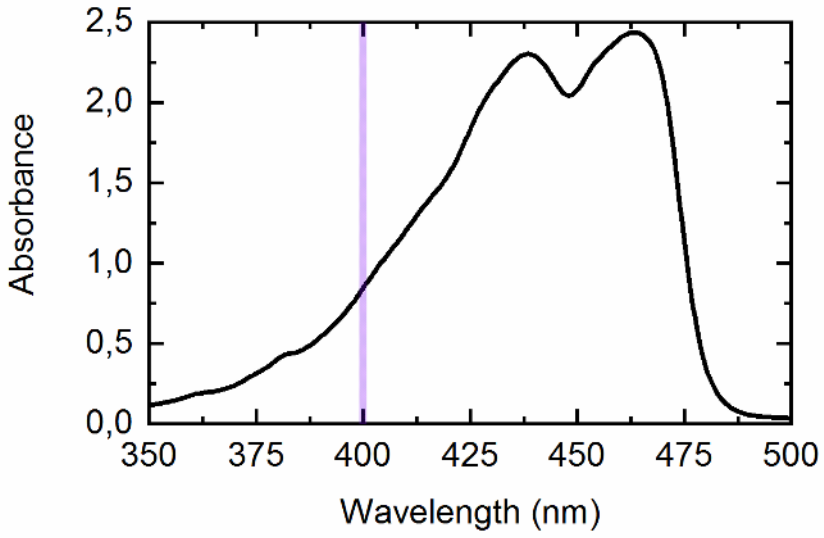

FIGURE C.1: UVvis absorption spectrum of BPA in DCM. Indicated in purple is the spectral position of the pump in the time resolved experiments.

9, 10 Bis-penylethynyl-antracene (BPA, SIGMA) was solved in dichloromethane (DCM) nearly to saturation at room temperature to provide sufficient absorption in the pump-probe experiment at lower wavelengths. No unsolved BPA crystals were observable in the solution. The spectrum of BPA in the visible spectral range was measured with a Shimadzu UV 1800 spectrophotometer and shows a structured absorption band between 350 and 480 nm (see Fig. C.1). The vibrational structure can be modeled by a vibrational progression with a mode spacing of $\Delta\nu/c = 1166\ cm^{-1}$ comparable with the spacing reported for another anthracene derivative [304] and with ν_{0-0} approximately centered around 460 nm and ν_{0-3} at ca. 400 nm. Excitation of the sample at this spectral position therefore leads to a vibrationally excited electronic S_1 state.

The infrared absorption spectrum of BPA in DCM was measured with a Bruker IFS 66 v/s FTIR spectrometer purged with dry air and is given in Fig. C.2. The spectrum of the pure solvent was measured separately in the same cuvette. The most prominent vibrational mode that is not obscured by the solvent is centered at 1492 cm^{-1}. Comparing the experimental vibrational spectrum with DFT calculations (see Fig. C.3) leads to the assignment of this mode to a stretching vibration of the phenyl rings, accounting for a scaling factor of 0.971 for the x-axis. Note that the calculated spectra represent a molecule with arrested thiol end groups rather than a free molecule and are thus not expected to be completely identical.

Transient pump probe spectra upon excitation of the sample at 400 nm show a sharp absorption feature at 1492 cm^{-1} that is already present at earliest times and is preceded by perturbed free induction decay (PFID). This signal at negative delay times is present for sharp absorption lines, where the dephasing time is longer than the probe pulse [305]. As shown in Fig. C.4, this distinctive signature that we attribute to absorption

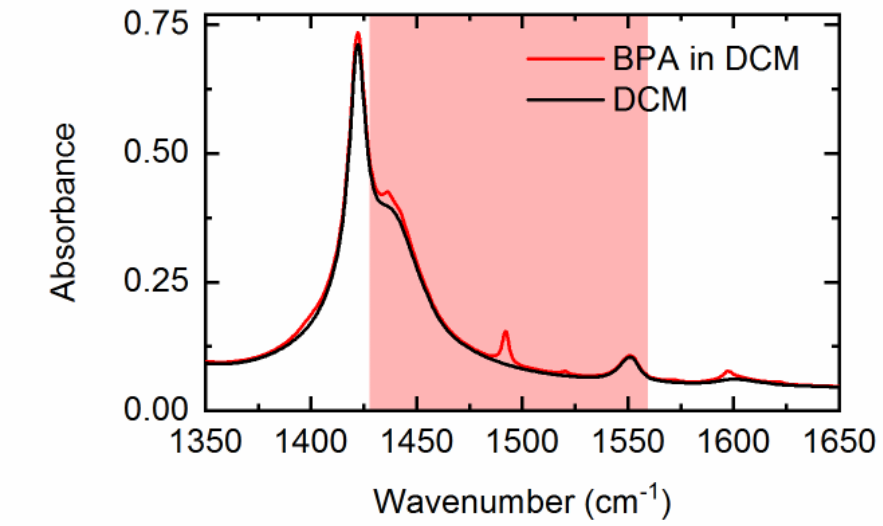

FIGURE C.2: FTIR absorption spectra of a saturated solution of BPA in DCM and of the pure solvent. Indicated in red is the spectral range covered by the probe pulse in the time resolved measurements.

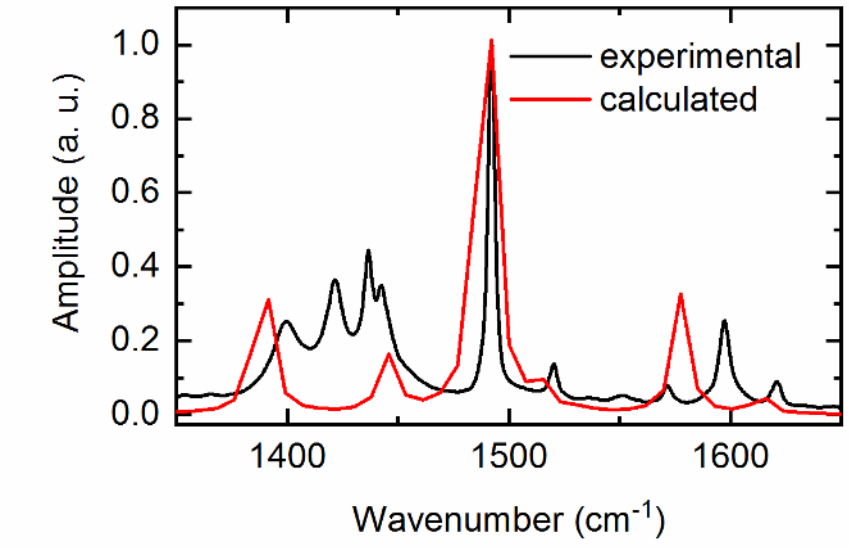

FIGURE C.3: FTIR absorption spectrum of BPEA in DCM corrected by solvent absorption compared with DFT calculated spectrum (x-axis scaled by 0.971).

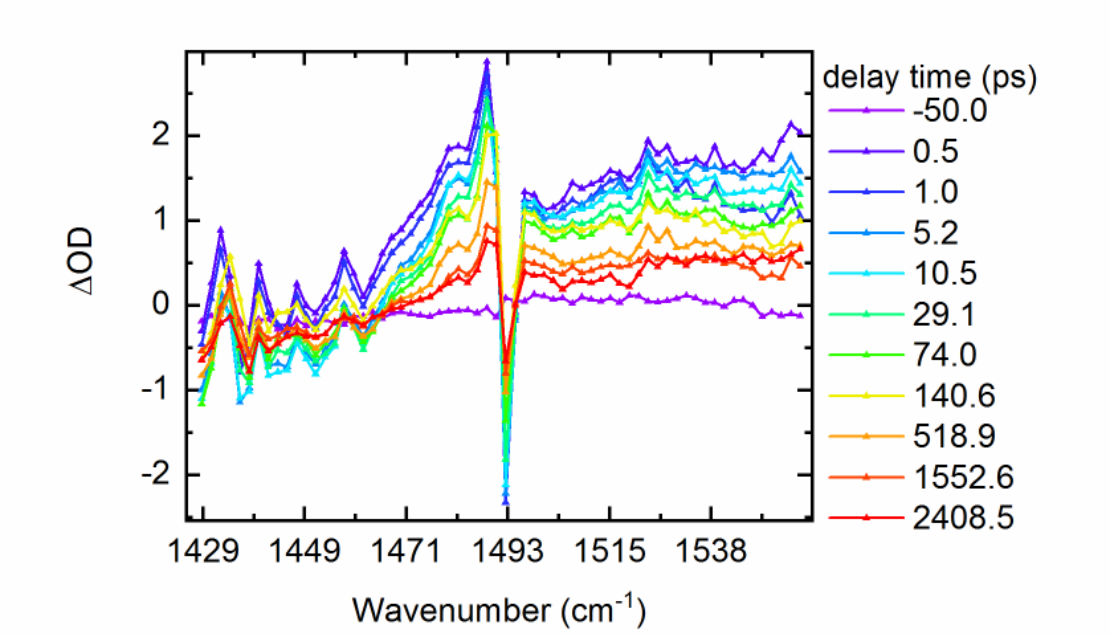

FIGURE C.4: Pump-probe spectra for indicated delay times.

by the BPA molecule upon comparison with the FTIR spectra is overlaid with a broad spectrally unspecific absorption also present for short delay times. The amplitude of this background decays with time. We attribute it to direct heating of the solvent via two-photon absorption at 400 nm. FTIR spectra of DCM for several temperatures (not shown) indicate a broad absorption change over the spectral range covered in the pump-probe measurements. Absorbance changes below 1470 cm^{-1} have to be considered with caution due to the onset of absorption in the solvent.

A global fit of the data in the whole spectral range with four exponentials results in time constants of 0.7 ps, 37 ps, 282 ps and 3000 ps. The lifetime of 3 ns was fixed to the given value on the basis of S_1 lifetimes determined in fluorescence measurements reported in the literature [306, 307]. This is necessary, since the mechanical delay stage limits the time window that can be covered to 3 ns. Therefore, lifetimes of some nanoseconds, as expected to be present in BPA, can otherwise not be accounted for accurately in the fit procedure.

To determine the time constant for internal vibrational relaxation we have to separate this process from intermolecular energy relaxation from solute to solvent that is mostly considered to happen subsequently. To this end, we take advantage of the concept of an internal temperature of the molecule that is not defined before equilibrium between the vibrational modes is reached. From this point onwards temperature related signatures in the spectrum should only change in amplitude, it at all. This is, because steady-state spectra of the change in absorption upon a variation of temperature show only a very slight shift at most, while the spectral profile of the absorption change stays the same.

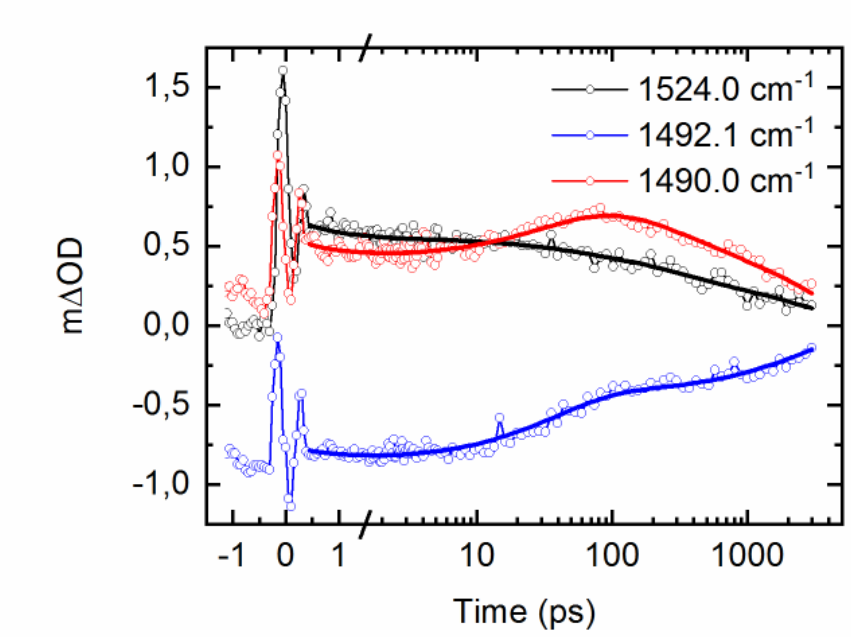

FIGURE C.5: Global fit with four exponentials modeled to the data. Transients are shown for a spectral position where predominantly direct heating of the solvent is observed (black), as well as for the negative and positive absorption maximum of the absorption change associated with the BPA molecule. The x-axis is linear up to 1.5 ps and logarithmic afterwards.

Taking a closer look at the BPA related changes in the transient pump-probe spectra around 1491 cm^{-1}, a slight spectral change can be observed in the positive absorption of the sharp differential-like spectral signature (see Fig. 4.8 in the Chapter 4, indicated by the arrow). Here, a slight shoulder begins to emerge for times longer than 10 ps. No further spectral change is observed for longer delay times. The spectra have been set to zero between 1496 and 1510 cm^{-1} to allow for assessing spectral changes in the sharp absorption feature regardless of the dynamics present in the broad background absorption. The time scale of 37 ps on which the increase in amplitude at this spectral position happens is also observable in the negative absorption maximum that decreases with the same rate. Away from the narrow BPA related absorption feature, the component has negligible amplitude. In Fig. C.5 the respective transients are presented along with one attributed to the solvent "background" for comparison. The distinctive signature at zero delay time is due to an artifact resulting from coherent interaction of pump and probe beam. The sharp absorption line due to BPA entails a perturbed free induction decay that leads to an absorption change for negative delay at this position, as mentioned above.

From the above we conclude that internal vibrational relaxation occurs with a time constant of 37 ± 4 ps. The associated spectral dynamics observed in the time resolved data are not consistent with a change upon variation in temperature as becomes clear when comparing them with the presented temperature series of FTIR spectra.

The observed time scale is comparably long for intramolecular relaxation. In other studies, time constants of some tens of picoseconds have mostly been associated with subsequent energy relaxation to the surrounding solvent [308–310] Yet, it has been also claimed, that complete internal energy redistribution might lie on the scale of 10 ps [311] and even compete with the 15-20 ps time scale for equilibration of the vibrational distribution with the surroundings [312]. The observation of relaxation times in BPA significantly longer than in anthracene is in line with the finding that vibrational coupling constants related to vibrational relaxation are reduced for anthracene derivatives substituted symmetrically at the 9 and 10 position, as in BPA [242]. The dephasing time of 3 ps, as read from an exponential fit to the PFID signal at 1492 cm^{-1} for negative delay times coincides with the time constant calculated as the inverse of the bandwidth according to Hamm et al. [305]. The full width at half maximum is obtained from a Lorentzian fit to the absorption profile in the FTIR spectrum at room temperature, thus assuming homogeneous line broadening [313]. In light of the unusually long dephasing time of a few picoseconds a likewise uncommonly slow internal vibrational relaxation seems plausible.

Bibliography

[1] M. Faraday *et al.*, "X. the bakerian lecture. experimental relations of gold (and other metals) to light," *Philosophical Transactions of the Royal Society of London*, vol. 147, pp. 145–181, 1857.

[2] I. Langmuir, "The constitution and fundamental properties of solids and liquids. ii. liquids.," *Journal of the American Chemical Society*, vol. 39, no. 9, pp. 1848–1906, 1917.

[3] K. B. Blodgett, "Monomolecular films of fatty acids on glass," *Journal of the American Chemical Society*, vol. 56, no. 2, pp. 495–495, 1934.

[4] K. B. Blodgett, "Films built by depositing successive monomolecular layers on a solid surface," *Journal of the American Chemical Society*, vol. 57, no. 6, pp. 1007–1022, 1935.

[5] W. Bigelow, D. Pickett, and W. Zisman, "Oleophobic monolayers: I. films adsorbed from solution in non-polar liquids," *Journal of Colloid Science*, vol. 1, no. 6, pp. 513–538, 1946.

[6] E. Synge, "Xxxviii. a suggested method for extending microscopic resolution into the ultra-microscopic region," *The London, Edinburgh, and Dublin Philosophical Magazine and Journal of Science*, vol. 6, no. 35, pp. 356–362, 1928.

[7] E. Ruska, *Die frühe Entwicklung der Elektronenlinsen und der Elektronenmikroskopie*, vol. 12. Deutsche Akademie der Naturforscher Leopoldina, 1979.

[8] M. Fleischmann, P. J. Hendra, and A. J. McQuillan, "Raman spectra of pyridine adsorbed at a silver electrode," *Chemical Physics Letters*, vol. 26, no. 2, pp. 163–166, 1974.

[9] A. Aviram and M. A. Ratner, "Molecular rectifiers," *Chemical Physics Letters*, vol. 29, no. 2, pp. 277–283, 1974.

[10] G. Binnig and H. Rohrer, "Scanning tunneling microscopy," *Surface science*, vol. 126, no. 1-3, pp. 236–244, 1983.

[11] G. Binnig, C. F. Quate, and C. Gerber, "Atomic force microscope," *Physical review letters*, vol. 56, no. 9, p. 930, 1986.

[12] W. Moerner, T. Plakhotnik, T. Irngartinger, M. Croci, V. Palm, and U. P. Wild, "Optical probing of single molecules of terrylene in a shpol'kii matrix: A two-state single-molecule switch," *The Journal of Physical Chemistry*, vol. 98, no. 30, pp. 7382–7389, 1994.

[13] M. Bates, T. R. Blosser, and X. Zhuang, "Short-range spectroscopic ruler based on a single-molecule optical switch," *Physical review letters*, vol. 94, no. 10, p. 108101, 2005.

[14] M. Heilemann, E. Margeat, R. Kasper, M. Sauer, and P. Tinnefeld, "Carbocyanine dyes as efficient reversible single-molecule optical switch," *Journal of the American Chemical Society*, vol. 127, no. 11, pp. 3801–3806, 2005.

[15] S. Y. Quek, M. Kamenetska, M. L. Steigerwald, H. J. Choi, S. G. Louie, M. S. Hybertsen, J. Neaton, and L. Venkataraman, "Mechanically controlled binary conductance switching of a single-molecule junction," *Nature nanotechnology*, vol. 4, no. 4, p. 230, 2009.

[16] P. J. Choi, L. Cai, K. Frieda, and X. S. Xie, "A stochastic single-molecule event triggers phenotype switching of a bacterial cell," *Science*, vol. 322, no. 5900, pp. 442–446, 2008.

[17] L. Kouwenhoven, "Single-molecule transistors," *Science*, vol. 275, no. 5308, pp. 1896–1897, 1997.

[18] W. Liang, M. P. Shores, M. Bockrath, J. R. Long, and H. Park, "Kondo resonance in a single-molecule transistor," *Nature*, vol. 417, no. 6890, p. 725, 2002.

[19] L. Yu, Z. K. Keane, J. W. Ciszek, L. Cheng, M. Stewart, J. Tour, and D. Natelson, "Inelastic electron tunneling via molecular vibrations in single-molecule transistors," *Physical review letters*, vol. 93, no. 26, p. 266802, 2004.

[20] B. Xu, X. Xiao, X. Yang, L. Zang, and N. Tao, "Large gate modulation in the current of a room temperature single molecule transistor," *Journal of the American Chemical Society*, vol. 127, no. 8, pp. 2386–2387, 2005.

[21] Z.-Z. Chen, R. Lü, and B.-f. Zhu, "Effects of electron-phonon interaction on nonequilibrium transport through a single-molecule transistor," *Physical Review B*, vol. 71, no. 16, p. 165324, 2005.

[22] C. Joachim and J. Gimzewski, "An electromechanical amplifier using a single molecule," *Chemical Physics Letters*, vol. 265, no. 3-5, pp. 353–357, 1997.

[23] C. Joachim and J. K. Gimzewski, "A nanoscale single-molecule amplifier and its consequences," *Proceedings of the IEEE*, vol. 86, no. 1, pp. 184–190, 1998.

[24] A. Aviram and M. A. Ratner, "Molecular rectifiers," *Chemical Physics Letters*, vol. 29, no. 2, pp. 277–283, 1974.

[25] J. Zhao, C. Zeng, X. Cheng, K. Wang, G. Wang, J. Yang, J. G. Hou, and Q. Zhu, "Single $C_{59}N$ molecule as a molecular rectifier," *Physical Review Letters*, vol. 95, jul 2005.

[26] M. Elbing, R. Ochs, M. Koentopp, M. Fischer, C. von Hänisch, F. Weigend, F. Evers, H. B. Weber, and M. Mayor, "A single-molecule diode," *Proceedings of the National Academy of Sciences of the United States of America*, vol. 102, no. 25, pp. 8815–8820, 2005.

[27] A. A. Kornyshev and A. M. Kuznetsov, "A new type of in situ single-molecule rectifier," *ChemPhysChem*, vol. 7, pp. 1036–1040, may 2006.

[28] C. P. Collier, E. W. Wong, M. Belohradský, F. M. Raymo, J. F. Stoddart, P. J. Kuekes, R. S. Williams, and J. R. Heath, "Electronically configurable molecular-based logic gates," *Science*, vol. 285, pp. 391–394, jul 1999.

[29] S. Ami, M. Hliwa, and C. Joachim, "Molecular OR and AND logic gates integrated in a single molecule," *Chemical Physics Letters*, vol. 367, no. 5, pp. 662–668, 2003.

[30] Y. Chen, G.-Y. Jung, D. A. A. Ohlberg, X. Li, D. R. Stewart, J. O. Jeppesen, K. A. Nielsen, J. F. Stoddart, and R. S. Williams, "Nanoscale molecular-switch crossbar circuits," *Nanotechnology*, vol. 14, no. 4, p. 462, 2003.

[31] R. Stadler, S. Ami, C. Joachim, and M. Forshaw, "Integrating logic functions inside a single molecule," *Nanotechnology*, vol. 15, no. 4, p. 5115, 2004.

[32] E. A. Osorio, T. Bjørnholm, J.-M. Lehn, M. Ruben, and H. S. J. van der Zant, "Single-molecule transport in three-terminal devices," *Journal of Physics: Condensed Matter*, vol. 20, no. 37, p. 374121, 2008.

[33] Z. Donhauser, B. Mantooth, K. Kelly, L. Bumm, J. Monnell, J. Stapleton, D. Price, A. Rawlett, D. Allara, J. Tour, *et al.*, "Conductance switching in single molecules through conformational changes," *Science*, vol. 292, no. 5525, pp. 2303–2307, 2001.

[34] S. Kubatkin, A. Danilov, M. Hjort, J. Cornil, J.-L. Brédas, N. Stuhr-Hansen, P. Hedegård, and T. Bjørnholm, "Single-electron transistor of a single organic molecule with access to several redox states," *Nature*, vol. 425, no. 6959, p. 698, 2003.

[35] V. Iancu and S.-W. Hla, "Realization of a four-step molecular switch in scanning tunneling microscope manipulation of single chlorophyll-a molecules," *Proceedings of the National Academy of Sciences*, vol. 103, no. 37, pp. 13718–13721, 2006.

[36] L. Venkataraman, J. E. Klare, C. Nuckolls, M. S. Hybertsen, and M. L. Steigerwald, "Dependence of single-molecule junction conductance on molecular conformation," *Nature*, vol. 442, no. 7105, p. 904, 2006.

[37] Z. Liu, S.-Y. Ding, Z.-B. Chen, X. Wang, J.-H. Tian, J. R. Anema, X.-S. Zhou, D.-Y. Wu, B.-W. Mao, X. Xu, *et al.*, "Revealing the molecular structure of single-molecule junctions in different conductance states by fishing-mode tip-enhanced Raman spectroscopy," *Nature communications*, vol. 2, p. 305, 2011.

[38] Y. Kim, T. Pietsch, A. Erbe, W. Belzig, and E. Scheer, "Benzenedithiol: a broad-range single-channel molecular conductor," *Nano letters*, vol. 11, no. 9, pp. 3734–3738, 2011.

[39] C. Bruot, J. Hihath, and N. Tao, "Mechanically controlled molecular orbital alignment in single molecule junctions," *Nature nanotechnology*, vol. 7, no. 1, p. 35, 2012.

[40] W. Auwärter, K. Seufert, F. Bischoff, D. Ecija, S. Vijayaraghavan, S. Joshi, F. Klappenberger, N. Samudrala, and J. V. Barth, "A surface-anchored molecular four-level conductance switch based on single proton transfer," *Nature nanotechnology*, vol. 7, no. 1, p. 41, 2012.

[41] T. A. Su, H. Li, M. L. Steigerwald, L. Venkataraman, and C. Nuckolls, "Stereoelectronic switching in single-molecule junctions," *Nature chemistry*, vol. 7, no. 3, p. 215, 2015.

[42] T. Yelin, R. Korytar, N. Sukenik, R. Vardimon, B. Kumar, C. Nuckolls, F. Evers, and O. Tal, "Conductance saturation in a series of highly transmitting molecular junctions," *Nature materials*, vol. 15, no. 4, p. 444, 2016.

[43] G. Kastlunger and R. Stadler, "Bias-induced conductance switching in single molecule junctions containing a redox-active transition metal complex," *Monatshefte für Chemie-Chemical Monthly*, vol. 147, no. 10, pp. 1675–1686, 2016.

[44] A. Credi, V. Balzani, S. J. Langford, and J. F. Stoddart, "Logic operations at the molecular level. an xor gate based on a molecular machine," *Journal of the American Chemical Society*, vol. 119, no. 11, pp. 2679–2681, 1997.

[45] A. Prasanna de Silva and N. D. McClenaghan, "Proof-of-principle of molecular-scale arithmetic," *Journal of the American Chemical Society*, vol. 122, no. 16, pp. 3965–3966, 2000.

[46] D. Margulies, G. Melman, and A. Shanzer, "A molecular full-adder and full-subtractor, an additional step toward a moleculator," *Journal of the American Chemical Society*, vol. 128, no. 14, pp. 4865–4871, 2006.

[47] T. Gupta and M. E. Van Der Boom, "Redox-active monolayers as a versatile platform for integrating boolean logic gates," *Angewandte Chemie*, vol. 120, no. 29, pp. 5402–5406, 2008.

[48] T. Hugel, N. B. Holland, A. Cattani, L. Moroder, M. Seitz, and H. E. Gaub, "Single-molecule optomechanical cycle," *Science*, vol. 296, no. 5570, pp. 1103–1106, 2002.

[49] B. Brough, B. H. Northrop, J. J. Schmidt, H.-R. Tseng, K. N. Houk, J. F. Stoddart, and C.-M. Ho, "Evaluation of synthetic linear motor-molecule actuation energetics," *Proceedings of the National Academy of Sciences*, vol. 103, no. 23, pp. 8583–8588, 2006.

[50] P. Lussis, T. Svaldo-Lanero, A. Bertocco, C.-A. Fustin, D. A. Leigh, and A.-S. Duwez, "A single synthetic small molecule that generates force against a load," *Nature nanotechnology*, vol. 6, no. 9, p. 553, 2011.

[51] J. M. Mativetsky, G. Pace, M. Elbing, M. A. Rampi, M. Mayor, and P. Samori, "Azobenzenes as light-controlled molecular electronic switches in nanoscale metal-molecule- metal junctions," *Journal of the American Chemical Society*, vol. 130, no. 29, pp. 9192–9193, 2008.

[52] Y. Kim, A. Garcia-Lekue, D. Sysoiev, T. Frederiksen, U. Groth, and E. Scheer, "Charge transport in azobenzene-based single-molecule junctions," *Physical review letters*, vol. 109, no. 22, p. 226801, 2012.

[53] Y. Kim, T. J. Hellmuth, D. Sysoiev, F. Pauly, T. Pietsch, J. Wolf, A. Erbe, T. Huhn, U. Groth, U. E. Steiner, *et al.*, "Charge transport characteristics of diarylethene photoswitching single-molecule junctions," *Nano letters*, vol. 12, no. 7, pp. 3736–3742, 2012.

[54] Y. Cao, S. Dong, S. Liu, Z. Liu, and X. Guo, "Toward functional molecular devices based on graphene–molecule junctions," *Angewandte Chemie*, vol. 125, no. 14, pp. 3998–4002, 2013.

[55] E. Margapoti, J. Li, Ö. Ceylan, M. Seifert, F. Nisic, T. L. Anh, F. Meggendorfer, C. Dragonetti, C.-A. Palma, J. V. Barth, *et al.*, "A 2D semiconductor–self-assembled monolayer photoswitchable diode," *Advanced materials*, vol. 27, no. 8, pp. 1426–1431, 2015.

[56] E.-D. Fung, O. Adak, G. Lovat, D. Scarabelli, and L. Venkataraman, "Too hot for photon-assisted transport: Hot-electrons dominate conductance enhancement in illuminated single-molecule junctions," *Nano letters*, vol. 17, no. 2, pp. 1255–1261, 2017.

[57] M. Irie, "Diarylethenes for memories and switches," *Chemical Reviews*, vol. 100, no. 5, pp. 1685–1716, 2000.

[58] D. Dulić, S. J. van der Molen, T. Kudernac, H. Jonkman, J. De Jong, T. Bowden, J. Van Esch, B. Feringa, and B. Van Wees, "One-way optoelectronic switching of photochromic molecules on gold," *Physical review letters*, vol. 91, no. 20, p. 207402, 2003.

[59] C. Jia, J. Wang, C. Yao, Y. Cao, Y. Zhong, Z. Liu, Z. Liu, and X. Guo, "Conductance switching and mechanisms in single-molecule junctions," *Angewandte Chemie International Edition*, vol. 52, no. 33, pp. 8666–8670, 2013.

[60] C. Jia, A. Migliore, N. Xin, S. Huang, J. Wang, Q. Yang, S. Wang, H. Chen, D. Wang, B. Feng, *et al.*, "Covalently bonded single-molecule junctions with stable and reversible photoswitched conductivity," *Science*, vol. 352, no. 6292, pp. 1443–1445, 2016.

[61] Y. Kim, S. G. Bahoosh, D. Sysoiev, T. Huhn, F. Pauly, and E. Scheer, "Inelastic electron tunneling spectroscopy of difurylethene-based photochromic single-molecule junctions," *Beilstein journal of nanotechnology*, vol. 8, p. 2606, 2017.

[62] K. Hosaka, H. Shimada, H. Chiba, H. Katsuki, Y. Teranishi, Y. Ohtsuki, and K. Ohmori, "Ultrafast fourier transform with a femtosecond-laser-driven molecule," *Physical review letters*, vol. 104, no. 18, p. 180501, 2010.

[63] A. Schiffrin, T. Paasch-Colberg, N. Karpowicz, V. Apalkov, D. Gerster, S. Mühlbrandt, M. Korbman, J. Reichert, M. Schultze, S. Holzner, *et al.*, "Optical-field-induced current in dielectrics," *Nature*, vol. 493, no. 7430, p. 70, 2013.

[64] H. Valkenier, C. M. Guédon, T. Markussen, K. S. Thygesen, S. J. van der Molen, and J. C. Hummelen, "Cross-conjugation and quantum interference: a general correlation?," *Physical Chemistry Chemical Physics*, vol. 16, no. 2, pp. 653–662, 2014.

[65] J.-H. Tian, B. Liu, X. Li, Z.-L. Yang, B. Ren, S.-T. Wu, N. Tao, and Z.-Q. Tian, "Study of molecular junctions with a combined surface-enhanced Raman and mechanically controllable break junction method," *Journal of the American Chemical Society*, vol. 128, no. 46, pp. 14748–14749, 2006.

[66] D. R. Ward, N. J. Halas, J. W. Ciszek, J. M. Tour, Y. Wu, P. Nordlander, and D. Natelson, "Simultaneous measurements of electronic conduction and Raman response in molecular junctions," *Nano letters*, vol. 8, no. 3, pp. 919–924, 2008.

[67] S. Kaneko, D. Murai, S. Marqués-González, H. Nakamura, Y. Komoto, S. Fujii, T. Nishino, K. Ikeda, K. Tsukagoshi, and M. Kiguchi, "Site-selection in single-molecule junction for highly reproducible molecular electronics," *Journal of the American Chemical Society*, vol. 138, no. 4, pp. 1294–1300, 2016.

[68] M.-N. Dessinges, T. Lionnet, X. G. Xi, D. Bensimon, and V. Croquette, "Single-molecule assay reveals strand switching and enhanced processivity of uvrd," *Proceedings of the National Academy of Sciences*, vol. 101, no. 17, pp. 6439–6444, 2004.

[69] I. De Vlaminck and C. Dekker, "Recent advances in magnetic tweezers," *Annual review of biophysics*, vol. 41, pp. 453–472, 2012.

[70] F. E. Kemmerich, M. Swoboda, D. J. Kauert, M. S. Grieb, S. Hahn, F. W. Schwarz, R. Seidel, and M. Schlierf, "Simultaneous single-molecule force and fluorescence sampling of dna nanostructure conformations using magnetic tweezers," *Nano letters*, vol. 16, no. 1, pp. 381–386, 2015.

[71] A. Ashkin, J. M. Dziedzic, J. Bjorkholm, and S. Chu, "Observation of a single-beam gradient force optical trap for dielectric particles," *Optics letters*, vol. 11, no. 5, pp. 288–290, 1986.

[72] A. Ashkin, K. Schütze, J. Dziedzic, U. Euteneuer, and M. Schliwa, "Force generation of organelle transport measured in vivo by an infrared laser trap," *Nature*, vol. 348, no. 6299, p. 346, 1990.

[73] U. Bockelmann, P. Thomen, B. Essevaz-Roulet, V. Viasnoff, and F. Heslot, "Unzipping dna with optical tweezers: high sequence sensitivity and force flips," *Biophysical journal*, vol. 82, no. 3, pp. 1537–1553, 2002.

[74] J. W. Black, M. Kamenetska, and Z. Ganim, "An optical tweezers platform for single molecule force spectroscopy in organic solvents," *Nano letters*, vol. 17, no. 11, pp. 6598–6605, 2017.

[75] A. Janshoff, M. Neitzert, Y. Oberdörfer, and H. Fuchs, "Force spectroscopy of molecular systems-single molecule spectroscopy of polymers and biomolecules," *Angewandte Chemie International Edition*, vol. 39, no. 18, pp. 3212–3237, 2000.

[76] B. Xu and N. J. Tao, "Measurement of single-molecule resistance by repeated formation of molecular junctions," *science*, vol. 301, no. 5637, pp. 1221–1223, 2003.

[77] D. J. Müller and Y. F. Dufrene, "Atomic force microscopy as a multifunctional molecular toolbox in nanobiotechnology," in *Nanoscience And Technology: A Collection of Reviews from Nature Journals*, pp. 269–277, World Scientific, 2010.

[78] R. Frisenda, G. D. Harzmann, J. A. Celis Gil, J. M. Thijssen, M. Mayor, and H. S. van der Zant, "Stretching-induced conductance increase in a spin-crossover molecule," *Nano letters*, vol. 16, no. 8, pp. 4733–4737, 2016.

[79] D. A. Davis, A. Hamilton, J. Yang, L. D. Cremar, D. Van Gough, S. L. Potisek, M. T. Ong, P. V. Braun, T. J. Martínez, S. R. White, *et al.*, "Force-induced

activation of covalent bonds in mechanoresponsive polymeric materials," *Nature*, vol. 459, no. 7243, p. 68, 2009.

[80] J. N. Ladenthin, T. Frederiksen, M. Persson, J. C. Sharp, S. Gawinkowski, J. Waluk, and T. Kumagai, "Force-induced tautomerization in a single molecule," *Nature chemistry*, vol. 8, no. 10, p. 935, 2016.

[81] D. Djukic, K. S. Thygesen, C. Untiedt, R. Smit, K. W. Jacobsen, and J. Van Ruitenbeek, "Stretching dependence of the vibration modes of a single-molecule pt- h 2- pt bridge," *Physical Review B*, vol. 71, no. 16, p. 161402, 2005.

[82] J. Cuevas, A. L. Yeyati, and A. Martín-Rodero, "Microscopic origin of conducting channels in metallic atomic-size contacts," *Physical review letters*, vol. 80, no. 5, p. 1066, 1998.

[83] E. Scheer, N. Agraït, J. C. Cuevas, A. L. Yeyati, B. Ludoph, A. Martín-Rodero, G. R. Bollinger, J. M. van Ruitenbeek, and C. Urbina, "The signature of chemical valence in the electrical conduction through a single-atom contact," *Nature*, vol. 394, no. 6689, p. 154, 1998.

[84] D. Gerster, J. Reichert, H. Bi, J. V. Barth, S. M. Kaniber, A. W. Holleitner, I. Visoly-Fisher, S. Sergani, and I. Carmeli, "Photocurrent of a single photosynthetic protein," *Nature Nanotechnology*, vol. 7, no. 10, pp. 673–676, 2012.

[85] P. E. Hasch, *Single-Molecule Junction Raman Spectroscopy on Distinct Metal-Molecule-Metal Systems*. PhD thesis, Technische Universität München, 2017.

[86] H. Bi, *Raman Spectroscopy on Single-Molecule Junctions*. PhD thesis, Technische Universität München, 2014.

[87] Y. Gong, "Electron-phonon interaction in current driven single molecule junctions," Master's thesis, Technische Universität München, 2013.

[88] H. Bi, C.-A. Palma, Y. Gong, P. Hasch, M. Elbing, M. Mayor, J. Reichert, and J. V. Barth, "Voltage-driven conformational switching with distinct Raman signature in a single-molecule junction," *Journal of the American Chemical Society*, vol. 140, no. 14, pp. 4835–4840, 2018.

[89] F. Chen, J. Hihath, Z. Huang, X. Li, and N. Tao, "Measurement of single-molecule conductance," *Annu. Rev. Phys. Chem.*, vol. 58, pp. 535–564, 2007.

[90] A. Nitzan and M. A. Ratner, "Electron transport in molecular wire junctions," *Science*, vol. 300, no. 5624, pp. 1384–1389, 2003.

[91] H. Park, J. Park, A. K. Lim, E. H. Anderson, A. P. Alivisatos, and P. L. McEuen, "Nanomechanical oscillations in a single-C 60 transistor," *Nature*, vol. 407, no. 6800, p. 57, 2000.

[92] F. Moresco, G. Meyer, K.-H. Rieder, H. Tang, A. Gourdon, and C. Joachim, "Conformational changes of single molecules induced by scanning tunneling microscopy manipulation: a route to molecular switching," *Physical Review Letters*, vol. 86, no. 4, p. 672, 2001.

[93] J. L. Zhang, J. Q. Zhong, J. D. Lin, W. P. Hu, K. Wu, G. Q. Xu, A. T. Wee, and W. Chen, "Towards single molecule switches," *Chemical Society Reviews*, vol. 44, no. 10, pp. 2998–3022, 2015.

[94] B. Capozzi, J. Xia, O. Adak, E. J. Dell, Z.-F. Liu, J. C. Taylor, J. B. Neaton, L. M. Campos, and L. Venkataraman, "Single-molecule diodes with high rectification ratios through environmental control," *Nature nanotechnology*, vol. 10, no. 6, p. 522, 2015.

[95] A. Vezzoli, R. J. Brooke, S. J. Higgins, W. Schwarzacher, and R. J. Nichols, "Single-molecule photocurrent at a metal–molecule–semiconductor junction," *Nano letters*, vol. 17, no. 11, pp. 6702–6707, 2017.

[96] E. Fung, J. Xia, B. Capozzi, L. Campos, L. Venkataraman, *et al.*, "Investigating single-molecule near-resonant charge transport in electrochemical environments," *Bulletin of the American Physical Society*, 2018.

[97] B. Lawson and M. Kamenetska, "Single molecule conductance of ferrocene at cryogenic and room temperature," *Bulletin of the American Physical Society*, 2019.

[98] M. Elbing, R. Ochs, M. Koentopp, M. Fischer, C. von Hänisch, F. Weigend, F. Evers, H. B. Weber, and M. Mayor, "A single-molecule diode," *Proceedings of the National Academy of Sciences of the United States of America*, vol. 102, no. 25, pp. 8815–8820, 2005.

[99] J. Reichert, R. Ochs, D. Beckmann, H. B. Weber, M. Mayor, and H. v. Löhneysen, "Driving current through single organic molecules," *Phys. Rev. Lett.*, vol. 88, p. 176804, Apr 2002.

[100] N. Zhitenev, H. Meng, and Z. Bao, "Conductance of small molecular junctions," *Physical review letters*, vol. 88, no. 22, p. 226801, 2002.

[101] M. A. Reed, C. Zhou, C. Muller, T. Burgin, and J. Tour, "Conductance of a molecular junction," *Science*, vol. 278, no. 5336, pp. 252–254, 1997.

[102] L. Venkataraman, J. E. Klare, I. W. Tam, C. Nuckolls, M. S. Hybertsen, and M. L. Steigerwald, "Single-molecule circuits with well-defined molecular conductance," *Nano letters*, vol. 6, no. 3, pp. 458–462, 2006.

[103] H. B. Akkerman and B. de Boer, "Electrical conduction through single molecules and self-assembled monolayers," *Journal of Physics: Condensed Matter*, vol. 20, no. 1, p. 013001, 2007.

[104] M. Kiguchi, T. Takahashi, Y. Takahashi, Y. Yamauchi, T. Murase, M. Fujita, T. Tada, and S. Watanabe, "Electron transport through single molecules comprising aromatic stacks enclosed in self-assembled cages," *Angewandte Chemie*, vol. 123, no. 25, pp. 5826–5829, 2011.

[105] S. Elke and C. J. Carlos, *Molecular electronics: An introduction to theory and experiment*, vol. 15. World Scientific, 2017.

[106] D. Krüger, H. Fuchs, R. Rousseau, D. Marx, and M. Parrinello, "Pulling monatomic gold wires with single molecules: an ab initio simulation," *Physical review letters*, vol. 89, no. 18, p. 186402, 2002.

[107] S. Kano, T. Tada, and Y. Majima, "Nanoparticle characterization based on stm and sts," *Chemical Society Reviews*, vol. 44, no. 4, pp. 970–987, 2015.

[108] R. J. Nichols, W. Haiss, S. J. Higgins, E. Leary, S. Martin, and D. Bethell, "The experimental determination of the conductance of single molecules," *Physical Chemistry Chemical Physics*, vol. 12, no. 12, pp. 2801–2815, 2010.

[109] M. Tsutsui and M. Taniguchi, "Single molecule electronics and devices," *Sensors*, vol. 12, no. 6, pp. 7259–7298, 2012.

[110] Z. Keane, L. Yu, and D. Natelson, "Magnetoresistance of atomic-scale electromigrated nickel nanocontacts," *Applied physics letters*, vol. 88, no. 6, p. 062514, 2006.

[111] H. Park, A. K. Lim, A. P. Alivisatos, J. Park, and P. L. McEuen, "Fabrication of metallic electrodes with nanometer separation by electromigration," *Applied Physics Letters*, vol. 75, no. 2, pp. 301–303, 1999.

[112] C. Joachim, J. Gimzewski, Aviram, and A, "Electronics using hybrid-molecular and mono-molecular devices," *Nature*, vol. 408, no. 6812, p. 541, 2000.

[113] X. Xiao, B. Xu, and N. J. Tao, "Measurement of single molecule conductance: Benzenedithiol and benzenedimethanethiol," *Nano Letters*, vol. 4, no. 2, pp. 267–271, 2004.

[114] X. Xiao, B. Xu, and N. Tao, "Conductance titration of single-peptide molecules," *Journal of the American Chemical Society*, vol. 126, no. 17, pp. 5370–5371, 2004.

[115] N. Tao, "Electron transport in molecular junctions," *Nature nanotechnology*, vol. 1, no. 3, p. 173, 2006.

[116] X. Baillin, C. Joachim, and G. Poupon, *Nanopackaging: From Nanomaterials to the Atomic Scale*. Springer, 2016.

[117] M. Kiguchi, N. Sekiguchi, and K. Murakoshi, "Electric conductance of metal nanowires at mechanically controllable break junctions under electrochemical potential control," *Surface Science*, vol. 601, no. 22, pp. 5262–5265, 2007.

[118] E. Lörtscher, H. B. Weber, and H. Riel, "Statistical approach to investigating transport through single molecules," *Physical review letters*, vol. 98, no. 17, p. 176807, 2007.

[119] R. Landauer, "Spatial variation of currents and fields due to localized scatterers in metallic conduction," *IBM Journal of Research and Development*, vol. 1, no. 3, pp. 223–231, 1957.

[120] R. Landauer, "Can a length of perfect conductor have a resistance?," *Physics Letters A*, vol. 85, no. 2, pp. 91–93, 1981.

[121] B. I. Halperin, "Quantized hall conductance, current-carrying edge states, and the existence of extended states in a two-dimensional disordered potential," *Physical Review B*, vol. 25, no. 4, p. 2185, 1982.

[122] M. Büttiker, "Absence of backscattering in the quantum hall effect in multiprobe conductors," *Physical Review B*, vol. 38, no. 14, p. 9375, 1988.

[123] K. Takayanagi, Y. Kondo, and H. Ohnishi, "Suspended gold nanowires: ballistic transport of electrons," *JSAP international*, vol. 3, no. 8, 2001.

[124] G. Breit and E. Wigner, "Capture of slow neutrons," *Physical review*, vol. 49, no. 7, p. 519, 1936.

[125] A. Nitzan, J. Jortner, J. Wilkie, A. L. Burin, and M. A. Ratner, "Tunneling time for electron transfer reactions," *The Journal of Physical Chemistry B*, vol. 104, no. 24, pp. 5661–5665, 2000.

[126] D. Segal, A. Nitzan, W. B. Davis, M. R. Wasielewski, and M. A. Ratner, "Electron transfer rates in bridged molecular systems 2. a steady-state analysis of coherent tunneling and thermal transitions," *The Journal of Physical Chemistry B*, vol. 104, no. 16, pp. 3817–3829, 2000.

[127] D. Averin and K. Likharev, "Coulomb blockade of single-electron tunneling, and coherent oscillations in small tunnel junctions," *Journal of low temperature physics*, vol. 62, no. 3-4, pp. 345–373, 1986.

[128] A. Nitzan, "The relationship between electron transfer rate and molecular conduction 2. the sequential hopping case," *Israel journal of chemistry*, vol. 42, no. 2-3, pp. 163–166, 2002.

[129] T. Hines, I. Diez-Perez, J. Hihath, H. Liu, Z.-S. Wang, J. Zhao, G. Zhou, K. Müllen, and N. Tao, "Transition from tunneling to hopping in single molecular junctions by measuring length and temperature dependence," *Journal of the American Chemical Society*, vol. 132, no. 33, pp. 11658–11664, 2010.

[130] L. Xiang, J. L. Palma, C. Bruot, V. Mujica, M. A. Ratner, and N. Tao, "Intermediate tunnelling–hopping regime in dna charge transport," *Nature chemistry*, vol. 7, no. 3, p. 221, 2015.

[131] X. Cui, A. Primak, X. Zarate, J. Tomfohr, O. Sankey, A. Moore, T. Moore, D. Gust, G. Harris, and S. Lindsay, "Reproducible measurement of single-molecule conductivity," *Science*, vol. 294, no. 5542, pp. 571–574, 2001.

[132] W. Haiss, R. J. Nichols, H. van Zalinge, S. J. Higgins, D. Bethell, and D. J. Schiffrin, "Measurement of single molecule conductivity using the spontaneous formation of molecular wires," *Physical Chemistry Chemical Physics*, vol. 6, no. 17, pp. 4330–4337, 2004.

[133] G. Fagas, P. Delaney, and J. C. Greer, "Independent particle descriptions of tunneling using the many-body quantum transport approach," *Physical Review B*, vol. 73, no. 24, p. 241314, 2006.

[134] X. Li, J. He, J. Hihath, B. Xu, S. M. Lindsay, and N. Tao, "Conductance of single alkanedithiols: conduction mechanism and effect of molecule- electrode contacts," *Journal of the American Chemical Society*, vol. 128, no. 6, pp. 2135–2141, 2006.

[135] C. Li, I. Pobelov, T. Wandlowski, A. Bagrets, A. Arnold, and F. Evers, "Charge transport in single Au-alkanedithiol-Au junctions: coordination geometries and conformational degrees of freedom," *Journal of the American Chemical Society*, vol. 130, no. 1, pp. 318–326, 2008.

[136] M. T. González, J. Brunner, R. Huber, S. Wu, C. Schönenberger, and M. Calame, "Conductance values of alkanedithiol molecular junctions," *New Journal of Physics*, vol. 10, no. 6, p. 065018, 2008.

[137] W. Wang, T. Lee, and M. A. Reed, "Mechanism of electron conduction in self-assembled alkanethiol monolayer devices," *Physical Review B*, vol. 68, no. 3, p. 035416, 2003.

[138] C. Raman and K. Krishnan, "A new type of secondary radiation," *Nature*, vol. 121, no. 3048, pp. 501–502, 1928.

[139] Wikimedia Commons, "Ramanscattering," 2007. [Online; accessed 17th June 2019].

[140] J. W. Strutt, "XV. on the light from the sky, its polarization and colour," *The London, Edinburgh, and Dublin Philosophical Magazine and Journal of Science*, vol. 41, no. 271, pp. 107–120, 1871.

[141] J. W. Strutt, "LVIII. on the scattering of light by small particles," *The London, Edinburgh, and Dublin Philosophical Magazine and Journal of Science*, vol. 41, no. 275, pp. 447–454, 1871.

[142] L. Rayleigh, "X. on the electromagnetic theory of light," *The London, Edinburgh, and Dublin Philosophical Magazine and Journal of Science*, vol. 12, no. 73, pp. 81–101, 1881.

[143] L. Rayleigh, "XXXIV. on the transmission of light through an atmosphere containing small particles in suspension, and on the origin of the blue of the sky," *The London, Edinburgh, and Dublin Philosophical Magazine and Journal of Science*, vol. 47, no. 287, pp. 375–384, 1899.

[144] E. Smith and G. Dent, *Modern Raman spectroscopy: a practical approach*. John Wiley & Sons, 2013.

[145] D. Rousseau, J. Friedman, and P. Williams, "Topics in current physics," in *Raman spectroscopy of gases and liquids*, vol. 2, Springer Berlin, 1979.

[146] R. J. Clark and T. J. Dines, "Theory of the resonance electronic Raman effect," *Molecular Physics*, vol. 45, no. 6, pp. 1153–1162, 1982.

[147] R. J. Clark and T. J. Dines, "Resonance Raman spectroscopy, and its application to inorganic chemistry. new analytical methods (27)," *Angewandte Chemie International Edition*, vol. 25, no. 2, pp. 131–158, 1986.

[148] Wikimedia Commons, "Sketch of surface plasmon," 2013. [Online; accessed 17th June 2019].

[149] Sermrock, "Conceptual illustration of SERS." [Online; accessed 17th June 2019].

[150] Bruker Nano Surface, "General setup for linear and non-linear tip-assisted scanning probe microscopy (SPM) and optical spectroscopies.," 2013. [Online; accessed 17th June 2019].

[151] C. Zeh, R. Spittel, S. Unger, J. Opitz, B. Köhler, J. Kirchhof, H. Bartelt, and L. M. Eng, "Polarization mode preservation in elliptical index tailored optical fibers for apertureless scanning near-field optical microscopy," *Applied Physics Letters*, vol. 97, no. 10, p. 103108, 2010.

[152] D. L. Jeanmaire and R. P. Van Duyne, "Surface Raman spectroelectrochemistry: Part I. heterocyclic, aromatic, and aliphatic amines adsorbed on the anodized silver electrode," *Journal of electroanalytical chemistry and interfacial electrochemistry*, vol. 84, no. 1, pp. 1–20, 1977.

[153] J. R. Lombardi and R. L. Birke, "A unified approach to surface-enhanced Raman spectroscopy," *The Journal of Physical Chemistry C*, vol. 112, no. 14, pp. 5605–5617, 2008.

[154] E. J. Blackie, E. C. L. Ru, and P. G. Etchegoin, "Single-molecule surface-enhanced Raman spectroscopy of nonresonant molecules," *Journal of the American Chemical Society*, vol. 131, no. 40, pp. 14466–14472, 2009.

[155] K. Kneipp and H. Kneipp, "Single molecule Raman scattering," *applied spectroscopy*, vol. 60, no. 12, pp. 322A–334A, 2006.

[156] S. Nie and S. R. Emory, "Probing single molecules and single nanoparticles by surface-enhanced Raman scattering," *science*, vol. 275, no. 5303, pp. 1102–1106, 1997.

[157] K. Kneipp, Y. Wang, H. Kneipp, L. T. Perelman, I. Itzkan, R. R. Dasari, and M. S. Feld, "Single molecule detection using surface-enhanced Raman scattering (sers)," *Physical review letters*, vol. 78, no. 9, p. 1667, 1997.

[158] P. Hermann, A. Hermelink, V. Lausch, G. Holland, L. Möller, N. Bannert, and D. Naumann, "Evaluation of tip-enhanced Raman spectroscopy for characterizing different virus strains," *Analyst*, vol. 136, no. 6, pp. 1148–1152, 2011.

[159] B. Pettinger, B. Ren, G. Picardi, R. Schuster, and G. Ertl, "Tip-enhanced Raman spectroscopy (TERS) of malachite green isothiocyanate at au (111): bleaching behavior under the influence of high electromagnetic fields," *Journal of Raman Spectroscopy*, vol. 36, no. 6-7, pp. 541–550, 2005.

[160] M. S. Anderson, "Locally enhanced Raman spectroscopy with an atomic force microscope," *Applied Physics Letters*, vol. 76, no. 21, pp. 3130–3132, 2000.

[161] R. M. Stöckle, Y. D. Suh, V. Deckert, and R. Zenobi, "Nanoscale chemical analysis by tip-enhanced Raman spectroscopy," *Chemical Physics Letters*, vol. 318, no. 1-3, pp. 131–136, 2000.

[162] N. Hayazawa, Y. Inouye, Z. Sekkat, and S. Kawata, "Metallized tip amplification of near-field Raman scattering," *Optics Communications*, vol. 183, no. 1, pp. 333–336, 2000.

[163] B. Pettinger, P. Schambach, C. J. Villagómez, and N. Scott, "Tip-enhanced Raman spectroscopy: near-fields acting on a few molecules," *Annual Review of Physical Chemistry*, vol. 63, pp. 379–399, 2012.

[164] A. Bouhelier, J. Renger, M. Beversluis, and L. Novotny, "Plasmon-coupled tip-enhanced near-field optical microscopy," *Journal of microscopy*, vol. 210, no. 3, pp. 220–224, 2003.

[165] N. Janunts, K. Baghdasaryan, K. V. Nerkararyan, and B. Hecht, "Excitation and superfocusing of surface plasmon polaritons on a silver-coated optical fiber tip," *Optics communications*, vol. 253, no. 1-3, pp. 118–124, 2005.

[166] W. Chen and Q. Zhan, "Numerical study of an apertureless near field scanning optical microscope probe under radial polarization illumination," *Optics express*, vol. 15, no. 7, pp. 4106–4111, 2007.

[167] W. Ding, S. Andrews, and S. Maier, "Internal excitation and superfocusing of surface plasmon polaritons on a silver-coated optical fiber tip," *Physical Review A*, vol. 75, no. 6, p. 063822, 2007.

[168] P. Hohenberg and W. Kohn, "Inhomogeneous electron gas," *Physical review*, vol. 136, no. 3B, p. B864, 1964.

[169] W. Kohn and L. J. Sham, "Self-consistent equations including exchange and correlation effects," *Physical Review*, vol. 140, no. 4A, p. A1133, 1965.

[170] A. P. Scott and L. Radom, "Harmonic vibrational frequencies: an evaluation of hartree- fock, møller- plesset, quadratic configuration interaction, density functional theory, and semiempirical scale factors," *The Journal of Physical Chemistry*, vol. 100, no. 41, pp. 16502–16513, 1996.

[171] W. Koch and M. Holthausen, "A chemist' guide to density functional theory. wiley," 2001.

[172] F. Jensen, *Introduction to computational chemistry*. John wiley & sons, 2017.

[173] D. Park, *Introduction to quantum theory*. New York : McGraw-Hill, 1964.

[174] Y. Wang and E. Carter, "Chap. 5 in theoretical methods in condensed phase chemistry, sd schwartz ed," 2000.

[175] W. Kohn, "Nobel lecture: Electronic structure of matter - wave functions and density functionals," January 1999.

[176] D. C. Langreth and J. P. Perdew, "The exchange-correlation energy of a metallic surface," *Solid State Communications*, vol. 17, no. 11, pp. 1425–1429, 1975.

[177] D. C. Langreth and M. Mehl, "Beyond the local-density approximation in calculations of ground-state electronic properties," *Physical Review B*, vol. 28, no. 4, p. 1809, 1983.

[178] J. P. Perdew, J. Chevary, S. Vosko, K. A. Jackson, M. R. Pederson, D. Singh, and C. Fiolhais, "Atoms, molecules, solids, and surfaces: Applications of the generalized gradient approximation for exchange and correlation," *Physical Review B*, vol. 46, no. 11, p. 6671, 1992.

[179] J. P. Perdew, P. Ziesche, and H. Eschrig, "Electronic structure of solids '91," *Akademie-Verlag, Berlin*, pp. 11–20, 1991.

[180] J. P. Perdew, K. Burke, and M. Ernzerhof, "Generalized gradient approximation made simple," *Physical Review Letters*, vol. 77, no. 18, p. 3865, 1996.

[181] J. P. Perdew, K. Burke, and M. Ernzerhof, "Generalized gradient approximation made simple [phys. rev. lett. 77, 3865 (1996)]," *Phys. Rev. Lett.*, vol. 78, pp. 1396–1396, Feb 1997.

[182] R. Car, "Introduction to density-functional theory and ab-initio molecular dynamics," *Quantitative Structure-Activity Relationships*, vol. 21, no. 2, pp. 97–104, 2002.

[183] P. Fulde, *Electron correlations in molecules and solids*, vol. 100. Springer Science & Business Media, 2012.

[184] L. Hedin and S. Lundqvist, "Effects of electron-electron and electron-phonon interactions on the one-electron states of solids," in *Solid state physics*, vol. 23, pp. 1–181, Elsevier, 1970.

[185] S. H. Vosko, L. Wilk, and M. Nusair, "Accurate spin-dependent electron liquid correlation energies for local spin density calculations: a critical analysis," *Canadian Journal of physics*, vol. 58, no. 8, pp. 1200–1211, 1980.

[186] C. Lee, W. Yang, and R. G. Parr, "Development of the colle-salvetti correlation-energy formula into a functional of the electron density," *Physical Review B*, vol. 37, no. 2, p. 785, 1988.

[187] A. D. Becke, "Density-functional exchange-energy approximation with correct asymptotic behavior," *Physical review A*, vol. 38, no. 6, p. 3098, 1988.

[188] J. P. Perdew, "Density-functional approximation for the correlation energy of the inhomogeneous electron gas," *Physical Review B*, vol. 33, no. 12, p. 8822, 1986.

[189] P. Stephens, F. Devlin, C. Chabalowski, and M. J. Frisch, "Ab initio calculation of vibrational absorption and circular dichroism spectra using density functional force fields," *The Journal of Physical Chemistry*, vol. 98, no. 45, pp. 11623–11627, 1994.

[190] A. D. Becke, "Density-functional thermochemistry. III. the role of exact exchange," *The Journal of Chemical Physics*, vol. 98, p. 5648, 1993.

[191] E. Fermi, "Sopra lo spostamento per pressione delle righe elevate delle serie spettrali," *Il Nuovo Cimento (1924-1942)*, vol. 11, no. 3, pp. 157–166, 1934.

[192] Wikimedia Commons, "Sketch pseudopotentials," 2006. [Online; accessed 17th June 2019].

[193] D. Hamann, M. Schlüter, and C. Chiang, "Norm-conserving pseudopotentials," *Physical Review Letters*, vol. 43, no. 20, p. 1494, 1979.

[194] D. Vanderbilt, "Soft self-consistent pseudopotentials in a generalized eigenvalue formalism," *Physical Review B*, vol. 41, no. 11, p. 7892, 1990.

[195] K. F. Domke, D. Zhang, and B. Pettinger, "Enhanced Raman spectroscopy: single molecules or carbon?," *The Journal of Physical Chemistry C*, vol. 111, no. 24, pp. 8611–8616, 2007.

[196] U. C. Fischer, "The tetrahedral tip as a probe for scanning near-field optical microscopy," in *Near Field Optics*, pp. 255–262, Springer, 1993.

[197] U. C. Fischer, J. Koglin, and H. Fuchs, "The tetrahedral tip as a probe for scanning near-field optical microscopy at 30 nm resolution," *J. Microsc.*, vol. 176, no. 3, pp. 231–237, 1994.

[198] K. S. Harsha, *Principles of vapor deposition of thin films*. Elsevier, 2005.

[199] J. C. Love, L. A. Estroff, J. K. Kriebel, R. G. Nuzzo, and G. M. Whitesides, "Self-assembled monolayers of thiolates on metals as a form of nanotechnology," *Chemical reviews*, vol. 105, no. 4, pp. 1103–1170, 2005.

[200] J. M. Tour, L. Jones, D. L. Pearson, J. J. Lamba, T. P. Burgin, G. M. Whitesides, D. L. Allara, A. N. Parikh, and S. Atre, "Self-assembled monolayers and multilayers of conjugated thiols,. alpha.,. omega.-dithiols, and thioacetyl-containing adsorbates. understanding attachments between potential molecular wires and gold surfaces," *Journal of the American Chemical Society*, vol. 117, no. 37, pp. 9529–9534, 1995.

[201] M. Kawasaki, T. Sato, T. Tanaka, and K. Takao, "Rapid self-assembly of alkanethiol monolayers on sputter-grown au (111)," *Langmuir*, vol. 16, no. 4, pp. 1719–1728, 2000.

[202] R. Yamada, H. Wano, and K. Uosaki, "Effect of temperature on structure of the self-assembled monolayer of decanethiol on au (111) surface," *Langmuir*, vol. 16, no. 13, pp. 5523–5525, 2000.

[203] C. D. Bain, E. B. Troughton, Y. T. Tao, J. Evall, G. M. Whitesides, and R. G. Nuzzo, "Formation of monolayer films by the spontaneous assembly of organic thiols from solution onto gold," *Journal of the American Chemical Society*, vol. 111, no. 1, pp. 321–335, 1989.

[204] F. Bensebaa, R. Voicu, L. Huron, T. H. Ellis, and E. Kruus, "Kinetics of formation of long-chain n-alkanethiolate monolayers on polycrystalline gold," *Langmuir*, vol. 13, no. 20, pp. 5335–5340, 1997.

[205] M. J. Frisch, G. W. Trucks, H. B. Schlegel, G. E. Scuseria, M. A. Robb, J. R. Cheeseman, G. Scalmani, V. Barone, B. Mennucci, G. A. Petersson, *et al.*, "Gaussian 09w, a. 02," 2009.

[206] J. M. Soler, E. Artacho, J. D. Gale, A. García, J. Junquera, P. Ordejón, and D. Sánchez-Portal, "The SIESTA method for ab initio order-n materials simulation," *Journal of Physics: Condensed Matter*, vol. 14, no. 11, p. 2745, 2002.

[207] W. Hehre, W. Latham, R. Ditchfield, M. Newton, and J. Pople, "Gaussian 70, quantum chemistry program exchange program no. 236," *University of Indiana, Bloomington, IN*, 1970.

[208] R. Ditchfield, W. J. Hehre, and J. A. Pople, "Self-consistent molecular-orbital methods. ix. an extended gaussian-type basis for molecular-orbital studies of organic molecules," *The Journal of Chemical Physics*, vol. 54, no. 2, pp. 724–728, 1971.

[209] T. H. Dunning Jr, "Gaussian basis sets for use in correlated molecular calculations. i. the atoms boron through neon and hydrogen," *The Journal of chemical physics*, vol. 90, no. 2, pp. 1007–1023, 1989.

[210] T. M. James, M. Schlösser, R. J. Lewis, S. Fischer, B. Bornschein, and H. H. Telle, "Automated quantitative spectroscopic analysis combining background subtraction, cosmic ray removal, and peak fitting," *Applied spectroscopy*, vol. 67, no. 8, pp. 949–959, 2013.

[211] I. Mikhailyuk and A. Razzhivin, "Background subtraction in experimental data arrays illustrated by the example of Raman spectra and fluorescent gel electrophoresis patterns," *Instruments and Experimental Techniques*, vol. 46, no. 6, pp. 765–769, 2003.

[212] N. Brandt, O. Brovko, A. Y. Chikishev, and O. Paraschuk, "Optimization of the rolling-circle filter for Raman background subtraction," *Applied spectroscopy*, vol. 60, no. 3, pp. 288–293, 2006.

[213] A. Savitzky and M. J. Golay, "Smoothing and differentiation of data by simplified least squares procedures.," *Analytical chemistry*, vol. 36, no. 8, pp. 1627–1639, 1964.

[214] A. Savitzky, "A historic collaboration," *Analytical Chemistry*, vol. 61, no. 15, pp. 921A–923A, 1989.

[215] M. Bradley, "Curve fitting in Raman and IR spectroscopy: basic theory of line shapes and applications," *Thermo Fisher Scientific, Madison, USA, Application Note*, vol. 50733, 2007.

[216] M. S. Bradley, "Lineshapes in IR and Raman spectroscopy: A primer," *Spectroscopy*, vol. 30, no. 11, pp. 42–+, 2015.

[217] G. Seber and C. Wild, "Nonlinear regression. 2003," *Hoboken: John Wiley.*

[218] M. Ratner and A. Aviram, "Molecular rectifiers," *Chem. Phys. Lett*, vol. 29, no. 2, pp. 277–283, 1974.

[219] M. Galperin, M. A. Ratner, A. Nitzan, and A. Troisi, "Nuclear coupling and polarization in molecular transport junctions: beyond tunneling to function," *Science*, vol. 319, no. 5866, pp. 1056–1060, 2008.

[220] M. M. Shulaker, G. Hills, N. Patil, H. Wei, H.-Y. Chen, H.-S. P. Wong, and S. Mitra, "Carbon nanotube computer," *Nature*, vol. 501, no. 7468, p. 526, 2013.

[221] M. A. Reed, C. Zhou, C. Muller, T. Burgin, and J. Tour, "Conductance of a molecular junction," *Science*, vol. 278, no. 5336, pp. 252–254, 1997.

[222] J. Reichert, R. Ochs, D. Beckmann, H. Weber, M. Mayor, and H. v. Löhneysen, "Driving current through single organic molecules," *Physical Review Letters*, vol. 88, no. 17, p. 176804, 2002.

[223] S. M. Lindsay and M. A. Ratner, "Molecular transport junctions: Clearing mists," *Advanced Materials*, vol. 19, no. 1, pp. 23–31, 2007.

[224] F. Giustino, "Electron-phonon interactions from first principles," *Reviews of Modern Physics*, vol. 89, no. 1, p. 015003, 2017.

[225] N. Sergueev, D. Roubtsov, and H. Guo, "Ab initio analysis of electron-phonon coupling in molecular devices," *Physical review letters*, vol. 95, no. 14, p. 146803, 2005.

[226] N. Tao, "Electron transport in molecular junctions," in *Nanoscience And Technology: A Collection of Reviews from Nature Journals*, pp. 185–193, World Scientific, 2010.

[227] E. Pop, "Energy dissipation and transport in nanoscale devices," *Nano Research*, vol. 3, no. 3, pp. 147–169, 2010.

[228] S. Ballmann, R. Härtle, P. B. Coto, M. Elbing, M. Mayor, M. R. Bryce, M. Thoss, and H. B. Weber, "Experimental evidence for quantum interference and vibrationally induced decoherence in single-molecule junctions," *Physical review letters*, vol. 109, no. 5, p. 056801, 2012.

[229] R. Hartle, M. Butzin, P. B. Coto, S. Ballmann, H. B. Weber, and M. Thoss, "Vibrationally induced decoherence in single-molecule junctions: The role of electron-hole pair creation processes," in *APS Meeting Abstracts*, 2013.

[230] R. Leturcq, C. Stampfer, K. Inderbitzin, L. Durrer, C. Hierold, E. Mariani, M. G. Schultz, F. Von Oppen, and K. Ensslin, "Franck–condon blockade in suspended carbon nanotube quantum dots," *Nature Physics*, vol. 5, no. 5, p. 327, 2009.

[231] J. Van Der Lit, M. P. Boneschanscher, D. Vanmaekelbergh, M. Ijäs, A. Uppstu, M. Ervasti, A. Harju, P. Liljeroth, and I. Swart, "Suppression of electron–vibron coupling in graphene nanoribbons contacted via a single atom," *Nature communications*, vol. 4, p. 2023, 2013.

[232] M. Galperin, M. A. Ratner, and A. Nitzan, "Inelastic electron tunneling spectroscopy in molecular junctions: Peaks and dips," *The Journal of chemical physics*, vol. 121, no. 23, pp. 11965–11979, 2004.

[233] Y. Li, P. Zolotavin, P. Doak, L. Kronik, J. B. Neaton, and D. Natelson, "Interplay of bias-driven charging and the vibrational stark effect in molecular junctions," *Nano letters*, vol. 16, no. 2, pp. 1104–1109, 2016.

[234] Y. Li, P. Doak, L. Kronik, J. B. Neaton, and D. Natelson, "Voltage tuning of vibrational mode energies in single-molecule junctions," *Proceedings of the National Academy of Sciences*, vol. 111, no. 4, pp. 1282–1287, 2014.

[235] A. Otto and M. Futamata, "Electronic mechanisms of SERS," in *Surface-Enhanced Raman Scattering*, pp. 147–182, Springer, 2006.

[236] Z. Ioffe, T. Shamai, A. Ophir, G. Noy, I. Yutsis, K. Kfir, O. Cheshnovsky, and Y. Selzer, "Detection of heating in current-carrying molecular junctions by Raman scattering," *Nature nanotechnology*, vol. 3, no. 12, p. 727, 2008.

[237] D. R. Ward, D. A. Corley, J. M. Tour, and D. Natelson, "Vibrational and electronic heating in nanoscale junctions," *Nature nanotechnology*, vol. 6, no. 1, p. 33, 2011.

[238] M. Galperin and A. Nitzan, "Raman scattering from biased molecular conduction junctions: The electronic background and its temperature," *Physical Review B*, vol. 84, no. 19, p. 195325, 2011.

[239] A. Mitra, I. Aleiner, and A. Millis, "Phonon effects in molecular transistors: Quantal and classical treatment," *Physical Review B*, vol. 69, no. 24, p. 245302, 2004.

[240] J. Koch, M. Semmelhack, F. Von Oppen, and A. Nitzan, "Current-induced nonequilibrium vibrations in single-molecule devices," *Physical Review B*, vol. 73, no. 15, p. 155306, 2006.

[241] J. S. Seldenthuis, H. S. Van Der Zant, M. A. Ratner, and J. M. Thijssen, "Vibrational excitations in weakly coupled single-molecule junctions: A computational analysis," *ACS nano*, vol. 2, no. 7, pp. 1445–1451, 2008.

[242] M. Uejima, T. Sato, K. Tanaka, and H. Kaji, "Enhancement of fluorescence in anthracene by chlorination: Vibronic coupling and transition dipole moment density analysis," *Chemical Physics*, vol. 430, pp. 47–55, 2014.

[243] K. Kneipp, Y. Wang, H. Kneipp, I. Itzkan, R. R. Dasari, and M. S. Feld, "Population pumping of excited vibrational states by spontaneous surface-enhanced Raman scattering," *Physical review letters*, vol. 76, no. 14, p. 2444, 1996.

[244] A. Brolo, A. Sanderson, and A. Smith, "Ratio of the surface-enhanced anti-Stokes scattering to the surface-enhanced Stokes-Raman scattering for molecules adsorbed on a silver electrode," *Physical Review B*, vol. 69, no. 4, p. 045424, 2004.

[245] H. S. Yoo, M. J. DeWitt, and B. H. Pate, "Vibrational dynamics of terminal acetylenes: I. comparison of the intramolecular vibrational energy redistribution

rate of gases and the total relaxation rate of dilute solutions at room temperature," *The Journal of Physical Chemistry A*, vol. 108, no. 8, pp. 1348–1364, 2004.

[246] M. A. Karimi, S. Bahoosh, M. Herz, R. Hayakawa, F. Pauly, and E. Scheer, "Shot noise of 1, 4-benzenedithiol single-molecule junctions," *Nano letters*, vol. 16, no. 3, pp. 1803–1807, 2016.

[247] S. Braig and K. Flensberg, "Vibrational sidebands and dissipative tunneling in molecular transistors," *Physical Review B*, vol. 68, no. 20, p. 205324, 2003.

[248] B. J. LeRoy, S. Lemay, J. Kong, and C. Dekker, "Electrical generation and absorption of phonons in carbon nanotubes," *Nature*, vol. 432, no. 7015, p. 371, 2004.

[249] D. P. Long, J. L. Lazorcik, B. A. Mantooth, M. H. Moore, M. A. Ratner, A. Troisi, Y. Yao, J. W. Ciszek, J. M. Tour, and R. Shashidhar, "Effects of hydration on molecular junction transport," *Nature Materials*, vol. 5, no. 11, p. 901, 2006.

[250] H. Iglev, M. Schmeisser, K. Simeonidis, A. Thaller, and A. Laubereau, "Ultrafast superheating and melting of bulk ice," *Nature*, vol. 439, no. 7073, p. 183, 2006.

[251] C. Gadermaier, A. Alexandrov, V. Kabanov, P. Kusar, T. Mertelj, X. Yao, C. Manzoni, D. Brida, G. Cerullo, and D. Mihailovic, "Electron-phonon coupling in high-temperature cuprate superconductors determined from electron relaxation rates," *Physical review letters*, vol. 105, no. 25, p. 257001, 2010.

[252] M. A. Reed and J. M. Tour, "Computing with molecules," *Scientific American*, vol. 282, no. 6, pp. 86–93, 2000.

[253] J. Markoff, "Designing the next wave of computer chips," *New York Times*, 2014.

[254] A. P. De Silva and S. Uchiyama, "Molecular logic and computing," *Nature Nanotechnology*, vol. 2, no. 7, p. 399, 2007.

[255] E. Lörtscher, M. Elbing, M. Tschudy, C. von Hänisch, H. B. Weber, M. Mayor, and H. Riel, "Charge transport through molecular rods with reduced π-conjugation," *ChemPhysChem*, vol. 9, no. 15, pp. 2252–2258, 2008.

[256] C. Toccafondi, G. Picardi, and R. Ossikovski, "Molecular bending at the nanoscale evidenced by tip-enhanced Raman spectroscopy in tunneling mode on thiol self-assembled monolayers," *The Journal of Physical Chemistry C*, vol. 120, no. 32, pp. 18209–18219, 2016.

[257] B. Nijs, F. Benz, S. J. Barrow, D. O. Sigle, R. Chikkaraddy, A. Palma, C. Carnegie, M. Kamp, R. Sundararaman, P. Narang, *et al.*, "Plasmonic tunnel junctions for single-molecule redox chemistry," *Nature communications*, vol. 8, no. 1, p. 994, 2017.

[258] E. Zojer, J. Cornil, G. Leising, and J.-L. Brédas, "Theoretical investigation of the geometric and optical properties of neutral and charged oligophenylenes," *Physical Review B*, vol. 59, no. 12, p. 7957, 1999.

[259] K. N. Baker, A. V. Fratini, T. Resch, H. C. Knachel, W. W. Adams, E. Socci, and B. Farmer, "Crystal structures, phase transitions and energy calculations of poly (p-phenylene) oligomers," *Polymer*, vol. 34, no. 8, pp. 1571–1587, 1993.

[260] M. Jalaie, S. Weatherhead, K. B. Lipkowitz, and D. Robertson, "Modulating force constants in molecular springs," *Electronic Journal of Theoretical Chemistry*, vol. 2, no. 1, pp. 268–272, 1997.

[261] P. Rempala and B. T. King, "Simulation of actuation by polymeric polyelectrolyte helicenes," *Journal of chemical theory and computation*, vol. 2, no. 4, pp. 1112–1118, 2006.

[262] L. Rulíšek, O. Exner, L. Cwiklik, P. Jungwirth, I. Starỳ, L. Pospíšil, and Z. Havlas, "On the convergence of the physicochemical properties of [n] helicenes," *The Journal of Physical Chemistry C*, vol. 111, no. 41, pp. 14948–14955, 2007.

[263] P. Šesták, J. Wu, J. He, J. Pokluda, and Z. Zhang, "Extraordinary deformation capacity of smallest carbohelicene springs," *Physical Chemistry Chemical Physics*, vol. 17, no. 28, pp. 18684–18690, 2015.

[264] J. Vacek, J. V. Chocholoušová, I. G. Stará, I. Starỳ, and Y. Dubi, "Mechanical tuning of conductance and thermopower in helicene molecular junctions," *Nanoscale*, vol. 7, no. 19, pp. 8793–8802, 2015.

[265] Y.-D. Guo, X.-H. Yan, Y. Xiao, and C.-S. Liu, "U-shaped relationship between current and pitch in helicene molecules," *Scientific reports*, vol. 5, p. 16731, 2015.

[266] O. Stetsovych, P. Mutombo, M. Švec, M. Šámal, J. Nejedlý, I. Císařová, H. Vázquez, M. Moro-Lagares, J. Berger, J. Vacek, *et al.*, "Large converse piezoelectric effect measured on a single molecule on a metallic surface," *Journal of the American Chemical Society*, vol. 140, no. 3, pp. 940–946, 2018.

[267] V. Kiran, S. P. Mathew, S. R. Cohen, I. Hernández Delgado, J. Lacour, and R. Naaman, "Helicenes - a new class of organic spin filter," *Advanced Materials*, vol. 28, no. 10, pp. 1957–1962, 2016.

[268] T.-R. Pan, A.-M. Guo, and Q.-F. Sun, "Spin-polarized electron transport through helicene molecular junctions," *Physical Review B*, vol. 94, no. 23, p. 235448, 2016.

[269] J. R. Brandt, F. Salerno, and M. J. Fuchter, "The added value of small-molecule chirality in technological applications," *Nature Reviews Chemistry*, vol. 1, no. 6, p. 0045, 2017.

[270] M. Groen and H. Wynberg, "Optical properties of some heterohelicenes. absolute configuration," *Journal of the American Chemical Society*, vol. 93, no. 12, pp. 2968–2974, 1971.

[271] J. J. Maki and A. Persoons, "One-electron second-order optical activity of a helix," *The Journal of chemical physics*, vol. 104, no. 23, pp. 9340–9348, 1996.

[272] T. Caronna, M. Catellani, S. Luzzati, L. Malpezzi, S. V. Meille, A. Mele, C. Richter, and R. Sinisi, "Molecular crystal architecture and optical properties of a thiohelicenes series containing 5, 7, 9, and 11 rings prepared via photochemical synthesis," *Chemistry of materials*, vol. 13, no. 11, pp. 3906–3914, 2001.

[273] N. Saleh, B. Moore, M. Srebro, N. Vanthuyne, L. Toupet, J. G. Williams, C. Roussel, K. K. Deol, G. Muller, J. Autschbach, *et al.*, "Acid/base-triggered switching of circularly polarized luminescence and electronic circular dichroism in organic and organometallic helicenes," *Chemistry–A European Journal*, vol. 21, no. 4, pp. 1673–1681, 2015.

[274] H. Tanaka, Y. Kato, M. Fujiki, Y. Inoue, and T. Mori, "Combined experimental and theoretical study on circular dichroism and circularly polarized luminescence of configurationally robust d 3-symmetric triple pentahelicene," *The Journal of Physical Chemistry A*, vol. 122, no. 37, pp. 7378–7384, 2018.

[275] T. Verbiest, S. Van Elshocht, M. Kauranen, L. Hellemans, J. Snauwaert, C. Nuckolls, T. J. Katz, and A. Persoons, "Strong enhancement of nonlinear optical properties through supramolecular chirality," *Science*, vol. 282, no. 5390, pp. 913–915, 1998.

[276] K.-H. Ernst, Y. Kuster, R. Fasel, M. Müller, and U. Ellerbeck, "Two-dimensional separation of [7] helicene enantiomers on Cu (111)," *Chirality: The Pharmacological, Biological, and Chemical Consequences of Molecular Asymmetry*, vol. 13, no. 10, pp. 675–678, 2001.

[277] K. Clays, K. Wostyn, A. Persoons, S. Maiorana, A. Papagni, C. A. Daul, and V. Weber, "Experimental study of the second-order non-linear optical properties of tetrathia-[7]-helicene," *Chemical physics letters*, vol. 372, no. 3-4, pp. 438–442, 2003.

[278] H. Oyama, K. Nakano, T. Harada, R. Kuroda, M. Naito, K. Nobusawa, and K. Nozaki, "Facile synthetic route to highly luminescent sila [7] helicene," *Organic letters*, vol. 15, no. 9, pp. 2104–2107, 2013.

[279] H. Sakai, S. Shinto, J. Kumar, Y. Araki, T. Sakanoue, T. Takenobu, T. Wada, T. Kawai, and T. Hasobe, "Highly fluorescent [7] carbohelicene fused by asymmetric 1, 2-dialkyl-substituted quinoxaline for circularly polarized luminescence and electroluminescence," *The Journal of Physical Chemistry C*, vol. 119, no. 24, pp. 13937–13947, 2015.

[280] L. Koetzner, M. J. Webber, A. Martinez, C. De Fusco, and B. List, "Asymmetric catalysis on the nanoscale: the organocatalytic approach to helicenes," *Angewandte Chemie International Edition*, vol. 53, no. 20, pp. 5202–5205, 2014.

[281] M. Karras, J. Holec, L. Bednárová, R. Pohl, B. Schmidt, I. G. Stará, and I. Stary, "Asymmetric synthesis of nonracemic 2-amino [6] helicenes and their self-assembly into langmuir films," *The Journal of organic chemistry*, vol. 83, no. 10, pp. 5523–5538, 2018.

[282] F. Teplỳ, I. G. Stará, I. Starỳ, A. Kollárović, D. Šaman, L. Rulíšek, and P. Fiedler, "Synthesis of [5]-,[6]-, and [7] helicene via Ni (0)-or Co (i)-catalyzed isomerization of aromatic cis, cis-dienetriynes," *Journal of the American Chemical Society*, vol. 124, no. 31, pp. 9175–9180, 2002.

[283] G. Foti, H. Vázquez, D. Sánchez-Portal, A. Arnau, and T. Frederiksen, "Identifying highly conducting Au-C links through inelastic electron tunneling spectroscopy," *The Journal of Physical Chemistry C*, vol. 118, no. 46, pp. 27106–27112, 2014.

[284] G. Foti and H. Vázquez, "Tip-induced gating of molecular levels in carbene-based junctions," *Nanotechnology*, vol. 27, no. 12, p. 125702, 2016.

[285] G. Foti and H. Vázquez, "Interface tuning of current-induced cooling in molecular circuits," *The Journal of Physical Chemistry C*, vol. 121, no. 2, pp. 1082–1088, 2017.

[286] N. P. Arasu and H. Vázquez, "Direct Au-C contacts based on biphenylene for single molecule circuits," *Physical Chemistry Chemical Physics*, vol. 20, no. 15, pp. 10378–10383, 2018.

[287] S. García-Gil, A. García, N. Lorente, and P. Ordejón, "Optimal strictly localized basis sets for noble metal surfaces," *Physical Review B*, vol. 79, no. 7, p. 075441, 2009.

[288] P. Mcmillan, "A Raman spectroscopic study of glasses in the system CaO-MgO-SiO2," *Amer. Mineral*, pp. 645–659, 1984.

[289] A. B. Andrews, D. Wang, K. M. Marzec, O. C. Mullins, and K. B. Crozier, "Surface enhanced Raman spectroscopy of polycyclic aromatic hydrocarbons and molecular asphaltenes," *Chemical Physics Letters*, vol. 620, pp. 139–143, 2015.

[290] N. T. T. An, D. Q. Dao, P. C. Nam, B. T. Huy, and H. N. Tran, "Surface enhanced Raman scattering of melamine on silver substrate: an experimental and DFT study," *Spectrochimica Acta Part A: Molecular and Biomolecular Spectroscopy*, vol. 169, pp. 230–237, 2016.

[291] M. C. Chong, G. Reecht, H. Bulou, A. Boeglin, F. Scheurer, F. Mathevet, and G. Schull, "Narrow-line single-molecule transducer between electronic circuits and surface plasmons," *Physical review letters*, vol. 116, no. 3, p. 036802, 2016.

[292] G. Rubio, N. Agrait, and S. Vieira, "Atomic-sized metallic contacts: mechanical properties and electronic transport," *Physical review letters*, vol. 76, no. 13, p. 2302, 1996.

[293] Z. Huang, F. Chen, P. A. Bennett, and N. Tao, "Single molecule junctions formed via Au-thiol contact: stability and breakdown mechanism," *Journal of the American Chemical Society*, vol. 129, no. 43, pp. 13225–13231, 2007.

[294] I. V. Pobelov, K. P. Lauritzen, K. Yoshida, A. Jensen, G. Mészáros, K. W. Jacobsen, M. Strange, T. Wandlowski, and G. C. Solomon, "Dynamic breaking of a single gold bond," *Nature communications*, vol. 8, p. 15931, 2017.

[295] D. Krüger, R. Rousseau, H. Fuchs, and D. Marx, "Towards mechanochemistry: mechanically induced isomerizations of thiolate–gold clusters," *Angewandte Chemie International Edition*, vol. 42, no. 20, pp. 2251–2253, 2003.

[296] Z. Huang, B. Xu, Y. Chen, M. D. Ventra, and N. Tao, "Measurement of current-induced local heating in a single molecule junction," *Nano letters*, vol. 6, no. 6, pp. 1240–1244, 2006.

[297] A. E. Reed, L. A. Curtiss, and F. Weinhold, "Intermolecular interactions from a natural bond orbital, donor-acceptor viewpoint," *Chemical Reviews*, vol. 88, no. 6, pp. 899–926, 1988.

[298] Y. S. Park, A. C. Whalley, M. Kamenetska, M. L. Steigerwald, M. S. Hybertsen, C. Nuckolls, and L. Venkataraman, "Contact chemistry and single-molecule conductance: a comparison of phosphines, methyl sulfides, and amines," *Journal of the American Chemical Society*, vol. 129, no. 51, pp. 15768–15769, 2007.

[299] M. Frei, S. V. Aradhya, M. S. Hybertsen, and L. Venkataraman, "Linker dependent bond rupture force measurements in single-molecule junctions," *Journal of the American Chemical Society*, vol. 134, no. 9, pp. 4003–4006, 2012.

[300] R. P. Wool, "Mechanisms of frequency shifting in the infrared spectrum of stressed polymer," *Journal of Polymer Science: Polymer Physics Edition*, vol. 13, no. 9, pp. 1795–1808, 1975.

[301] V. K. Mitra, W. M. Risen Jr, and R. H. Baughman, "A laser Raman study of the stress dependence of vibrational frequencies of a monocrystalline polydiacetylene," *The Journal of Chemical Physics*, vol. 66, no. 6, pp. 2731–2736, 1977.

[302] E. Kampshoff, E. Hahn, and K. Kern, "Correlation between surface stress and the vibrational shift of CO chemisorbed on Cu surfaces," *Physical review letters*, vol. 73, no. 5, p. 704, 1994.

[303] G. R. Hutchison and X. Quan, "Flexible molecular piezoelectric device," May 29 2018. US Patent 9,985,197.

[304] F. Lederer, F. Graupner, B. Maerz, M. Braun, and W. Zinth, "Excimer formation in 9, 10-dichloroanthracene–solutions and crystals," *Chemical Physics*, vol. 428, pp. 82–89, 2014.

[305] P. Hamm, "Coherent effects in femtosecond infrared spectroscopy," *Chemical physics*, vol. 200, no. 3, pp. 415–429, 1995.

[306] M. Levitus and M. A. Garcia-Garibay, "Polarized electronic spectroscopy and photophysical properties of 9, 10-bis (phenylethynyl) anthracene," *The Journal of Physical Chemistry A*, vol. 104, no. 38, pp. 8632–8637, 2000.

[307] C. V. Suneesh and K. R. Gopidas, "Long-lived photoinduced charge separation in flexible 9, 10-bis (phenylethynyl) anthracene- phenothiazine dyads," *The Journal of Physical Chemistry C*, vol. 113, no. 4, pp. 1606–1614, 2009.

[308] N. Gottfried, A. Seilmeier, and W. Kaiser, "Transient internal temperature of anthracene after picosecond infrared excitation," *Chemical physics letters*, vol. 111, no. 4-5, pp. 326–332, 1984.

[309] F. Emmerling, M. Lettenberger, and A. Laubereau, "Vibrational dynamics of anthracene in liquid solution studied by picosecond IR/UV spectroscopy with polarization resolution," *The Journal of Physical Chemistry*, vol. 100, no. 50, pp. 19251–19256, 1996.

[310] P. Hamm, S. Ohline, and W. Zinth, "Vibrational cooling after ultrafast photoisomerization of azobenzene measured by femtosecond infrared spectroscopy," *The Journal of chemical physics*, vol. 106, no. 2, pp. 519–529, 1997.

[311] A. Charvat, J. Aβmann, B. Abel, and D. Schwarzer, "Real-time probing of intramolecular vibrational energy redistribution and intermolecular vibrational energy transfer of selectively excited CH2I2 molecules in solution," *The Journal of Physical Chemistry A*, vol. 105, no. 21, pp. 5071–5080, 2001.

[312] R. J. Sension, A. Z. Szarka, and R. M. Hochstrasser, "Vibrational energy redistribution and relaxation in the photoisomerization of cis-stilbene," *The Journal of chemical physics*, vol. 97, no. 7, pp. 5239–5242, 1992.

[313] S. Fischer and A. Laubereau, "Dephasing processes of molecular vibrations in liquids," *Chemical Physics Letters*, vol. 35, no. 1, pp. 6–12, 1975.

List of Figures

List of Acronyms

7HdiET	S,S'-heptahelicene-2,17-diyl diethanethioate
AFM	Atomic Force Microscopy
BPA	9,10-bis-phenylethynyl-anthracene
CCD	Charge-Coupled Device
DAC	Digital to Analog Converter
DC	Direct Current
DFT	Density Functional Theory
DOS	Density of States
FWHM	Full Width at Half Maximum
GGA	Generalized Gradient Approximation
GTOs	Gaussian-Type Orbitals
HOMO	Highest Occupied Molecular Orbital
I-d	Current-Distance
IPT	Inter-Phenyl Torsion
I-V	Current-Voltage
LDA	Local Density Approximation
LSDA	Local Spin-Density Approximation
LUMO	Lowest Unoccupied Molecular Orbital
MCBJ	Mechanically Controlled Break-Junctions
MJS	Molecular Junction Spectroscopy
ND	Neutral-Density
OFDFT	Orbital Free kinetic-energy Density Functional Theory
RCF	Rolling-Circle Filter
SAM	Self-Assembled Monolayers
SCARF	Savitzky–Golay Coupled Advanced Rolling-Circle Filter
SCF	Self-Consistent Field
SEM	Scanning Electron Microscope
SERS	Surface Enhanced Raman Spectroscopy
SIESTA	Spanish Initiative for Electronic Simulations with Thousands of Atoms
SNOM	Scanning Near-field Optical Microscopy

SPM	Scanning Probe Microscopy
SPP	Surface Plasmon Polarition
SPs	Surface Plasmons
STOs	Slater-Type Orbitals
TERS	Tip-Enhanced Raman Spectroscopy
THF	Tetrahydrofurane
TPD	p-terphenyl-4,4”-dithiol
TPDT	4, 4”-bis (acetylthiol)-2, 2’, 5’, 2”-tetramethyl-[1, 1’; 4’, 1”] terphenyl
TSP	Titanium Sublimation Pump
UHV	Ultra High Vacuum

Acknowledgements

First of all, I would like to express my very great appreciation to **Prof. Dr. Johannes Barth** for providing me the opportunity to pursue a PhD degree in an innovative, supportive and friendly research group.

I would like to express my deep gratitude to **Dr. Joachim Reichert** for the continuous support of my PhD study and related researches, for his patience, motivation and insightful comments. It is a great pleasure to work in his team. The challenging projects, the extensible device as well as the flexible work environment enable me to further develop my knowledge and skills.

I am particularly grateful for the assistance given by **Dr. Peter Hasch**. We worked together for two and a half years. He made significant improvements in the experimental procedures and kindly guided me to these innovations. Only based on his brilliant work I could realize the statistical measurements. During the daily coffee break, we talked about research details and plans, life in Germany, cultures and cars, to name but a few, which got me better involved in living here.

My sincere thanks also goes to **Dr. Héctor Vázquez** and his team in Prague. I joined his team for two weeks in May 2017 to learn the DFT simulations. It was a memorable time during and outside work hours. Thanks for the strong support of my research project.

I would also like to thank **Dr. Chao Jing** for her assistance in lab work and reviewing this thesis. Thanks to **Dr. Yuanqin He**, **Dr. Runyuan Han**, **Dr. Juan Li** and **Bodong Zhang** for spending lunch break together.

Finally, I would like to thank my family for supporting my work spiritually and my life in general.